UNIVERSITÀ DELLA CALABRIA

Dipartimento di Fisica

Doctorate School of Science and Technique
"Bernardino Telesio"

A thesis submitted for the degree of Doctor of Philosophy in Science and Technology of Mesophases and Molecular Materials

XXVI Cycle

FIS/03

Synthesis and Characterization of Enstatite and Talc Doped with Zinc and Manganese

School Director
Prof. Roberto Bartolino

Curriculum Coordinator
Prof. Carlo C Versace

Supervisor
Prof. Enzo Cazzanelli

Tutor
Dott. Andrea Bloise

Candidate
Dott.ssa Manuela Catalano

December 2013

INDICE

Abstract

Synthesis and characterization of enstatite and talc doped with zinc and manganese

In recent years, particular interest has been addressed by researchers in the synthesis and study of silicates such as enstatite $MgSiO_3$ and talc $Mg_3Si_4O_{10}(OH)_2$. The first one is useful for several technological applications such as substrates in electronics, high frequency insulators, thermal insulators in high temperatures applications, and as luminescent materials in laser technology. The latter, because of the low cost and good properties (i.e. resistant to heat and acids, hydrophobic, electrical insulating) is widely used in many different products such as ceramics, papers, cosmetics, foods, polymers and filler in composites. The usual presence of foreign ions (e.g., Mn, Ti, Ni, etc.) and their inconstant amounts in natural enstatite and talc hinder the use of these minerals as high-performance materials. For these reasons, in recent years pure and doped enstatite and talc have been grown and characterized in several different ways. Nevertheless, there are still various problems to be solved in order to obtain very high quality crystals and the desired changes in the physical and chemical properties of them when they are doped with metal elements.

In this work, Zn-doped enstatite, Mn-doped enstatite, Zn-doped talc and Mn-doped talc have been grown and characterized with different techniques. The starting materials and the final products were characterized and studied by binocular microscope, powder crystal X-ray diffraction (XRPD), scanning electron microscopy with energy-dispersive spectrometry (SEM/EDS), single-crystal X-ray diffraction (XRD), micro-Raman (μ-R), cathodoluminescence (CL), differential scanning calorimetry, thermogravimetric analysis (DSC-TG) and Fourier transform infrared spectroscopy (FT-IR).

Zn- and Mn-doped enstatite was successfully produced by slow-cooling flux growth method, using MoO_3, V_2O_5, Li_2CO_3 as melting agent. Several starting mixtures, with different MnO or ZnO concentrations, were first held at 1350 °C, 1250 °C 1050 °C and 950 °C and then slowly cooled down to 700 °C or 600 °C with different cooling rate (3.75 °C/h, 2.1 °C/h, 1.8 °C/h 1.7 °C/h). Enstatite crystallizes in the orthorhombic and monoclinic systems as revealed by XRD and Raman spectra. Transparent Zn-doped enstatite (max length of 3.5 mm) and reddish Mn-doped enstatite (max length of 8 mm) single crystals are euhedral in form, not homogeneous in width and inclusion free. Maximum content of Mn-dopant is 14.52 wt %, while the maximum amount of Zn-dopant

is 10.49 wt%. Crystals grow under equilibrium conditions only when the dopant content is maintained at low value. When either Zn or Mn is totally substituted for Mg in the starting material, no enstatite is produced. The presence of the dopant in the enstatite structure causes a decrease in unit cell volume respect to the pure one and strongly affects the CL-signal and micro-Raman spectra. CL spectrum of Mn-doped enstatite contains a broad emission located at 677 nm and attributed to the $^4T_{1g}(G) \rightarrow {}^6A_{1g}(S)$ transition of octahedral Mn^{2+} centres. The presence of Zn in enstatite induces very remarkable peak broadening by the mode at 133 cm^{-1} and 343 cm^{-1} in the Raman spectra; for these modes a strong component of metal ion displacement must be postulated. Raman spectra of Mn-enstatite show: i) a general decrease of Raman intensity due to the increase in surface reflection when the MnO dopant concentration increases; ii) a widening and a down shifting of the peak positions indicating changes in vibrational modes because of the increasing presence of MnO.

Zn- and Mn-doped talc was successfully synthesized in hydrothermal conditions at temperatures of 300, 500 and 650 °C, under constant pressure of 2 kbar and reaction time of 160 hours. Talc morphology and content of dopant within the crystals show strong dependence on crystallization temperature. Talc exhibits a cabbage-like morphology, its classical hexagonal tabular morphology and fibrous morphology. The best temperature to obtain the highest abundance of Zn- and Mn-doped talc is 650 °C. A decrease in temperature from 650 to 300 °C: i) worsens the reactions and poorly crystallized Zn- and Mn-doped talc is obtained; ii) increases the content of zinc or manganese dopant. Talc only grows when Mg is not totally substituted by either zinc or manganese in the starting mixture. Zn-doped talc formation is increased by treating the starting mixture with H_2O + HCl; conversely, the reactant H_2O + $CaCl_2$ inhibits the growth of talc. In order to increase doped talc yield, large amounts of aqueous solution is as crucial as high temperatures. The presence of varying amounts of metal elements replacing Mg in talc influences its temperature decomposition. Indeed, the thermal stability of Zn- and Mn-doped talc decreases with respect to pure one. Zn-dopant in talc mainly affected the hydroxyl stretching fundamental peak (3674 cm^{-1}), splitting itself into as many as four peaks with respect to non-doped talc, which displayed only a sharp band. The splitting appears to be dependent on the degree of substitution of the magnesium in the octahedral layer and related to the electronegativity difference between Zn and Mg.

Future studies will be carried out on these materials to have a better knowledge of other physical properties, useful in novel applications.

Introduction

The flux growth and hydrothermal techniques have been most popular, garnering interest from scientists and technologists of different disciplines, particularly in the last twenty years.

These methods dealing with laboratory simulations have helped the earth scientists to determine complex geological processes of the formation of rocks, minerals, and ore deposits. As the subject became more and more popular among geologists, new branches of geology emerged as "Experimental Mineralogy" and "Experimental Petrology."

The basic precept of experimental petrology and mineralogy is that one can reproduce in the laboratory the condition under which rocks and minerals have formed in nature.

Today, the Experimental Mineralogy has found its place in several branches of science and technology, which involve materials scientists, earth scientists, materials engineers, metallurgists, physicists, chemists, biologists, and others.

Different methods have been developed in order to synthesize many different minerals in various chemical systems, technologically useful.

Among them, the most known and used are the slow-cooling flux growth method, the hydrothermal method, Czochralski, sol–gel, co-precipitation, etc. (Grandin de Le´ previer, 1983 ; Ushio et al.,, 1991; Tanaka & Takey., 1997 ; Stalder, 2002; Goel et al., 2007).

In particular, the slow-cooling flux growth method was successfully used to produce high-quality single crystals such as oxides and silicates at atmospheric pressure and high temperature. Flux crystallization is particularly attractive for the growth of silicates since their growth from pure melts is generally difficult: they often melt incongruently. Moreover, single crystal are interesting materials because structure determinations and intrinsic property measurements are preferably, sometimes exclusively, carried out on single crystals and for certain applications, most notably those which rely on optical and/or electronic properties (laser crystals, semiconductors, etc.), single crystals are necessary.

An understanding of the mineral formation in nature under high pressure and temperature conditions in the presence of water led to the development of the hydrothermal technique. Thus, the hydrothermal technique became a very popular means to simulate the natural conditions existing under the earth's crust and synthesizing them in the laboratory.

Further importance of the hydrothermal technique was realized soon after the synthesis of large single crystals of quartz by Nacken (1946) and zeolites by Barrer (1948) in a commercial way during late 1930s and 1940s, respectively.

Today the hydrothermal technique is largely used by researcher because of its several advantages. Indeed, by this method, widely accepted since 1960s, all inorganic species, starting from native elements to the most complex oxides, silicates, germanates, phosphates, chalcogenides, carbonates, and so on, have been obtained.

In particular, in my work, the flux growth method and the hydrothermal method are used to obtain enstatite and talc respectively.

The first attempt to synthesize enstatite ($MgSiO_3$) a silicate member of the pyroxene family was in 1851 by Ebelman[3] in order to study its polymorphism.

Owing to their good properties, such as high refractoriness and strength, combined with low dielectric constant and low thermal expansion, enstatite crystals are ideal substrates in electronics as insulators at high frequencies and also optimal materials for thermal insulation in application at high temperatures (Holand & Beall, 2012; Beall, 1993) and more recently, as biorestorations in enstatite based-ceramics (Goel e at., 2007). Since large and high quality single crystals of enstatite are very rare in nature, it is important to obtain such a kind of crystals because of their usefulness in investigating their physical, chemical, electrical and mechanical properties. In addition, with the discovery of doped enstatite single crystals, their use was also proposed for laser technology luminescence (Gaft et al., 2005).

The presence of dopant to ideal chemical composition (e.g., $MgSiO_3$) in enstatite, even in small amounts, affects its chemical/physical properties and the efficiency of laser technology, which can be enhanced by increasing doping levels. So far, enstatite has been doped with varying amounts of Cr^{3+}(Cavalli & Bettinelli, 1993; Moncorgè et al.,1999), Ni^{2+}(Moncorgè et al.,1999, Bloise et al., 2011), Mn^{2+}(Lin et al., 2006) and $Li^{+}Sc^{3+}$ ($LiScSi_2O_6$) (Smyth & Ito, 1977), Ti^{4+} (Bloise et al., 2011), but no paper reports about enstatite doped with zinc; Mn-doped enstatite has been mentioned in only one paper (Lin et al., 2008), in which it was synthesized by sol-gel method, mainly to study its luminescent properties, and not to define in detail the synthesis conditions allowing its growth.

For this reason and in the light of the potential applications of these doped crystals to advanced technologies, the present work aimed to clarify whether it is possible to obtain Zn-doped and Mn-doped $MgSiO_3$, in order to elucidate the best conditions of growth and to assess the possible effects on its features (*i.e.* morphology, size, cell dimensions, chemical/physical properties) due to the amount of Zn or Mn-dopant.

In regard to talc, $Mg_3Si_4O_{10}(OH)_2$, the low cost and good properties (i.e. resistant to heat and acids, hydrophobic, electrical insulating) make it widely used in many different products such as, ceramics, papers, cosmetics, foods, polymers and filler in composities (Zanzenski et al., 1995; Karrad et al., 1998; Johnson & Virta, 2000; Ferrage et al., 2002 E. Ferrage et al., 2003, Denac et. al., 2004; Ahmeda et al., 2007; Dellisanti et al., 2009).

The usual presence of foreign ions (i.e. Fe, Ni, Al, etc.) in natural talc and their inconstant amounts may inhibit the high-performance of this mineral (Marzbani et al., 2013). For these reasons and owing its good properties, syntheses and property studies have been conducted in recent years on non-doped and doped talc. So far, Ni-, Co-, Fe-, S-, O-, MgO-,$Mg(NO_3)_2$- and Mn-doped talc has been synthesised mainly to study its chemical and physical properties (e. g. electric conductivity) (Deer et al., 2009, Takahashi et al., 1994; Wilkins & Ito, 1967; Ishida, 1990; Bloise et al., 2010; Kirak et al., 1999; Pidluzhna et al., 2012). Talc doped with Zn and Mn has been mentioned in only one paper (Wilkins & Ito, 1967), which mainly reports the infrared spectrum of some synthetic Zn and Mn-doped talc. On the basis of the aforesaid remarks, the purposes of the present thesis were: i) to clarify whether it is possible to obtain isomorphic series between talc s.s. $Mg_3Si_4O_{10}(OH)_2$ and $Zn_3Si_4O_{10}(OH)_2$; ii) to assess whether incorporation of Zn or Mn in the talc structure leads to changes in its chemical/physical properties, iii) to assess the potential of the different talc products. Deeper knowledge of the hydrothermal growth conditions, together with the physical performance of these doped crystals may allow them to be exploited for new applications.

Thesis Outline and Motivation

In this thesis work, the main scope was to create a new technologically advanced material and to characterize them.

First, the attention is focused on growth of two silicates using different techniques: slow-cooling flux method and hydrothermal method for enstatite and talc respectively.

This research has two particular prominent aspects: first, to give information about the probable changes in phase equilibria when foreign ions are introduced in the growth system; second, to study how the presence of foreign ions within the structure of both types of crystals may change the physical, chemical and optical characteristics of them.

For this purpose, increasing amount of zinc and manganese were introduced as dopant in enstatite and talc lattice according to their stoichiometry.

In this framework, particular attention was also devoted to the investigation and characterization of the grown crystals using various techniques.

Crystals were identified by x-ray powder diffractometer. The chemical composition and morphology were investigated by energy dispersive spectroscopy (EDS) with a field-emission scanning electron microscope (SEM).

Single crystals of enstatite were analyzed by single crystals x-ray diffraction, cathodoluminescence (CL) and micro-Raman spectroscopy, while talc crystals were studied by differential scanning calorimetry thermogravimetric analysis (DSC-TG) and Fourier transform infrared (FT-IR).

Pure enstatite single crystals and talc crystals were also synthesized in order to investigate the physical and chemical differences between pure phases and doped one.

This thesis work can be divided as follow:

In the first part (Chapter 1) a brief description of the structure, chemistry, optical and physical properties of enstatite and talc is reported. The generalities of zinc and manganese are also summarized.

The vertical furnace apparatus and the externally- heated pressure vessels are described in chapter 2, in which it is also reported about the instrumentations used to perform part of the measurements reported in this work.

In Chapter 3, the basic aspects of slow-cooling flux growth and hydrothermal growth techniques are explained and the experimental conditions and the procedures for crystal growth are discussed.

Chapter 4 focuses on the analyses, results and discussions. Finally, the main findings obtained during this Ph.D. work are resumed in Chapter 5.

Chapter 1. General Properties of Enstatite and Talc

In this chapter, the fundamental properties of enstatite and talc will be discussed. First, the chemical and structural characterization of both minerals that are the main object of this work will be presented. Then, the general properties of zinc and manganese elements will be reported.

1.1 Enstatite

Enstatite is the magnesium end-member of the pyroxene silicate mineral series enstatite ($MgSiO_3$) - ferrosilite ($FeSiO_3$). The magnesium rich members of the solid solution series are common rock-forming minerals found in igneous and metamorphic rocks (serpentine deposits). It is also a constituent of some meteorites.

1.1.1 Chemistry

Enstatite belongs to the pyroxene group (inosilicates, single chain silicates). This group includes both orthorhombic and monoclinic minerals and the general formula of them may be expressed as:

$$X_{1-p}Y_{1+p}Z_2O_6$$

where *X*= Ca, Na; *Y*= Mg, Fe^{2+}, Mn, Li, Ni Al, Fe^{3+}, Cr, Ti; *Z*= Si, Al. In the orthopyroxene series p= 1. The wide range of replacements in the *Y* ions commonly involves substitution of ions of different charge and is accompanied by compensatory replacement of either the *X* or *Z* ions; the substitution must be such that the sum of the charges of the *X Y Z* ions is twelve.

The pyroxenes can be divided into several groups based on chemistry and crystallography

1) *Orthorhombic pyroxenes:*

Enstatite-orthoferrosilite $(Mg,Fe^{2+})_2Si_2O_6$

2) *Monoclinic pyroxenes:*

Diopside-Hedenbergite-Johannsenite $Ca(Mg,Fe^{2+},Mn)Si_2O_6$

Augite-Ferroaugite $(Ca,Na,Mg,Fe^{2+},Mn,Al,Fe^{3+},Ti)_2(Si,Al)_2O_6$

Pigeonite $(Mg,Fe^{2+},Ca)(Mg, Fe^{2+},)Si_2O_6$

Aegirine-Aegirine-augite $NaFe^{3+}Si_2O_6$-$(Na,Ca)(Fe^{3+},Fe^{2+},Mg)Si_2O_6$

Spodumene $LiAlSi_2O_6$

Jadeite $NaAlSi_2O_6$

1.1.2 Structure

The structure of the minerals of the pyroxene group has two fundamental unities (Fig. 1.1):

1. the tetrahedral layer, in which each T tetrahedron shares two corners with adjacent tetrahedra to form infinite chains parallel to *c*-axis which are branched together by the two (M1, M2) symmetrical Mg-octahedral sites;
2. M1, M2-octahedral sites occupied by cations present in *X* and *Y* respectively. Cation sites have six or eight-fold coordination accordingly with the type of cation. Each poliedron shares two corners with adjacent poliedra to form layers parallel to c-axis.

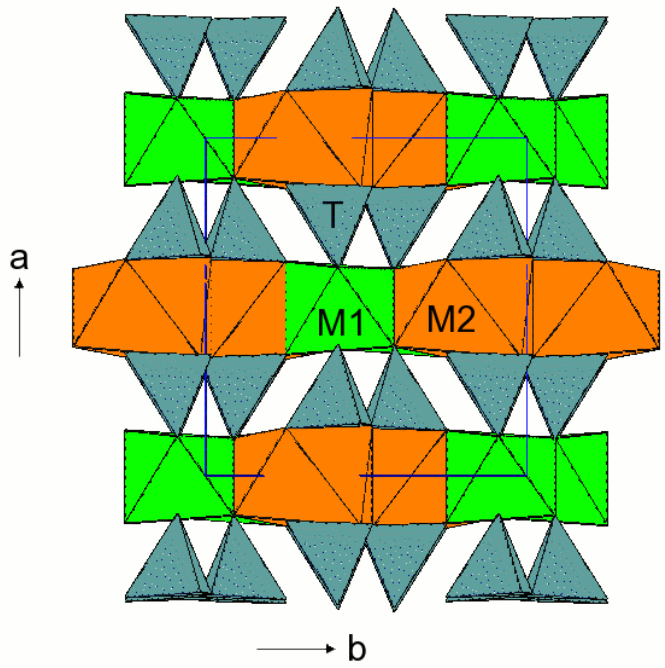

Fig.1. 1 structure of the minerals of the pyroxene group.

In particular, M1, M2-octahedral sites are occupied both by Mg cation in the case of enstatite. Both cation sites have six-fold coordination and this causes some distortion of the $[SiO_3]$ chains (Fig. 1.2)

In enstatite and other orthorhombic pyroxenes the $[SiO_3]$ chains are linked laterally by Mg or (Mg,Fe) atoms which are in position comparable, for example with those of Mg and Ca in diopside. Since both Mg and Fe are smaller than ions present in M2 sites of other

clinopyroxene, the stacking of the chain differs from that in clino and is such as to produce an orthorhombic cell with approximately double *a* dimension (Deer et al.,1966).

So far, five forms of $MgSiO_3$ have been described (see Atlas, 1952) but only three of the five have been thought to have a field of stability: the low temperature orthorhombic enstatite stable at intermediate temperature (600-1000 °C), the high-temperature protoenstatite which is stable at elevated temperatures (over 1000 °C) and which also has orthorhombic symmetry and the phase stable at low temperature (< 566 °C) clinoenstatite.

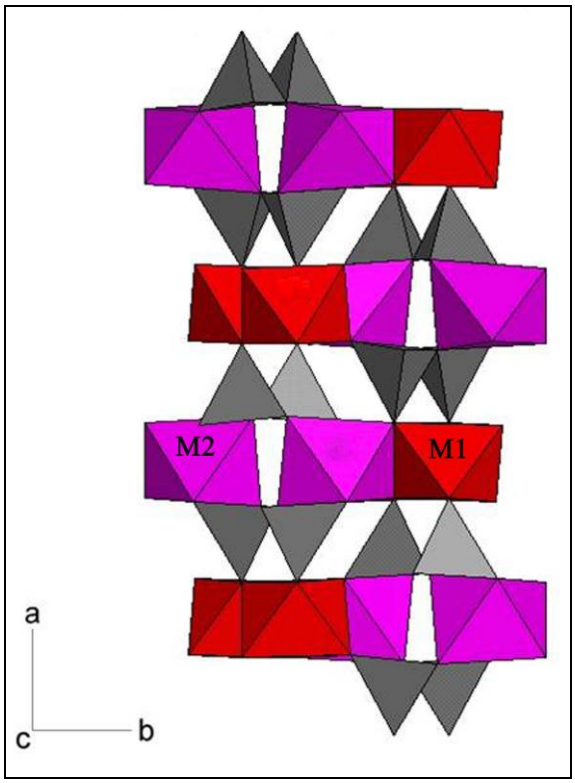

Fig. 1.2. Orthoenstatite structure, from Ghose et al., (1986)

The sequence of successive planes of Mg atoms in the direction of the x-axis can be represented as ABABAB… for clinoentatite, AABBAABB… for enstatite and AAAA… for protoenstatite. In table 1.1 are reported the unit cell parameters of the three polymorphs. The transition from one polymorph to another is related to pressure and temperature as shown in figure 1.3.

Name	Space group	a (Å)	b (Å)	c (Å)	β (°)	*V* (Å^3)	T (°C)

Clino	$P2_1/c$	9.606(1)	8.815(1)	5.169(1)	108.33(1)	415.5(1)	20
Ortho	Pbca	18.225(1)	8.815(1)	5.175(1)	---	831.3(1)	20
Proto	$P2_1cn$	9.304(4)	8.902(4)	5.351(3)	---	443.2(5)	1100

Table 1.1. Space Groups and Cell Parameters of Enstatite Polymorphs by J. Smith, 1974.

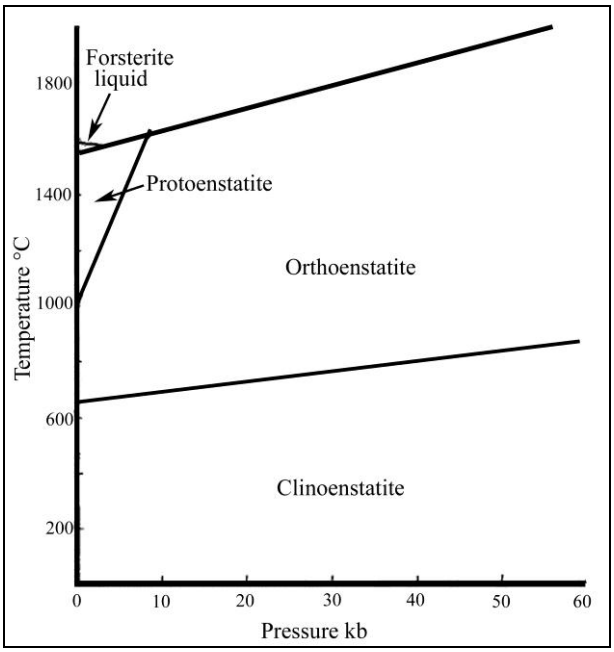

Fig. 1.3. Isochemical phase relations of enstatite, $MgSiO_3$, by Boyd & England (1965).

1.1.3 Physical and optical properties

The color of natural enstatite varies. It can be white, grey, green, yellow or brown - colorless in thin section. Enstatite has a characteristic vitreous, pearly on cleavage luster.

Enstatite typically forms prismatic crystals (Fig. 1.4a, 1.4b), lamellar, fibrous or massive ones.

They also have a prismatic cleavage that is perfect in two directions at 90 degrees; its hardness is 5–6 on the Mohs scale, and its specific gravity is 3.2–3.3.

Orthorhombic enstatite crystals are distinguished from those of the monoclinic series by their optical characteristics, such as straight extinction, much weaker double refraction and stronger pleochroism (from pale green to pale orange).

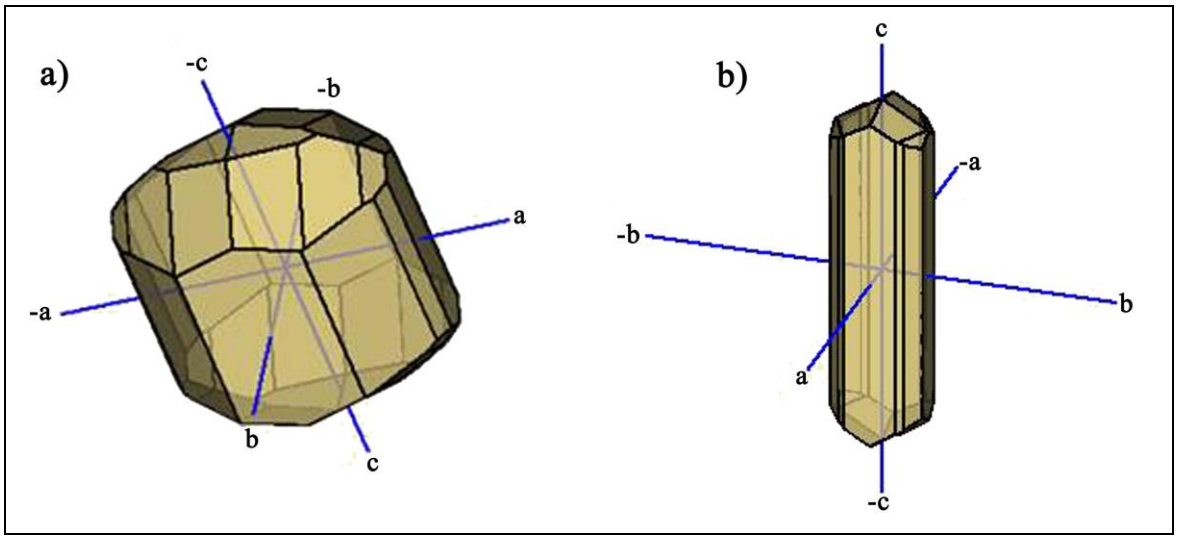

Fig.1.4. a) Short prismatic enstatite; b) long prismatic enstatite. *a*, *b*, *c* crystallographic axes.

1.1.4 Enstatite field stability in MgO-SiO_2 system

Enstatite stability limits can be represented by the phase diagram for the simple MgO-SiO_2 system (Fig. 1.5). This system was investigated by Bowen first in 1914 and Grieg after few years (1927). The growth condition of enstatite is restricted at a shallow range of composition and temperature, as estimated from MgO-SiO_2 phase diagram.

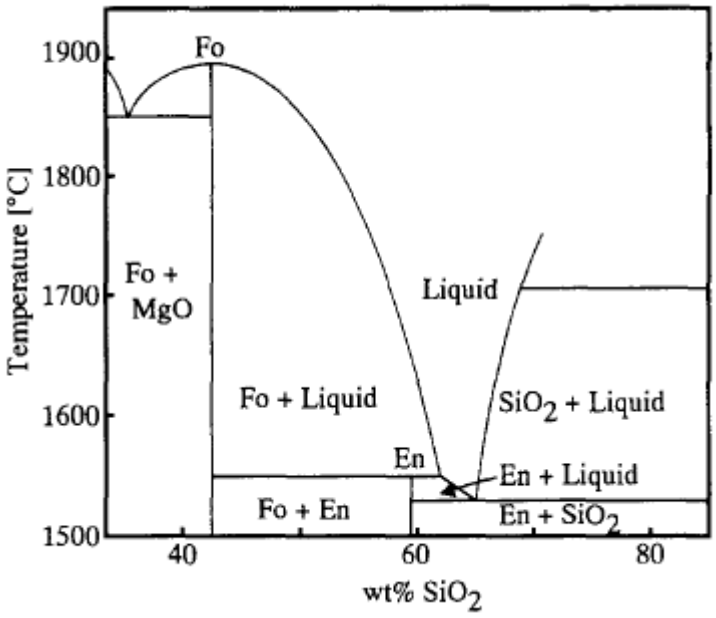

Fig. 1.5. 1. The phase diagram for the system MgO-SiOz in air, where Fo and En mean Mg/SiO, and MgSiO3, respectively. From Tanaka & Takey (1997).

1.2 Talc

Talc, ideally $Mg_3Si_40_{10}(OH)_2$, belonging to the phyllosilicate is a hydrated magnesium silicate found as a soft crystalline, foliated or compact mineral of white, grey or pale green color and soapy feel (Rayner & Brown, 1973). It occurs mainly in metamorphosed ultrabasic rocks but also by replacement of tremolite and olivine in siliceous dolomites and high-grade kyanite-talc rocks. It is the major component of economic deposits of soapstone or steatite, block of which can be used for thermal and electrical insulation. It is also used in ceramics, talcum powder and other toilet preparations, as a lubrificant, and as filler in paints, paper and rubber (Deer et al. 2009; Marzbani et al., 2013).

1.2.1 Structure of Phyllosilicates

The structure of the phyllosilicates is based on interconnected six member rings of SiO_4^{-4} tetrahedra that extend outward in infinite sheets. Three out of the 4 oxygens from each tetrahedra are shared with other tetrahedra. This leads to a basic structural unit of $T_2O_5^{-2}$, two dimensional tetrahedral sheets in which T normally is Si^{4+}, Al^{3+}, Fe^{3+}. Most phyllosilicates contain hydroxyl group, OH^-, with the OH located at the center of the 6 membered rings, as shown in figure 1.6a. Thus, the group becomes $Si_2O_5(OH)^{-3}$. When other cations are bonded to the SiO_4 sheets, they share the apical oxygens and the (OH) group which bond to the other cations in octahedral coordination. This forms a layer of cations, usually Fe^{+2}, Mg^{+2}, or Al^{+3}, that occur in octahedral coordination with the O and OH ions of the tetrahedral layer. The triangles become the faces of the octahedral groups that can bind to the tetrahedral layers (Fig. 1.6b).

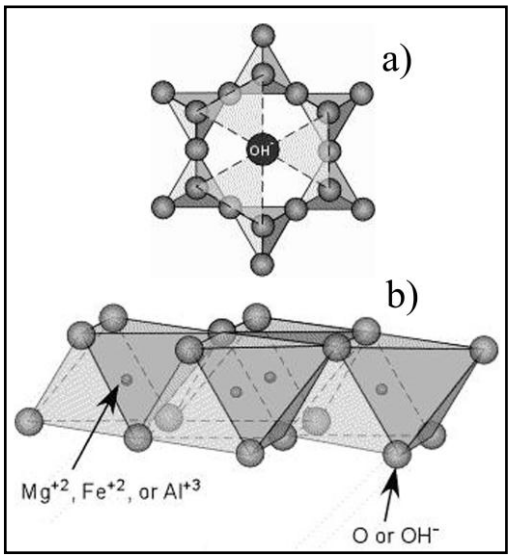

Fig. 1.6. Structure of Phyllosilicates: 1.6a) OH location at the center of the 6 membered rings; 1.6b) OH or O and cations location.

While all the tetrahedral sites are occupied in these structures, such is not necessarily the case for the octahedral sites. When the octahedral contain a divalent ion such as Mg^{2+} or Fe^{2+}, charge balance between the sheets is achieved when all sites are occupied, as illustrated in figure 1.7a. This sheet is termed a trioctahedral sheet (Brucite type $[Mg(OH)_3]$), because there are three octahedra within each hexagonal ring of tetrahedra. When a trivalent ion such as Al^{3+} or Fe^{3+} occupies the octahedra, only two thirds of the octahedra are occupied, as shown in figure 1.7b, and the sheet is termed a dioctahedral sheet (Gibbsite type $[Al(OH)_3]$) (Mottana, 1988).

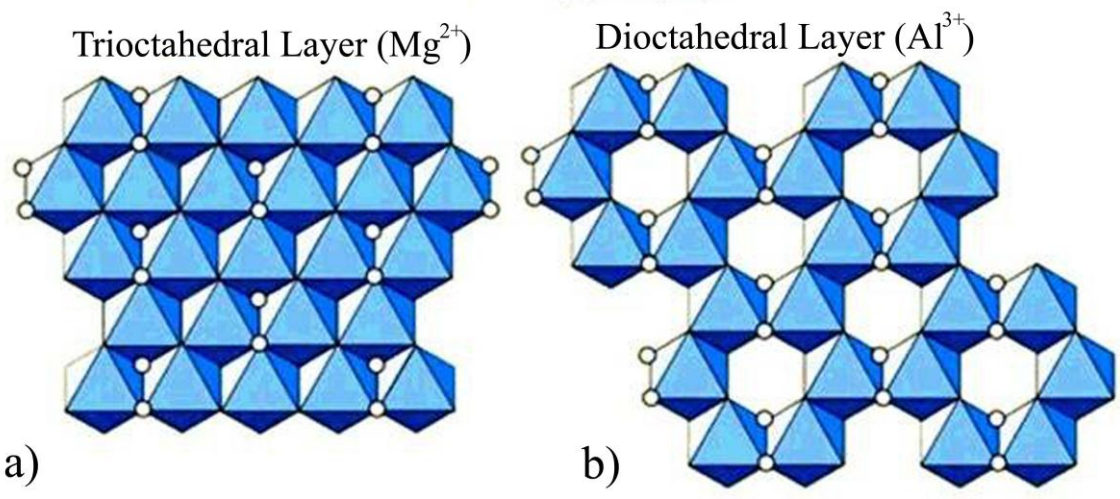

Fig. 1.7. Octahedral sheets: a) Trioctahedral Layer (Brucite type); b) Dioctahedral Layer (Gibbsite type).

Rather than terminate the external plane of oxygen atoms of the octahedral sheet by hydroxyl group, as in T-O structure, it is possible to add a second tetrahedral sheet, this one inverted with reference to the first tetrahedral sheet, making a T-O-T structure, which is the case of talc, pyrophyllite, mica, smectite and others. Finally, there are layer structures which have octahedral (hydroxide) sheets inserted between T-O-T type layers. These are known as T-O-T-O and chlorite represent this class.

A special characteristic of T-O-T phyllosilicates is the presence of a layer charge. This term refers to an excess of negative charge per formula unit that may exist in certain phyllosilicates (Bailey.,1991). The net charge may originate entirely within the tetrahedral sheet, within the octahedral sheet in some species, or may come partly form both sheets. This negative charge must be balanced by a positive charge on the interlayer so that the crystal is electrostatically neutral.

In T-O layer silicates, the interlayer bonding is via hydrogen bonds from one hydroxyl surface to the adjacent oxygen plane of the neighboring T-O. The electrostatic neutrality is

maintained and thus, the layer charge is always zero (CIT). The T-O-T layer silicates could have a net layer charge. Since such situation would be unstable because of the electrostatic repulsion between all the layers, the charge must be balanced by the presence of extra positive charge that can be situated between the layers. The chemical and physical properties are obviously strongly influenced by the layer charge.

1.2.2 Structure of Talc

The structure of talc was first described by Gruner (1934) and studied also by Hendricks (1938). Ideally, talc and pyrophillyte are the only electrostatically neutral T-O-T clay minerals. Talc is made of a central trioctahedral brucite layer composed of Mg-octahedra sandwiched in-between two hexagonal silicate tetrahedral rings. The oxygen atoms of the two remaining OH groups belong to the brucite layer, and are therefore located inside the talc slab (Fig. 1.8).

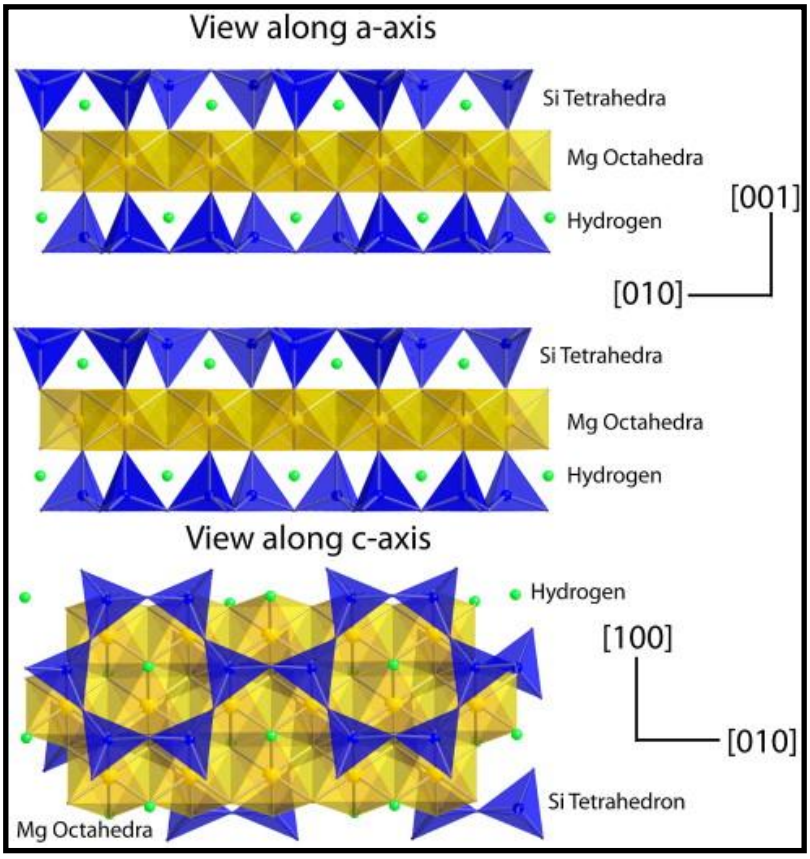

Fig. 1.8. Talc structure

The layer are held together by a combination of predominantly Lifshitz-van der Waals force (17.1 Kcal/mole) (Ward & Phillips, 1971; Giese 1978) along with a minor net ionic attraction (maximum of 4.1 kcal/mole), in spite of the insignificant layer charge (Giese 1978). These are normally thought of as weak forces, yet there is no report in the literature describing the intercalation of water or any sort of organic molecular species between the talc layers.

The layers of the structure have almost monoclinic symmetry but the nearly hexagonal rings of oxygen atoms on the surfaces of the layers, formed by the bases of the silica tetrahedral are partly displaced so that the stack of layers forms a triclinic crystal. The hexagons of surface oxygen are distorted by a 3.4° twist of the tetrahedra so that the b axis is 0.2 per cent shorter than in a structure with regular hexagons, and the twist brings the oxygen ions a little closer to the octahedral magnesium ions (Rayner & Brown, 1973). Further refinement of the structure, including the location of hydrogen atoms, was carried out by Perdikatsis & Burzlaff (1981), who found that although the symmetry of a single layer of the structure is very nearly monoclinic, the stacking of successive layers reduces this to triclinic. Cell parameters were given as a = 5.293 Å, b = 9.174 Å, c = 9.461 Å, α = 90.47° β= 98.69° γ = 90.03°.

1.2.3 Physical and optical properties

The color of natural talc varies. It can be colourless, white, pale blue or green and brown (Deer et al., 2009). Talc has a characteristic silvery or pearly luster. Upon grinding, however, all talcs yield a gray to white power with varying degree of dry brightness.

The crystal form of talc may be platelike (lamellar), foliated (leafy) (Fig. 1.8a), fibrous (acicular) (Fig. 1.8b, 1.8c), or massive.

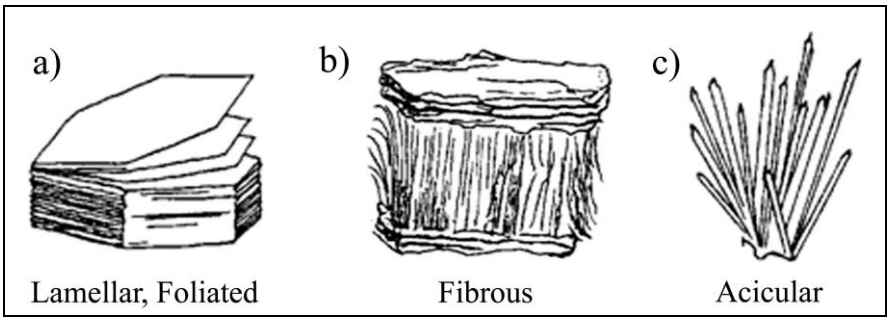

Fig. 1.9. Some talc habits. (From Klein, C., 1994, Mineral and rocks. Exercises in Crystallography and Hand Specimen Petrology, New Yoerk, Wiley. P. 305).

Talc exhibits perfect cleavage along (001) plane of symmetry, yielding flexible, slightly elastic, lamellae (Deer et al., 2009). Talc is taken as one of the standard of hardness, having the value 1 on the Mohs scale. It is infusible and inert to acids. Although talc has a marked affinity for certain organic chemicals, it generally has very little chemical reactivity. It is neither explosive nor flammable. Moreover, talc is a non-conductor of electricity and, thus, it is used in the manufacture of high frequency electrical insulators. It has low thermal conductivity and high resistance to thermal shock.

1.2.4 Chemistry

There is generally only minor departure from the end-member formula $Mg_3Si_4O_{10}(OH)_2$. Small amount of Al, Cr or Ti may substitute for Si and small amount of Mn or Al and Fe may substitute for Mg. Very small amount of Ca, Na and K may also substitute for Mg, but in several cases these elements may represent only impurities. Minor amount of Ni are often found in talc associated with ultrabasic rocks, while ferrous iron was detected in hydrothermal talc.

1.2.5 Talc field stability in the system MgO-SiO_2-H_2O

Talc maximum stability limits can be represented by the phase diagram for the simple MgO-SiO_2-H_2O system (Fig. 1.9). This system was investigated by Bowen & Tuttle (1949), and as a part of the system MgO-Al_2O_3-SiO_2-H_2O (MASH) by Yoder (1952). Talc alone is stable over almost the entire metamorphic range of pressure-temperature conditions. It can be synthesized at up to 800° C from mixture of MgO and SiO_2 at water vapour pressures of 200-1000 bar.

However, talc was hydrothermally synthesized by Koshimizu et al., (1981) at 550° C and 500 Kg/cm^2 $P_{(H2O),}$ while Ishida (1990) obtained talc at 550° C and 2 kbar.

Evans & Guggenheim (1988) calculated the P-T diagram that shows the talc stability in the system MgO-SiO_2-H_2O. This diagram confirmed that talc breaks down at or below 800° C (Fig.1.10).

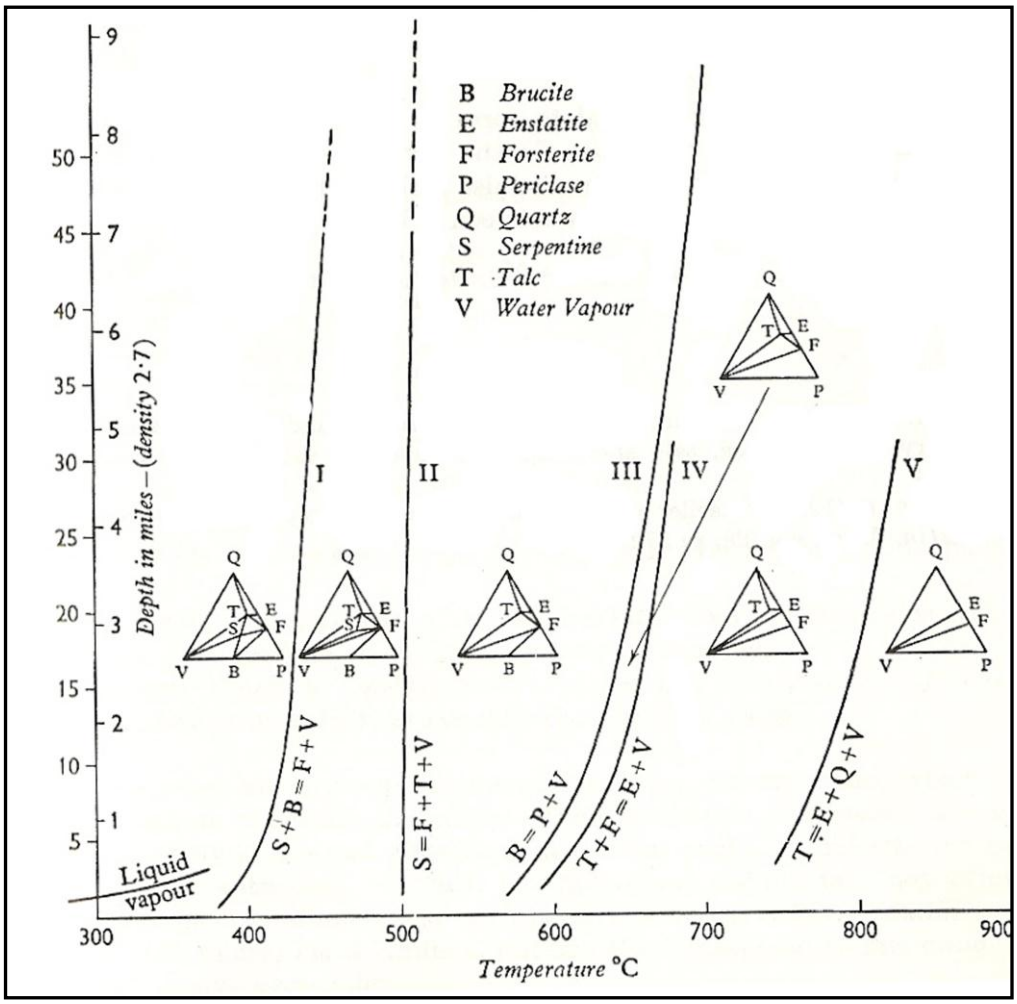

Fig. 1.10. Pressure-temperatures curves (I-V) of univariant equilibrium in the system MgO-SiO2-H2O. Equation of each curve indicates the reaction to which the curve refers. Triangular diagram on each divariant region between curves indicates, for all composition, the stable assemblages under the range of P,T condition represented by the region.

Chapter 2. Material and methods

2.1 Vertical furnace apparatus

Enstatite crystals have been grown by *flux growth technique* using a furnace equipped with Super Kanthal heating element (0 °C–1700 °C), with temperature controlled by PtRh–PtRh thermocouples (precision ±4 °C). The pot furnace consists of a single spiral tube containing a precoiled wire. Choice of wire depends on the temperature required; platinum is used above 1200 °C; below that temperature, other wires are also suitable. The design for these furnaces is shown in figure 2.1,

Fig. 2.1. Vertical furnace apparatus

2.2 Externally- heated pressure vessels

Talc synthesis was performed in *hydrothermal condition* using externally- heated pressure vessels (autoclave) which can be used up to about 10 kbar gas pressure (commonly water) at temperature of about 750 °C and at much higher temperatures under lower pressure.

The vessel used in our experiment was of a Tuttle-type (Edgar, 1973). This is consists of a long vessel in which the open end and seal are outside the furnace. An advantage of this design in contrast with the first Tuttle-type vessel is that the cone-in-cone seal is held in place by a right-hand threaded nut cap. When this cap is tightened, pressure is exerted on a left-hand threaded sleeve on the end of the nipple on the closure stem. Pressure is transmitted to the sample, which is contained in a sealed capsule, through a hole in the

closure. Temperature is measured either by placing a thermocouple in a well in the side or base of the vessel as close as possible to the sample. (Fig. 2.2).

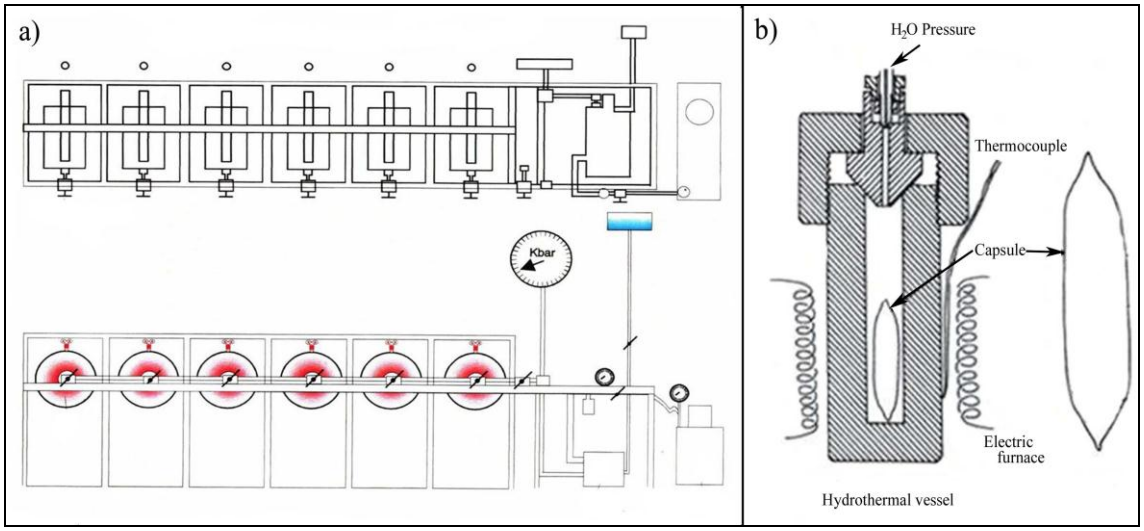

Fig. 2.2. a) Hydrothermal apparatus; b) hydrothermal vessel.

2.3 Choice of starting materials.

The preparation of samples to be used as starting material is of prime importance.

The importance of choosing correct starting-material is reported by Fyfe (1960).

The choice of the starting material depends on the number of factors, including the nature of the problem to be investigated, the availability of sufficiently pure components, the availability of equipment. The first problem in synthetic experiments it is the necessity to use sufficiently reactive starting materials, with high free energies, in order to induce the desired reaction in a reasonable length of time. The most reactive materials are also those that are most likely to produce metastable phases. Thus, it is important to use starting-materials with the lowest free energies in order to achieve the stability. Another problem is that of hydrated compounds in which the percentage of H_2O often differs from the theoretically expected value. All reagents should therefore be dried and desiccated to prevent hydration. Moreover, the use of platinum containers are necessary to avoid the contamination and in case of very high temperature.

Finally, the particle size of the material must also be considered. Starting- materials must be sufficiently fine-grained to ensure homogeneity and to provide large surface areas for reaction in a reasonable time, but at the same time, they should not be excessively fine-grained because disequilibrium results could be produced.

Four types of starting materials are commonly used in experimental investigations: i) glasses; ii) gels; iii) dry mixtures of oxide and other compound; iv) natural minerals and rocks.

In the present case, the starting materials consisted of dry mixtures of oxides and other compounds. In particular, the following nutrients were used:

A) Granular quartz (SiO_2; Carlo Erba reagent, code No. 364011);

B) Magnesium oxide (MgO; Carlo Erba reagent, code No. 459586);

C) Manganese oxide (MnO; Aldrich reagent, code No. 8849);

D) Zinc oxide (ZnO; Merck reagent, code No. 8849).

All starting materials used in experiments had a purity exceeding 99%. In addition, different types of reactants such as i) H_2O; ii) $CaCl_2$ (pH = 7); iii) HCl (pH = 5) were exploited in case of preparation of samples for hydrothermal synthesis. To increase the reactivity between nutrients, starting oxides were preheated in a vertical furnace.

1) SiO_2: selected high-purity quartz is generally recommended as a source of SiO_2. The quartz is crushed to about 60 mesh in a agate mortar. The crushed and purified quartz is then placed in a platinum crucible, and roasted for about 2 hours at 1600 °C, to remove any liquid inclusion and then rapidly quenched. Thus, quartz is converted into cristobalite and desiccated until required.
2) MgO: pure oxide is used as a source of MgO. It should be ignited at 1050 °C for 2 hours in order to remove moisture and carbonate. It is kept desiccated.
3) MnO and ZnO are heated at 110 °C and keep at this temperature in order to eliminate hygroscopic content (Edgar, 1973).

2.3.1 Choice of a transition metal-ion dopant

The selection of candidate transition metal ions for incorporation in the enstatite and talc structures was made after thorough screening of the existing literature. Primary criterion for the choice of a transition metal-ion dopant was the similarity in ionic size in an octahedral field of O^{2-} anions. The ions were selected such that the effect of oxidation state and electronic configuration could also be evaluated. Based on the above guidelines, Zn^{2+} and Mn^{2+} were identified as suitable candidates for this study.

2.4 Characterization techniques

The doped enstatite crystals after the separation from the solidified flux by sonication in hot water, were recovered under a stereo binocular microscope (20 x) for a preliminary

analyses. Successively, the products were characterized and studied by powder crystal X-ray diffraction (XRPD), scanning electron microscopy with energy-dispersive spectrometry (SEM/EDS), single-crystal X-ray diffraction (XRD), micro-Raman and cathodoluminescence (CL).

After hydrothermal treatment, capsules are carefully opened with the help of pincers and the products were analyzed by XRPD, SEM-EDS, Fourier transform infrared (FT-IR), differential scanning calorimetry and thermogravimetric analysis (DSC-TG).

2.4.1 X-ray powder diffraction (XRPD)

Crystals were identified by x-ray powder diffractometer (Bruker D8 Advance) with Cu-*Kα* radiation, operating at 40 kV and 40 mA. Scans were collected on powder samples in the range of 3-60° 2θ, step interval 0.02° 2θ, step-counting time 3 s. EVA software (DIFFRACplus EVA) was used to identify the mineral phases in each X-ray powder spectrum, experimental peaks being compared with 2005 PDF2 reference patterns.

2.4.2 Single-crystal X-ray diffraction (XRD)

Single crystals were mounted on a Bruker-Nonius X8APEXII CCD area detector system and used for data collection. Diffraction data were collected at room temperature with graphite-monochromated Mo-K_α radiation (λ = 0.71073 Å). Data frames were collected with a narrow-frame method with scan widths of 0.3° in omega, exposure time 5 s per frame, and crystal-to-detector distance 40 mm.

2.4.3 Scanning electron microscopy with energy-dispersive spectrometry (SEM/EDS)

The chemical composition and morphology of the crystals were investigated by energy dispersive spectroscopy (EDS) with a field-emission scanning electron microscope (SEM, FEI Quanta 200). Crystal compositions were determined on cross-sections, well polished and C-coated.

2.4.4 Micro-Raman (μ-R)

A confocal microprobe apparatus was used for micro-Raman investigation: an Olympus microscope interfaced to a triple monochromator (Horiba-Jobin Yvon, model T64000), mounting holographic gratings having 1800 lines/mm, set in double-subtractive/single configuration, and equipped with a CCD (256x1024 pixels) detector, cooled by liquid

nitrogen. Polarized micro-Raman spectra were collected at room temperature from 180° scattering geometry, mostly in parallel XX polarization, under excitation of different lines of a mixed gas Ar-Kr laser, the maximum output laser power, for the 514.5 nm line, was 20 mw. An objective of magnification 80X was used to focus the laser beam onto the sample surface. Moreover, in order to reduce the background scattering, a confocal approach with an iris aperture of 2 μm has been adopted. To check the calibration of the triple-monochromator, spectra of the Kr/Ar laser secondary emissions were recorded, and their energy position was compared the reported one in the NIST database [Kramida, A., Ralchenko, Yu., Reader, J., and NIST ASD Team (2012). NIST Atomic Spectra Database (ver. 5.0), [Online]. Available: http://physics.nist.gov/asd [2013, July 8]. National Institute of Standards and Technology, Gaithersburg, MD.]. The mismatch of our measurements, was of about 0.7 cm^{-1} for a Raman shift of about 1100 cm^{-1} on the Stokes side, allowing an straightforward re-calibration of the recorded values.

The Raman spectrum of pure enstatite was used as internal benchmark, in view of the evaluation of the spectral effects induced by the doping ions.

Raman spectra were collected on single crystals.

2.4.5 Cathodoluminescence (CL)

Cathodoluminescence (CL) measurements were carried out on a Cambridge Stereoscan 360 SEM, equipped with a Horiba Jobin Yvon VS140 UV-VIS spectrometer with spectral resolution of ~ 1 nm. SEM operating conditions were: 20-40 kV of accelerating voltage, 1 μA for the emission current, 12.5 Hz for the scanning frequency, an acquisition time of 40s, and scanning area ranging from 0.1 to 0.4 mm^2. Our interest has been focused on qualitative spectral changes at room temperature.

2.4.6 Fourier transform infrared (FT-IR)

The infrared spectra were acquired using a Thermo Nicolet iS50 Fourier Transform Infrared Spectrophotometer (FT-IR) operating in ATR mode; a built-in diamond ATR equipped with a dedicated DTGS detector allows to analyze samples in the MID-FAR infrared range (5000-100cm^{-1}); 64 interferograms, with a resolution of 4 cm^{-1} were collected for each sample.

2.4.7 Differential scanning calorimetry and thermogravimetric analysis (DSC-TG).

Thermogravimetric and differential scanning calorimetry (TG-DSC) were performed in an alumina crucible under a constant nitrogen flow of 30 cm^3min^{-1} with a Netzsch STA 449 C Jupiter in a 25 - 1000 °C temperature range, with a heating rate of 10 °C/min. Instrumental precision was checked by six repeated collections on a kaolinite reference sample revealing good reproducibility (instrumental theoretical T precision of ± 1.2 °C) and theoretical weight sensitivity of 0.10 Vg.

Chapter 3. Enstatite and talc synthesis procedure

3.1 Grow of enstatite by flux method

During the years, pure and doped enstatite has been grown in several different ways (e.g., Czochralski, flux methods, sol–gel, co-precipitation, etc.; (Grandin de Le´ previer, 1983; Ushio et al.,, 1991; Tanaka & Takey., 1997 ; Stalder, 2002; Goel et al., 2007). Here, it was chosen to grow pure enstatite and Zn- and Mn-doped enstatite single crystals by flux method for the following reasons: i) structure determination and intrinsic property measurements are preferably, sometimes exclusively, carried out on single crystals; ii) for certain applications, most notably those which rely on optical and/or electronic properties (laser crystals, semiconductors, etc.), single crystals are necessary.

Single crystals of orthoenstatite were synthesized with the flux method described by Grandin de l'Eprevier (1972) and used by J. Ito (1975). From that moment numerous researchers started to synthesize enstatite in order to study its geophysical properties that could give a significant contribution to understand dynamic processes in the mantle (Tanaka & Takey, 1997). After the discovery of some important properties such as high refractoriness, high strength and toughness, low dielectric constant, enstatite crystals have been used as insulators at high frequencies and reinforced components (Beall, 1993; Holand & Beall,2012); and more recently, as biorestorations in enstatite based-ceramics (Goel et al., 2007). In addition, with the discovery of the luminescence spectroscopic properties of enstatite single crystals doped with metal elements, interest in them has recently increased (Moncorgè et al., 1999). So far, enstatite has been doped with various methods and with varying amounts of Cr^{3+} (Cavalli & Bettinelli, 1993; Moncorgè et al., 1999), Ni^{2+} (Moncorgè et al 1999, Bloise et al., 2011), Mn^{2+} (Lin et al., 2006), Li^{+} Sc^{3+} (Smyth & Ito, 1977), and Ti (Bloise et al., 2011).

In this context, we investigated the experimental conditions required to obtain Zn-and Mn-doped enstatite single crystals by the flux growth method. Here it is reported the preparation of samples, run procedures and experimental conditions for obtaining enstatite crystals.

3.1.1 Preparation of samples and run procedures for flux growth methods.

Enstatite has been obtained using two different finely powdered fluxes as melting agent (Ito, 1975; Ozima, 1982): MoO_3, V_2O_5, Li_2CO_3 and Li_2CO_3, MoO_3. These fluxes have been

frequently used for single-crystal growth, even if other fluxes are also suitable (Ushio et al., 1991).

The flux, also called high temperature solvent, permits growth to proceed at temperatures well below the melting point of the growing phase. This is one of the main advantages of this technique compared with growth from the pure melt, because relatively lower temperature are involved in a flux growth and better quality crystals can be grown.

In the present case, the starting materials consisted in oxides such as SiO_2, MgO, ZnO and MnO that, after the pre-heating (see Chapter 2) are mix together in an agate mortar (grain size < 0.177 mm) with various molar ratios. Successively, the nutrients are mixed with the flux at a constant nutrient/flux ratio of 0.5.

The mixture is then transferred into a 50 ml platinum crucible and heated in a vertical furnace with programmable temperature controller ramp and soak. Usually, thermal runs start with a steep increment up to the temperature of melting point and held at this maximum temperature for a certain period of time (from 60 to 140 hours) for complete dissolution and homogenization of the oxide mixtures. Subsequently, slow cooling was applied down to the final temperature (e. g. 600 °C), after which temperature is decreased rapidly by plunging the crucible into a shallow dish of water to about half of the depth of the crucible (quenching). To separate the crystals from the solidified solvent, the product in the crucible is treated by sonication in hot water and recovered under binocular microscope for preliminary observations.

3.1.2 Experimental condition for the growth of enstatite crystals doped with zinc.

Zn-doped enstatite crystals with different Mg/Zn molar ratio (Table 1) have been grown by flux growth technique using two different finely powdered fluxes as melting agent (Ozima, 1982; J. Ito 1982): MoO_3, V_2O_5, Li_2CO_3, and Li_2CO_3- MoO_3. The composition of the solvents was in molar percentage: MoO_3 = 38.8, V_2O_5 =5.4, Li_2CO_3 = 46.5 (A. Bloise et al. 2009), and MoO_3= 43.1, Li_2CO_3 = 51.4.

Fourteen different runs have been performed with the aim of observing how different composition of the starting material, various cooling rate, starting cooling and cut off temperature could influence the growth of the crystals (Table 3.1).

Thermal runs A1, A2 and A3 were started with an increment up to 950 °C in 37 hours, (Table 3.1), after which the temperature was kept constant for 168 h, in order to get complete dissolution and homogenization of the mixture. The melts obtained in such a way

were then slowly cooled down to 600 °C at the cooling rate of 2.1 °C/h. The various step of cooling have been reported in the figure 3.1.

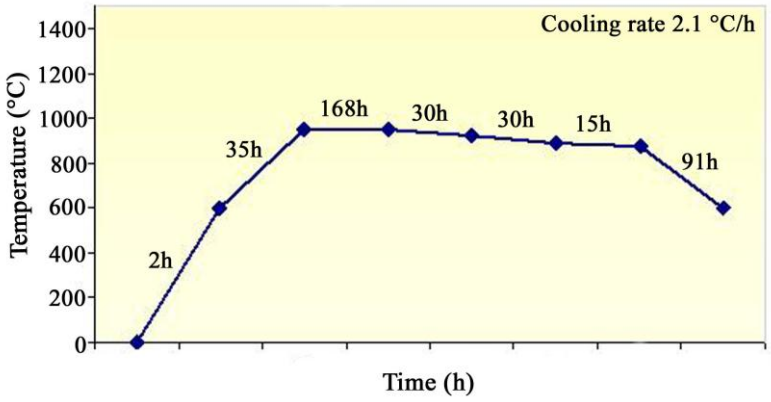

Fig. 3.1 . Steps of cooling for A1, A2 and A3 runs.

B1 and B2 runs with different content of zinc in the starting materials, have been started with a steep increment (only 10 hours) up to 1050 °C. After 144 hours of holding time, the temperature was decreased down to 650 °C at a rate of 1.7 °C/h (Fig. 3.2).

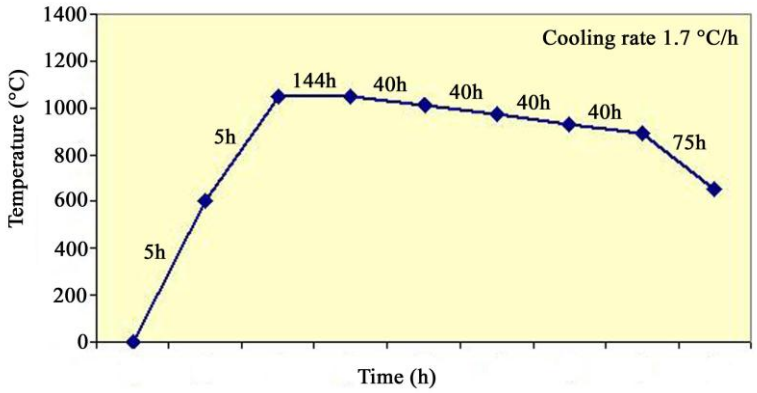

Fig. 3.2 . Steps of cooling for B1, and B2 runs.

The specimen materials (C1 and C2 runs) were heated an maintained at 1250 °C for 48 h, then slowly cooled to 700 °C at the rate of 1.8 °C/h (Fig. 3.3).

Temperature in I1, I2 and I3 runs was incremented up to 1350 °C in 8 hours and slowly decreased down to 750 °C after 48 hours of holding time. The cooling rate was about 3.7 °C/h. (Fig. 3.4).

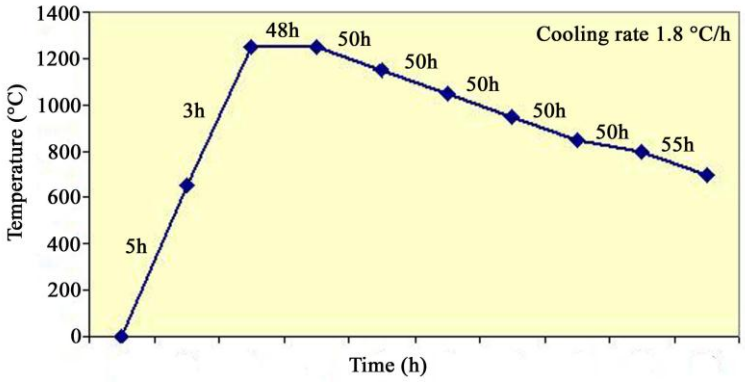

Fig. 3.3 . Steps of cooling for C1and C2 runs.

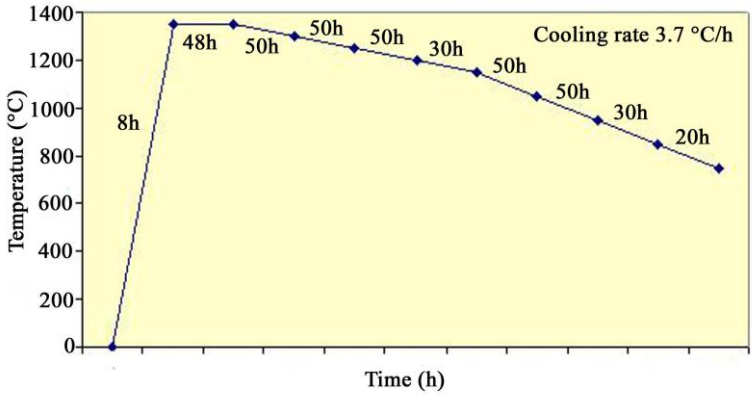

Fig. 3.4 . Steps of cooling for I1, I2 and I3 runs.

Samples D1, D2, G1 and G2 were transferred into the furnace at 1250 °C and kept at this temperature for 60 hours. Successively, they were cooled down to 700 °C at the rate of 1.6 °C/h (Fig. 3.5). No-doped enstatite (H1 run, Table1), was synthesized to be compared with the doped one.

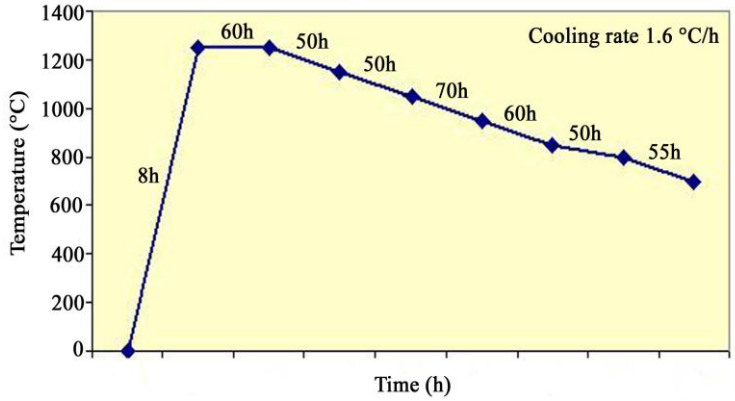

Fig. 3.5 . Steps of cooling for D1, D2, G1 and G2 runs.

In A1, A2, A3, B1, B2, I1, I3, C1, C2 and H1 runs, minerals synthesized have been grown using MoO_3, V_2O_5, Li_2CO_3 as a flux, while for I2, D1, D2, G1 and G2 runs the Li_2CO_3-MoO_3 system was used as flux.

Molar proportion of the nutrient (starting-mixture) for each run is reported in table 3.1.

Run	Nutrient (molar ratio)			Flux	Starting cooling T(°C)	Cooling rate (T/h)	Cut off temperature (°C)
	MgO	SiO_2	ZnO				
H1	1.00	1.00	-	*	1350	3.7	750
A2	0.80	1.00	0.20	*	950	2.1	600
A1	0.60	1.00	0.40	*	950	2.1	600
A3	0.50	1.00	0.50	*	950	2.1	600
B2	0.40	1.00	0.60	*	1050	1.7	650
B1	0.20	1.00	0.80	*	1050	1.7	650
C1	0.80	1.00	0.20	*	1250	1.8	700
C2	0.50	1.00	0.50	*	1250	1.8	700
I1	0.75	1.00	0.25	*	1350	3.7	750
I3	0.25	1.00	0.75	*	1350	3.7	750
I2	0.50	1.00	0.50	§	1350	3.7	750
D2	0.80	1.00	0.20	§	1250	1.6	700
D1	0.50	1.00	0.50	§	1250	1.6	700
G1	0.30	1.00	0.70	§	1250	1.6	700
G2	0.00	1.00	1.00	§	1250	1.6	700

Table 3.1. Molar ratios of the starting-mixtures and experimental conditions. (*Flux composition MoO_3, V_2O_5, Li_2CO_3; §Flux composition MoO_3, Li_2CO_3).

3.1.3 Experimental condition for the growth of enstatite crystals doped with manganese.

Mn-doped enstatite was grown by using a lithium-vanadomolybdate flux (Ozima 1982, Ito 1982, Bloise et al., 2009). In table 3.2 it is reported the experimental conditions and the molar proportions of the starting oxide mixtures.

The nine runs can be divided into three groups according to the cooling rate.

EN1 and EN2 runs were started with an increment up to 1350 °C and kept at this temperature for 100 h. Subsequently, the temperature was decreased down to 750 °C at a rate of 3.7 °C/h (Fig. 3.4; note that the holding time is not the same as the one used for I1, I2 and I3 runs).

Starting-mixtures EN3, EN4, EN5 were heated and maintained at 950 °C for 60 h and then slowly cooled down to 600 at a rate of 2.1 °C/h (Fig. 3.1; note that the holding time is not the same as the one used for A1, A2 and A3 runs).

The slowest cooling rate (1.7 °C/h) was used for EN6, EN7, EN8, EN9 runs, for which the temperature was increased up to 1050 °C and then cooled down to 650 °C (Fig. 3.2).

Run	Nutrient (molar ratio)			Flux	Starting cooling T(°C)	Cooling rate (T/h)	Cut off temperature (°C)
	MgO	SiO_2	MnO				
H1	1.00	1.00	-	*	1350	3.7	750
EN1	0.50	1.00	0.50	*	1350	3.7	750
EN2	0.75	1.00	0.25	*	1350	3.7	750
EN3	0.60	1.00	0.40	*	950	2.1	600
EN4	0.25	1.00	0.75	*	950	2.1	600
EN5	0.00	1.00	1.00	*	950	2.1	600
EN6	0.50	1.00	0.50	*	1050	1.7	650
EN7	0.60	1.00	0.40	*	1050	1.7	650
EN8	0.40	1.00	0.60	*	1050	1.7	650
EN9	0.00	1.00	1.00	*	1050	1.7	650

Table 3.2. Molar ratios of the starting-mixtures and experimental conditions. (*Flux composition MoO_3, V_2O_5, Li_2CO_3).

It is important to underline that, despite the slight difference among the four cooling rate used in these experiments (3.7 °C/h, 2.1 °C/h, 1.8 °C/h, 1.7 °C/h and 1.6 °C7h), there is a big difference between one cooling and another; indeed, each run is made of various steps and different holding times as shown in figures 3.1-3.5.

3.2 Talc grow by hydrothermal methods

Talc is widely used in different workplaces as roofing, plastics, cosmetics and as a filler in many industrial applications such as paper, paint, ceramics and polymers (Menczel & Varga, 1983; Ferrage et al., 2002; Marzbani et al. 2013) .

In natural talc, moderate amounts of foreign cations (e.g. Fe, Ni, Mn) are found to occupy the octahedral sites, while small amounts of Al, Cr and Ti may substitutes for Si [W. A. Deer, 2009]. The usual presence of these foreign ions (i.e. Fe, Ni, Al, etc.) in natural talc and their inconstant amounts may inhibit the high-performance of this mineral as reported by Marzbani et al., (2013). For these reasons, pure and doped talc was synthesized mainly hydrothermally using different starting materials and experimental conditions (Wilkins & Ito, 1967; Ishida 1990; Bose & Ganguly, 1994; Kirak et al., 1999; Martin et al., 1999;). So far, Ni-, Co-, Fe-, S-, O-, MgO-, $Mg(NO_3)^{2-}$ and Mn-doped talc has been synthesized mainly to study its chemical and physical properties (e. g. electric conductivity) (Wilkins & Ito, 1967; Ishida, 1990; Bloise et al., 2010; Kirak et al., 1999; Pidluzhna et al., 2012). In this context, we investigated the experimental conditions required to obtain pure, Zn-and Mn-doped talc crystals by hydrothermal method using oxide mixtures as starting materials and distilled water as main reactant (Bose, 1994). Here it is reported the preparation of samples, run procedures and experimental conditions for obtaining talc crystals.

3.2.1 Preparation of samples and run procedures for hydrothermal methods.

After pre-heating (see Chapter 2), nutrients (SiO_2, MgO, ZnO and MnO powder oxides) are mixed together according to stoichiometry of the talc.

The prepared samples are enclosed in a sealed noble-metal capsule (e.g. platinum) together with volatile phase, usually distilled water or distilled water with the addition of some reactants. The starting-material is inserted into the capsule with a small spatula and a funnel.

The water or reactants are added to the weighed sample capsule by a microsyringe. The capsules are usually in platinum or gold because they are inert to most starting-materials, malleable and easily welded. A capsule is about 0.11 cm^3 in volume, the walls must to be thick enough to avoid the bursting under pressure.

The filled capsule will be welded with an arc-welder and put to react in externally heated pressure vessel. Welding a filled capsule is considerably more difficult that an empty one,

because materials may be lost either by spattering of the metal or by evaporation of the water. After welding, the capsule is examined to avoid the presence of possible holes, weighed, dried and finally placed in the pressure vessel.

The vessel is attached to the pressure line and the required pressure applied. If there are not any leaks, the vessel is placed in the furnace. As the temperature rises, the excess pressure should be bled from the vessel by cracking a dump valve in the system.

Pressure is transmitted to the sample by collapse of the walls of the capsule when the external pressure is applied. After several hours or days (depending on the experiments) during which the capsule is maintained at the same temperature and pressure, the vessel is removed from the furnace and, at run pressure, it is quenched initially by applying a jet of air to the bottom of the vessel and then by water for the final cooling. When the vessel reached the room temperature, the pressure is released by opening the dump valve and the capsule are removed, dried and reweighed. If the capsule has changed its weight, it should be discarded; otherwise, it can be carefully opened in order to recover the products.

3.2.2 Experimental condition for the growth of talc doped with zinc.

Eleven different runs have been performed with the aim of observing how different composition of the starting material and temperature of growth could influence the growth of the crystals when pressure and time of reaction is maintained constant (Table 3.3).

All runs were maintained for 160 h in the vessel under a constant pressure of 2 kbar.

About 80 mg of finely powdered starting mixture prepared according to the stoichiometry of talc, was mixed with three different types of reactant in amount between 4 wt% and 16 wt%:

i) H_2O;

ii) $H_2O + CaCl_2$ (pH = 7);

iii) $H_2O + HCl$ (pH = 5)

Runs T1P, T2e, T3f, T4 were treated with an excess of water, three time the amount of the water present as crystalline water in the natural talc.

T2Ca and T3Ca were altered with a neutral solution made of water and calcium chloride.

T2HCl and T4HCl were treated with an acidic solution (pH=5).

Water was added four times the normal amount of the water present as crystalline one in the natural talc in the TZn1 and T2P runs.

Run	Molar ratio		T (°C)	Pressure (kbar)	Time (h)	Reactant
	MgO	ZnO				
T1P	3	0	650	2kbar	160	H_2O 12%
T2e	2	1	650	2kbar	160	H_2O 12%
T3f	1.5	1.5	650	2kbar	160	H_2O 12%
T4	0	3	650	2kbar	160	H_2O 12%
T2Ca	2	1	650	2kbar	160	H_2O + $CaCl_2$ 12%
T3Ca	1.5	1.5	650	2kbar	160	H_2O + $CaCl_2$ 12%
T2HCl	2	1	650	2kbar	160	H_2O + HCl 12%
T4HCl	0	3	650	2kbar	160	H_2O + HCl 12%
T2a	2	1	500	2kbar	160	H_2O 4%
T2b	2	1	500	2kbar	160	H_2O 12%
T2c	2	1	300	2kbar	160	H_2O 4%
T2d	2	1	300	2kbar	160	H_2O 12%
TZn1	2	1	650	2kbar	160	H_2O 16%
T2P	2	1	650	2kbar	160	H_2O 16%

Table 3.3. Molar ratio of the starting-mixtures and experimental conditions.

3.2.3 Experimental condition for the growth of talc doped with manganese.

Preliminary 4 runs have been performed in order to obtain Mn-doped talc under the same experimental conditions used for the yield of Zn-talc. The content of manganese in the starting mixture was incremented from 0.25 in molar ratio, to a complete substitution of magnesium by manganese (Table 3.4).

Run	Molar ratio		T (°C)	Pressure (kbar)	Time (h)	Reactant
	MgO	MnO				
T1P	3	0	650	2kbar	160	H_2O 12%
AC1	2.75	0.25	650	2kbar	160	H_2O 12%
AC2	2	1	650	2kbar	160	H_2O 12%
AC3	1.5	1.5	300	2kbar	160	H_2O 12%
AC4	0	3	300	2kbar	160	H_2O 12%

Table 3.4. Molar ratio of the starting-mixtures and experimental conditions.

The experiments were all conducted at neutral pH and at constant pressure and time.

Chapter 4. Results and Discussion

4.1 Enstatite doped with zinc

The doped enstatite crystals after the separation from the solidified flux by sonication in hot water were recovered and selected under a binocular microscope (20 x).

Optical inspections and X-ray powder diffraction analyses of all products revealed that, in addition to Zn-doped enstatite, other phases were grown. The minerals produced for each run, with the average of zinc content, maximum length and length and width average of Zn-doped enstatite crystals are reported in table 4.1.

Run	Nutrient (molar ratio)			Flux	Minerals produced	Average ZnO in enstatite (wt. %)	Max length enstatite (mm)	Average length enstatite (mm)	Average width enstatite (μm)
	MgO	SiO_2	ZnO						
H1	1.00	1.00	-	*	Mg-En, Qtz	-	-	0.9	500
A2	0.80	1.00	0.20	*	Zn-En, L-W	3.57	1.5	1	300
A1	0.60	1.00	0.40	*	Zn-En, Qtz, L-W	3.37	1.3	1	500
A3	0.50	1.00	0.50	*	Zn-En, L-W, Qtz	3.48	1.4	0.8	250
B2	0.40	1.00	0.60	*	Zn-En	10.49	2.6	1.3	200
B1	0.20	1.00	0.80	*	Qtz, L-W	-	-	-	-
C1	0.80	1.00	0.20	*	Qtz, L-W, Zn-En	4.53	3.5	1	300
C2	0.50	1.00	0.50	*	Qtz, Zn-En, L-W	4.45	1	0.8	240
I1	0.75	1.00	0.25	*	Zn-En, Qtz	4.43	2.2	1.2	350
I3	0.25	1.00	0.75	*	Qtz, L-W	-	-	-	-
I2	0.50	1.00	0.50	§	Qtz, L-W	-	-	-	-
D2	0.80	1.00	0.20	§	Qtz, L-W	-	-	-	-
D1	0.50	1.00	0.50	§	L-W, Qtz	-	-	-	-
G1	0.30	1.00	0.70	§	L-W, Qtz	-	-	-	-
G2	0.00	1.00	1.00	§	L-W	-	-	-	-

Table 4.1. Molar ratios of the starting nutrient mixtures and products obtained. Zn-En = Zn-doped enstatite; Qtz = Quartz; Mg-W = Mg-doped willemite; L-W = Li_2ZnSiO_4-Zn_2SiO_4 solid solution. (*Flux composition MoO_3, V_2O_5, Li_2CO_3; §Flux composition MoO_3, Li_2CO_3).

As it is shown in table 4.1, enstatite was obtained in different amounts only in solvents of the system MoO_3- V_2O_5- Li_2CO_3. Indeed, when MoO_3 - Li_2CO_3 was used as a flux, no enstatite was produced, due to the lack of sufficient starting materials solubility according to Smyth and Ito (1977). Probably, the low concentration of SiO_2 in the melt constrains the composition of the starting mixture towards the formation of other phases such as Li_2ZnSiO_4 in agreement with the Li_2O-ZnO-SiO_2 system reported in figure 4.1 (West, 1980).

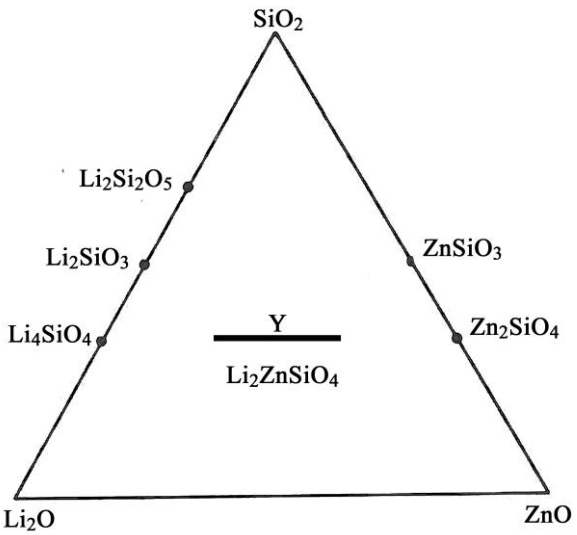

Fig. 4.1. Occurrence of Li_2ZnSiO_4 solid solutions (hatched) in the system Li_2O-ZnO-SiO_2. Compositions in mole percent, (A. R. West, 1980).

Run products (H1, A1, A2, A3, B2, C1, C2 runs) consisted of approximately 50 wt. % enstatite crystals and side-products and 50 wt. % quenched solute from the fluid, which appeared as yellow/white, soft material that could easily be removed from the crystal surfaces. In some runs it occurred that crystals were assembled together, and even in those cases, the aggregates could be mechanically separated. The most abundance of enstatite was obtained from I1 and B2 runs.

Zn-enstatite crystals are colorless and all appear to be idiomorphic, commonly without defects and elongated along the c-axis (Fig. 4.2). Inspections of the recovered enstatite crystals revealed that they were virtually free of fluid inclusions. In some rare specimens, veins occurred, which were open towards both ends and contained some quench material.

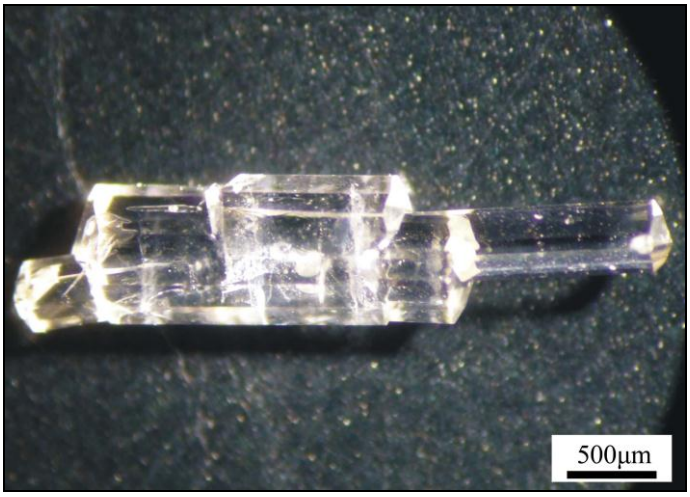

Fig. 4.2. Optical image of transparent crystals of Zn-doped enstatite (run B2).

4.1.1 XRPD characterization

According to the XRPD patterns, the most intense diffraction peaks of Zn-doped enstatite consisted of orthoenstatite (OR-EN) (JCPDS 22-0714) associated with clinoenstatite (CL-EN) (JCPDS 35-610).

As predicted by Grover (1972), CL-EN may have its own field of stability in the absence of shear below 566 °C. In our case, CL-EN was detected in all runs even if the syntheses were conducted in the range of temperature from 1350 to 600 °C (stability field of OR-EN, Fig. 4.3), and the quenching was done above 600 °C.

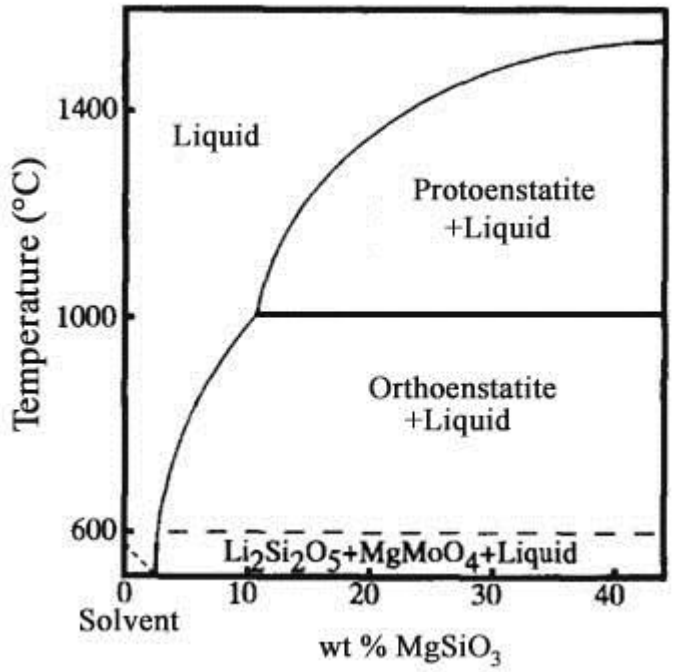

Fig. 4.3. Stability field of orthoenstatite and phase relation between lithiumvanadomolybdate and $MgSiO_3$ in air reported by Ito.

The presence of CL-EN could be explained in many different ways. Indeed, CL-EN can form from OR-EN in a variety of ways. Turner et al., (1960) have shown that shearing favors CL-EN, while the data are contradictory regarding whether OR-EN or CL-EN is stable at low temperatures in the absence of shear, although OR-EN appears to be favored (Grover,1972).

Moreover, the growth of CL-EN could be associated with fast cooling, as obtained by Ushio et al. 1991, but it was excluded because enstatite was of clino-type even when the cooling rate was very slow (1.7 °C/h).

Moreover, as predicted by Smyth (1974), slower cooling through the range 700-600 °C (as in our case) produced crystals containing about 50% OR-EN.

The presence of CL-EN together with OR-EN by quenching between 750 and 600 °C, is probably due to the shearing of OR-EN**.** In fact, Turner et al., (1960) suggested that CL-EN is a good stress indicator and numerous subsequent studies have confirmed that it can be produced from OR-EN by shearing. Such a reaction occurs at temperatures below the prothoenstatite stability field and thus is represented as OR-EN – CL-EN.

Other phases are found to be present in different quantities: quartz and a solid solutions that occur between Li_2ZnSiO_4 and Zn_2SiO_4; their general formula may be written $Li_{2-2x}Zn_{1+x}SiO_4$.($0 < x < 0.5$) (Table 4.1). The formation of these phases together with enstatite was probably due to the decrease of flux acidity with increasing contents of ZnO. Thus, SiO_2 solubility decreases, making the nutrient closer to the composition of the zinc-lithium silicate according to the Li_2O-ZnO-SiO_2 system reported in figure 4.1 (A. R. West, 1980).

Moreover, in all runs, other side-products (but in major amount in A1, A2 and A3 runs) from the solidified solvent were detected (Fig. 4.4), probably grown because, on cooling from 600 °C down to room temperature by quenching (Fig. 4.3), their phase boundary is being crossed (Ito, 1975). Among these phases, the main ones were VO_2, karelianite (V_2O_3), Li_2MoO_4, $Li_2Si_2O_5$, and $ZnMoO_4$ an inorganic chemical compound, which can be used as a corrosion inhibitor in paints and adhesives.

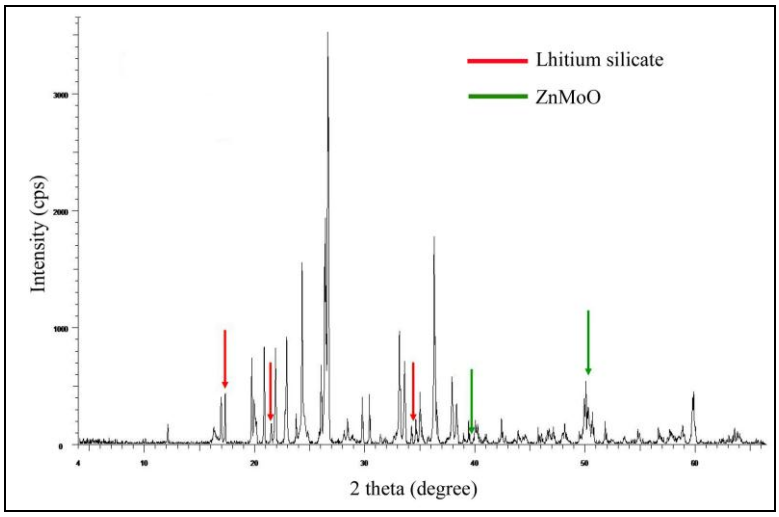

Fig. 4.4. Powder X-Ray diffractogram identifying $Li_2Si_2O_5$, $ZnMoO_4$, crystallized from the solvent.

4.1.2 SEM/EDS characterization

The synthesized Zn-doped enstatite was euhedral and grew in prismatic crystals with well-developed (110), (010), (100), (011), (111), (001) faces.
Enstatite grew as single crystals (Fig.4.5a) and in aggregation (Fig. 4.5b).

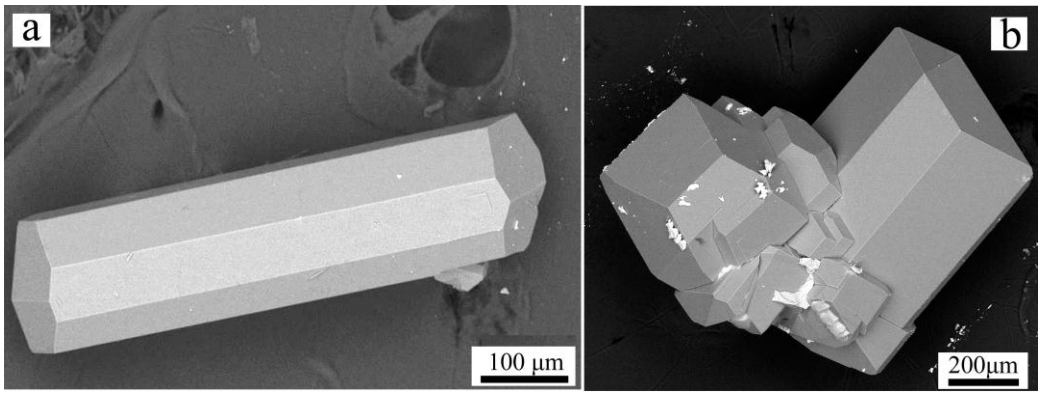

Fig. 4.5. Secondary electron SEM images of a) single crystal of Zn-doped enstatite; b) aggregation of Zn-doped enstatite crystals.

It is shown that at large undercooling values, when the nucleation density is higher and growth rate is lower, a large number of small crystals were produced. Aggregation textures are obtained by the crystallization kinetics at large undercooling values. Indeed, cooling rate faster or equal to 2.1 °C/h gives small aggregation of enstatite (Fig.s 4.6a, 4.6b, 4.6c, 4.6d, 4.6e).
Conversely, when the cooling rate is slower than 2.1 °C/h, crystals grow as single ones (Fig.s 4.7a, 4.7b). Some enstatite crystals show autoepitaxial growth parallel to the c-axis, a kind of epitaxy, in which the oriented growing of crystalline matter takes place on a single-crystal substrate of the same material (Fig.s 4.7b, 4.7d). Occasionally some crystals were twinned. Indeed, sometimes during the crystal growth, or if the crystal is subjected to stress or temperature/pressure conditions different from those under which it originally formed, two or more intergrown crystals are formed in a symmetrical fashion. These symmetrical intergrowths of crystals are called twinned crystals (Mottana, 1988).
The presence of twinned crystals demonstrates that probably part of clinoenstatite could be considered as an inversion product from unquenchable proto-type $MgSiO_3$ single crystals, i.e., "clino-from proto" $MgSiO_3$ (Ozima &Akimoto, 1983).

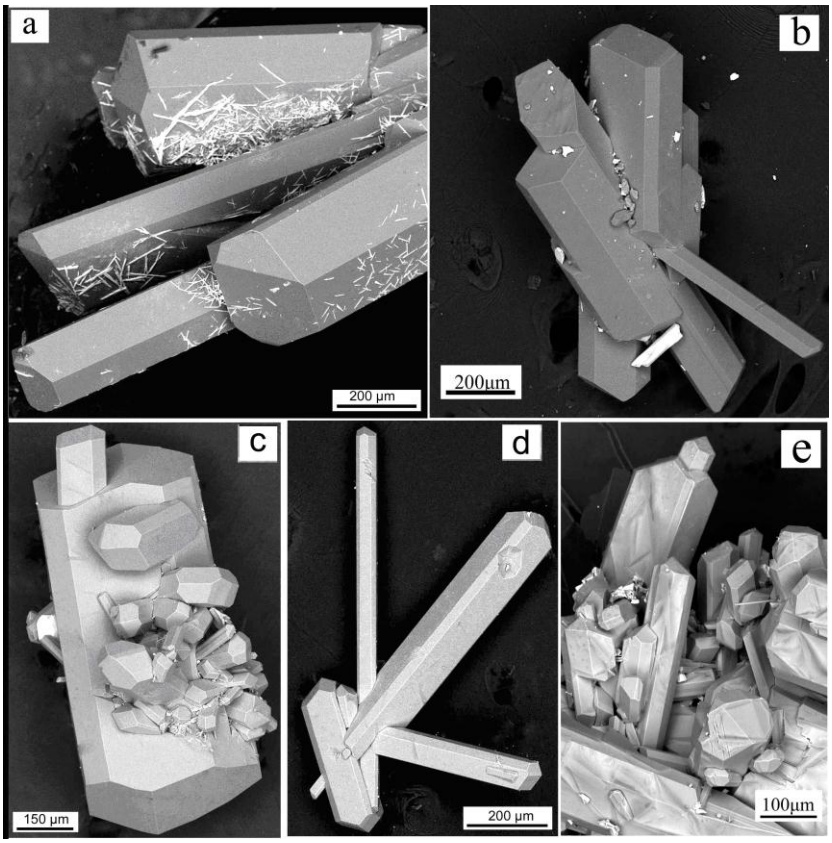

Fig. 4.6. SEM images of various Zn-doped enstatite crystals: a) VO_2 needles over prismatic Zn-doped enstatite crystals (run I1); b) Zn-doped enstatite aggregation crystals (run I1); c-d-e); Intergrowth of Zn-doped enstatite crystals (run A2). Cooling rate 3.7 °C/h (run I1); cooling rate 2.1 °C/h (run A2).

The enstatite crystals length ranges from few μm to 3.5 mm, while the width range from some μm to 500 μm. The size of the crystals depends on how quickly the melt that produced the crystals cooled. Rate of cooling determines the size of the crystal. Slow cooling gives to the crystals time to add more ions and grow larger, while fast cooling causes the ions to immediately lose their motion and combine rapidly, producing numerous nuclei which compete for smaller number of ions. Indeed, on average, the size of Zn-crystals was 1.3 mm in length when the cooling rate was 1.7 °C/h, becoming smaller when the cooling rate was faster (> 2.1 °C/h; run A3, see Table 4.1).

In regard to the chemical composition, EDS-SEM analyses of several enstatite crystals from all runs showed that the amount of Zn^{2+} indicated as ZnO wt% ranges from 3.37 (A1 run) to 10.49 wt% (B2 run; see Table 4.1).

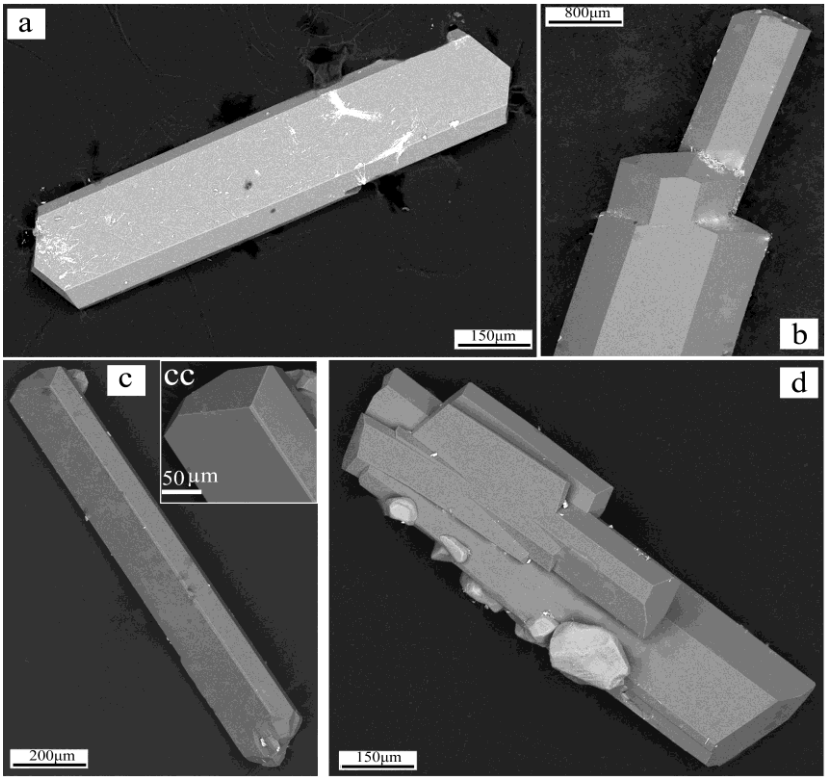

Fig. 4.7. SEM images of various Zn-doped enstatite crystals: a) Zn-doped enstatite single crystal (run C2); b) autoepitaxial growth of Zn-doped enstatite crystals (run C2); c) Zn-doped enstatite single crystal (run B2), cc) magnification of upper side of figure 4.7c; d) autoepitaxial growth of Zn-doped enstatite crystals. Cooling rate 1.7 °C/h (run B2); cooling rate 1.8 °C/h (run C2).

Despite the crystals of the runs A2-C1 and A3-C2 formed from a same starting mixtures (same amount of zinc oxide in the starting mixtures), enstatite from C1 and C2 runs has higher zinc content than enstatite from A2 and A3 runs. Normally, dopant incorporation is kinetically controlled by slow diffusion of it in the growing crystal structure. In this case the slight difference between cooling rate of A1, A2 runs and C1, C2 runs can not explain the change in Zn-content; It is more probable that the higher starting temperature (1250 instead of 950 °C) has a much stronger influence on the Zn-solubility. Moreover, the increase of temperature favored the incorporation of impurities such as dopant within the crystals.

Zn-doped enstatite crystals shift from their stoichiometric composition in the ideal products of the starting mixtures. Indeed, for example in the I1 run, although the starting mixture contains Zn 0.25 and Mg 0.75 in molar proportion, Zn-doped enstatite shows Zn 0.06 and Mg 0.94 atoms per formula unit [$(Mg_{0.94}Zn_{0.06})SiO_3$]. Probably, this is due to the growth of phases that subtract Zn from the starting materials such as Li_2ZnSiO_4 (Table 4.1). Indeed, enstatite crystals in A1, A2, A3 runs, in which Li_2ZnSiO_4 and $ZnMoO_4$ formed in major amount, have the lowest Zn dopant amount (Table 4.1).

Zn-enstatite was produced in big abundance when ZnO was weighed in amount up to 0.60 (mol. proportion) in the starting mixture (B2 run), while it was not obtained at all when the amount of the dopant was more than 0.70 % in mol. ratio.

In some Zn-doped enstatite crystals (A1, A2, A3, I1 runs), vanadium impurities from the flux were detected in small amounts (less than 2 wt %). Incorporation of components in the crystal lattice from flux is may be due to fast cooling (3.7 °C/h and 2.1 °C/h); indeed, impurities are not found (within the limit of detection of EDS/SEM instrument) (B2, C1, C2 runs) when cooling is kept under 2.1 °C/h.

4.1.2.1 SEM/EDS characterization on enstatite thin section

Thin section of several enstatite single crystals were prepared in order to detect the probable presence of defects. Here is reported, as an example, the thin section of one crystal from I1 run. Generally Zn-doped enstatite single crystals appear without inclusions or defects but crystals from I1 run showed some voids (Fig. 4.8).

At present, is uncertain whether such voids are due the lack of nutrient owing the viscosity of the melt (Bloise et al., 2008) or to the relatively fast cooling rate (3.7 °C/h) (Ushio et al., 1991) which causes an addition of the nutrients more rapidly to the edges and corners of a growing crystal than to the centers of crystal faces.

Moreover, in order to study the distribution of the dopant through the crystals, SEM-EDS analyses were conducted on a thin section of the single enstatite crystal (Fig. 4.8).

Analyses conducted in several areas of the sections revealed that the concentration of ZnO was not constant.

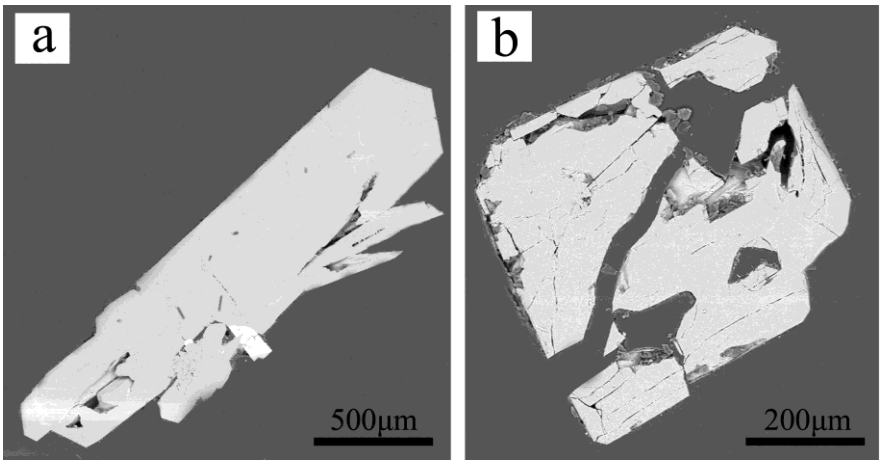

Fig. 4.8 . SEM images of: longitudinal (a) and transversal (b) thin section of a single Zn-doped enstatite crystal.

In the longitudinal section (Fig. 4.8a) the content of zinc ranges from 2.15 to 3.37 wt% from one end to another; the amount of zinc changes from 1.7 in the centre to 2.45 wt% on the edge in the transversal one (Fig. 4.8b). However, the highest difference in the dopant content is between the surface of the crystal (4.4 wt % in average) and the core of it (2.35 wt % in average). Crystals of I1 run seems to be slightly zoned, suggesting crystallization in non-equilibrium conditions. Probably the mechanism for sector formation was controlled by growth rate and crystal does not re-equilibrate by volume diffusion (Schwandt & Mckay, 2006).

4.1.3 XRD characterization

Several single crystals of Zn-doped enstatite with the maximum dopant content $Mg_{0.86}Zn_{0.14}SiO_3$ (run B2; Table 4.1) were selected for X-ray diffraction characterization, in order to understand whether the presence of high amount of zinc dopant incorporated in the resulting enstatite induces or not a significant shift in their cell parameters.

The analyses defined that the most samples crystallize in the orthorhombic crystal system. The cell axes and volume are as follow: a = 18.112(2) Å, b = 8.782(1) Å, c = 5.161(1) Å, V= 821(1) $Å^3$. These parameters were compared with the ones reported by Stephenson et al., (1966) for the pure enstatite. Zn-doped enstatite shows a decrease in the a, b parameters and in volume respect to the non-doped synthetic enstatite (a = 18.225(1) Å, b = 8.815(1) Å and c = 5.175(1) Å, V = 831.3(1) $Å^3$). Specifically, the c axis length remains almost unchanged, while a and b edges show a small change. Likely, the Zn^{2+} ion (i. r. 0.74 Å) substituted for Mg^{2+} (i. r. 0.72 Å) on M1 and M2 sites, induces a slightly distortion and thus, contraction of the whole crystal lattice. Although the orthorhombic structure keeps unchanged, the lattice contraction could imply the instability of the enstatite doped with zinc.

4.1.4 μ-R characterization

Raman spectroscopy can be performed to provide easy and rapid identification among enstatite polymorphs, or to investigate how the structure of enstatite changes when defects are introduced.

Several spectra were recorded from crystals with different amount of Zn-dopant. Here, for simplicity, are reported results obtained from i) the pure enstatite sample (i.e. run H1; Fig. 4.9a); ii) and iii)enstatite with increasing amounts of Zn-dopant (4.3 wt% Fig. 4.9b, 10.42 wt %; Fig. 4.9c).

The shaded areas in all three spectra indicate the spectral regions useful for quick identification of polymorphism. Crystals analyzed belong to the orthorhombic crystal system. Indeed, the strongest vibrational modes and most of the weak ones show frequency values and intensity ratio well consistent with the observations of previous works on orthoenstatite (Choudhury et al., 1998; Reynard et al., 2008). In particular, according to Reynard et al.,(2008), OR-EN and CL-EN can be distinguished easily by the position of the lowest mode at 82 cm^{-1} in OR-EN and 118 cm^{-1} in CL-EN. Besides, the symmetric Si-O-Si bending doublet at 665–687 cm^{-1} in association with the strongest mode at 83 cm^{-1}, are diagnostic of an orthorhombic phases.

While particular care must be taken to distinguish the spectral contribution of the mineral from the other components, when prepared samples, thin sections, and crystals glued to sample holder are analyzed, the Raman technique becomes certainly very useful when applied to a single crystals non-embedded in resins or other materials because all observed bands may be ascribed only to the examined mineral with no interference (as in our case). Indeed, the spectrum obtained from pure single enstatite and the one obtained from the most doped enstatite were easily compared in order to appreciate the probable changes that the dopant can cause on the Raman spectra from this phase (Fig. 4.10).

The Zn doping up to about 10% does not cause any change of the crystal phase, but induces a softening and a broadening of some modes, likewise previously observed for other pyroxenes (Huang et al., 2000; Stalder et al., 2009).

In particular, it is worth to note the remarkable differences of the band-broadening amount among the different modes. At this purpose, for the main peaks, the plot of linewidth value versus increasing Zn concentration has been reported in figure 4.11.

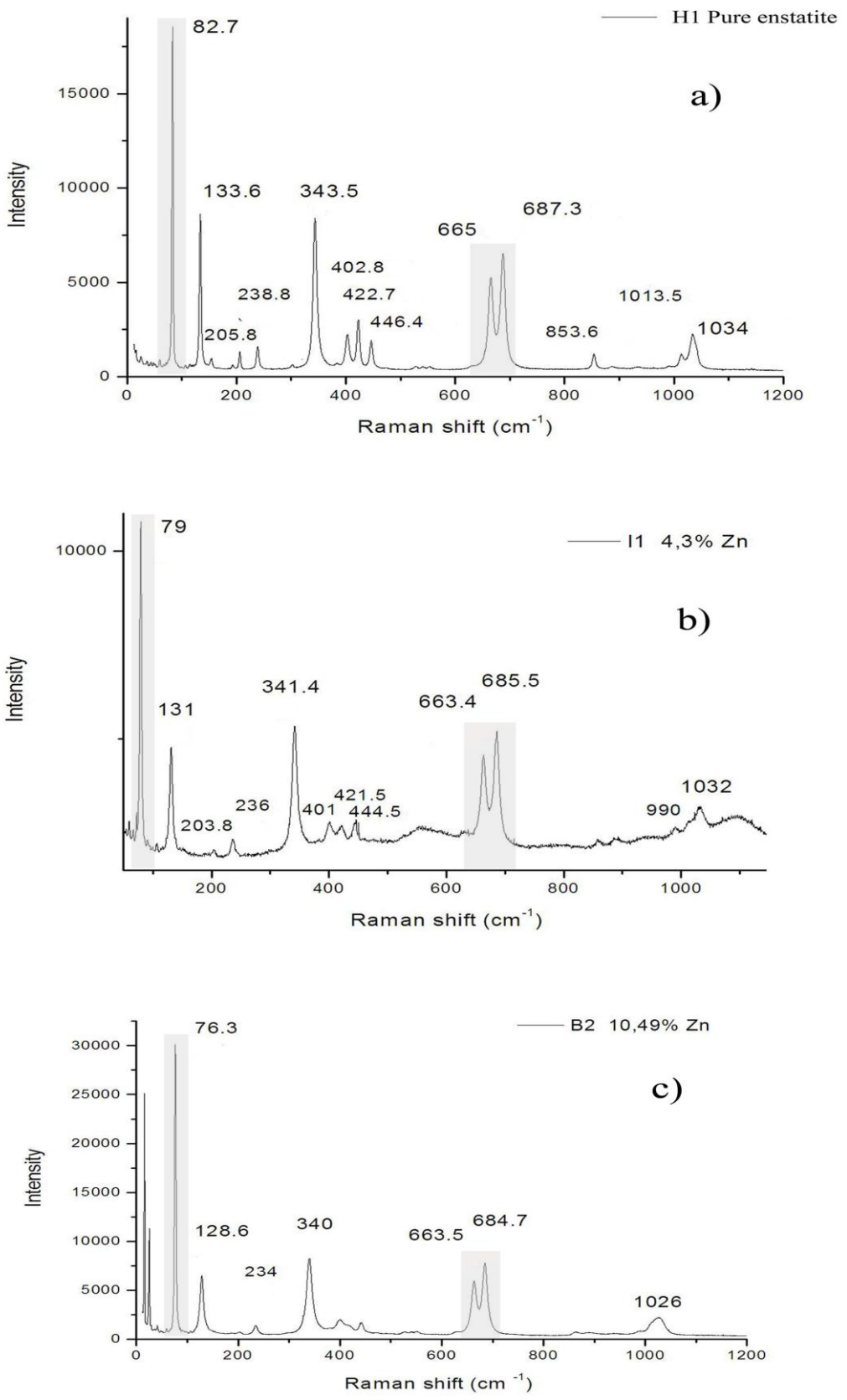

Fig. 4.9 . Raman spectra of: a) no-doped enstatite (run H1); b) Zn-doped enstatite with 4.3 % Zn-content (run I1); c) Zn-doped enstatite with 10.43 % Zn-content (run B2) in the 0 – 1200 cm^{-1} region.

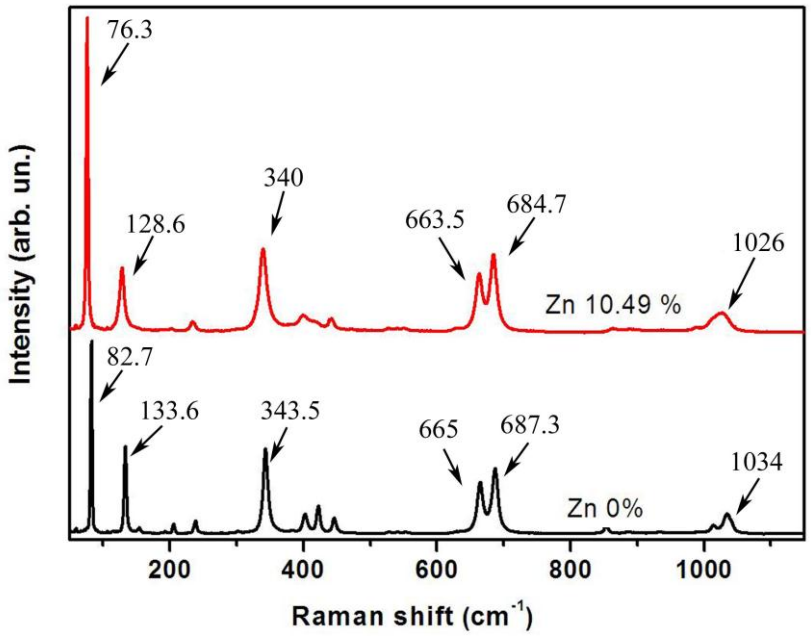

Fig. 4.10. Raman spectra of pure enstatite (run H1) and Zn-doped enstatite (run B2) in the 10 – 1200 cm^{-1} region.

For instance the very strong, lowest frequency mode (82.7 cm^{-1}; non-doped enstatite, run H1) is not influenced very much by the ion disorder: its bandwidth is not increasing vs. Zn concentration for doping greater than the first value of 4.3%, and its maximum broadening is about 20%.

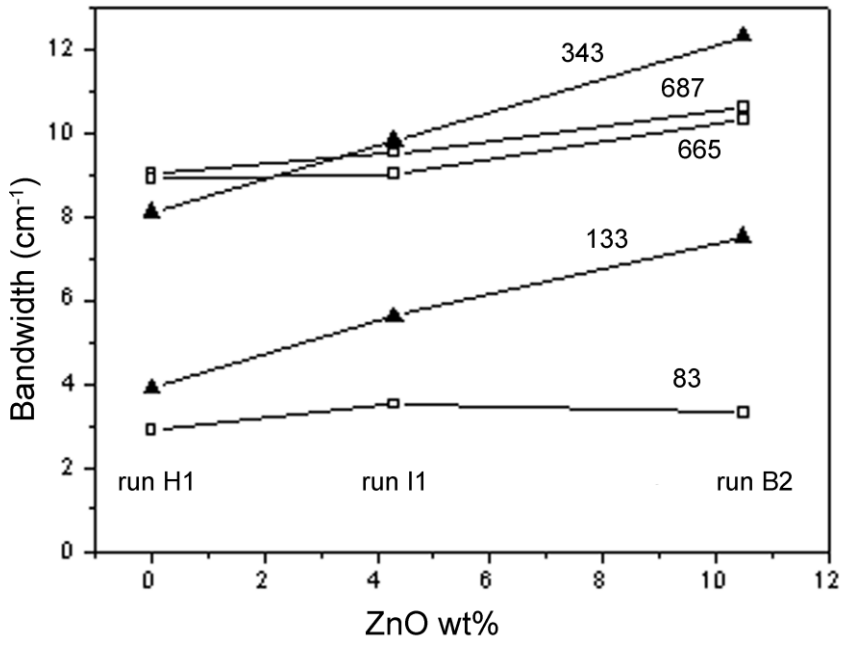

Fig. 4.11. Plot of linewidth value versus increasing ZnO (wt%) concentration; open square: small broadening; solid triagle: great broadening; numbers: frequency in pure enstatite (run H1).

Likewise, the two strong modes at 665 and 687 cm^{-1} have a comparable bandwidth increment, which is less than 20%. In contrast, a very remarkable peak broadening is shown by the mode at 133 cm^{-1} (whose bandwidth turns out to double) and also by the one at 343 cm^{-1} (with more than 50% of increase).

Moreover, weaker Raman active modes close to other modes in the pure compound (run H1) broaden at increasing of the dopant concentration, so that they appear no more resolved, as in the case of the two modes at 403 and 423 cm^{-1} (run H1, Fig. 4.9) and the two high frequency peaks at 1013 and 1034 cm^{-1} (Fig. 4.9). These differences clearly indicate a quite different degree of involvement of the divalent metal ions in the eigenvectors of the Raman active modes mentioned above. In particular, 1) the lowest frequency could be attributed to a silicate group libration; 2) the frequencies that show small broadening could be assigned to the vibrations of silicate groups (i.e., bending modes) and 3) for the two modes at 133 cm^{-1} and 343 cm^{-1} a strong component of metal ion displacement must be postulated.

4.1.5 Side-products

XRPD and SEM/EDS analyses show that, together with enstatite, other phases were also product. Among these, Li_2ZnSiO_4-Zn_2SiO_4 solid solution and quartz, and Li_2MoO_4, $Li_2Si_2O_5$, $ZnMoO_4$, VO_2 from the solidified flux. Figure 4.12 shows two crystals of Li_2ZnSiO_4 with different content of zinc (EDS/SEM detected).

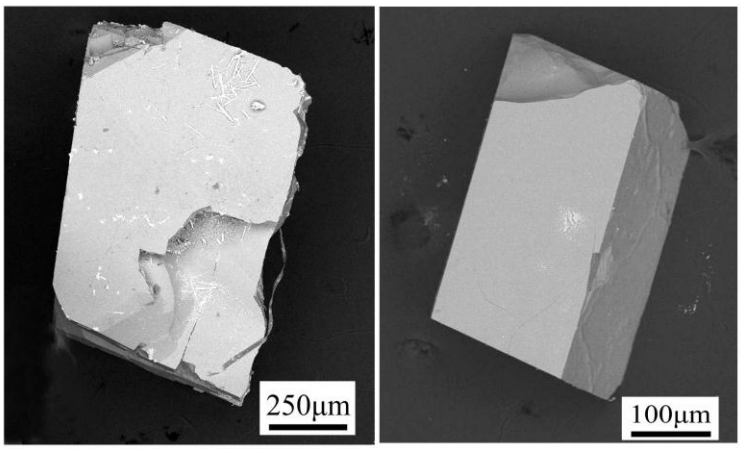

Fig. 4.12. SEM images of: Li_2ZnSiO_4 crystals

Li_2ZnSiO_4 as well as enstatite, can also be considered as one of the most practical and attractive materials that has been widely researched because of its usefulness in many different technological fields. In particular, it is one of the promising ceramic electrolytes, categorized into LISICON (Lithium Super Ionic Conductor) type (Adnan & Mohamed 2012).

Li_2MoO_4 formed hollowed elongated crystals and arrays of thin-walled hexagonal tubes (Fig. 4.13a), VO_2 grew in needles (Fig. 4.13b), $ZnMoO_4$ (widely used as white pigment) exhibited an acicular morphology (Fig. 4.13c).

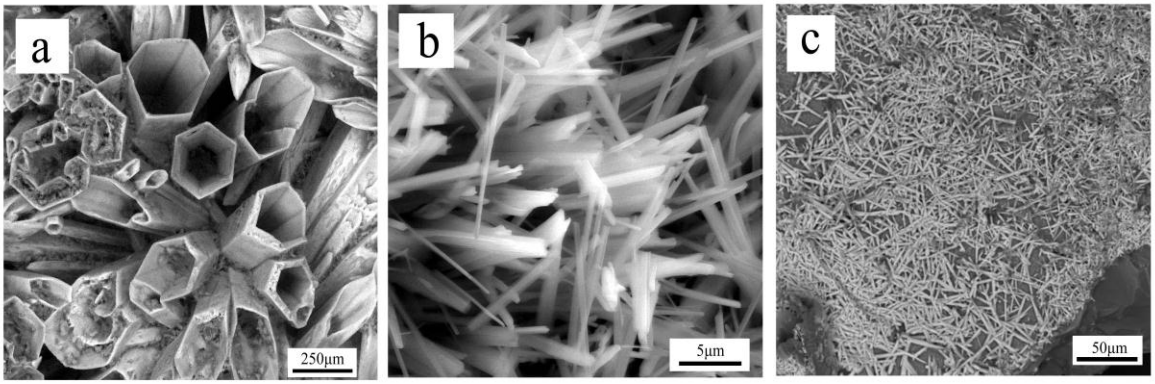

Fig. 4.13. SEM images of: a) hexagonal tubes of Li_2MoO_4; b) VO_2 needles; c) acicular $ZnMoO_4$.

4.2 Enstatite doped with manganese

Optical inspection and X-ray powder diffraction analyses of all products revealed that, in addition to Mn-doped enstatite, other phases were present. In table 4.2 it is reported the minerals obtained for every run, with the average of manganese content, maximum length and average length of Mn-doped enstatite crystals.

Run	Nutrient (molar ratio)			Minerals produced	Average MnO in enstatite (wt. %)	Max length enstatite (mm)	Average length enstatite (mm)
	MgO	SiO_2	MnO				
H1	1.00	1.00	-	Mg-En > Qtz	-	-	0.9
EN1	0.50	1.00	0.50	Mn-En > Qtz	8.87	5.0	2.6
EN2	0.75	1.00	0.25	Mn-En > Qtz,	6.35	8.0	3.8
EN3	0.60	1.00	0.40	Mn-En > Qtz	6.30	7.0	3.4
EN4	0.25	1.00	0.75	H > Qtz > O	-	-	-
EN5	0.00	1.00	1.00	Qtz > H > O	-	-	-
EN6	0.50	1.00	0.50	Mn-En > Qtz	8.56	5.0	3.3
EN7	0.60	1.00	0.40	Mn-En > Qtz	6.28	8.5	4.4
EN8	0.40	1.00	0.60	Mn-En > Qtz	9.89	3.0	1.8
EN9	0.00	1.00	1.00	H >> Qtz	-	-	-

Table 4.2. Molar ratios of starting nutrient mixtures and products obtained. Mg-En = enstatite; Mn-En = Mn-doped enstatite; Qtz = quartz; H = hausmannite (Mn_3O_4); O = Mg-manganese oxide.

Enstatite doped with manganese was yielded in all runs except in EN4 and EN5, which have the content of dopant above 0.70 in molar proportion.

Run products consisted of approximately 70 wt. % enstatite crystals, few side-products and 30 wt. % quenched solute from the fluid, which appeared as grey/reddish, soft material that could easily be removed from the crystal surfaces. Crystals occur mainly as single crystals and only in some case as an aggregation of them. The abundance of Mn-enstatite was more or less the same in all runs. Mn-enstatite crystals are reddish in color and all appear to be idiomorphic, commonly without defects and elongated along the c-axis (Fig.s 4.14a, 4.14b). Inspection of the recovered enstatite crystals revealed that they were virtually free of fluid inclusions. In some rare specimens, veins occurred, which contain some quench material.

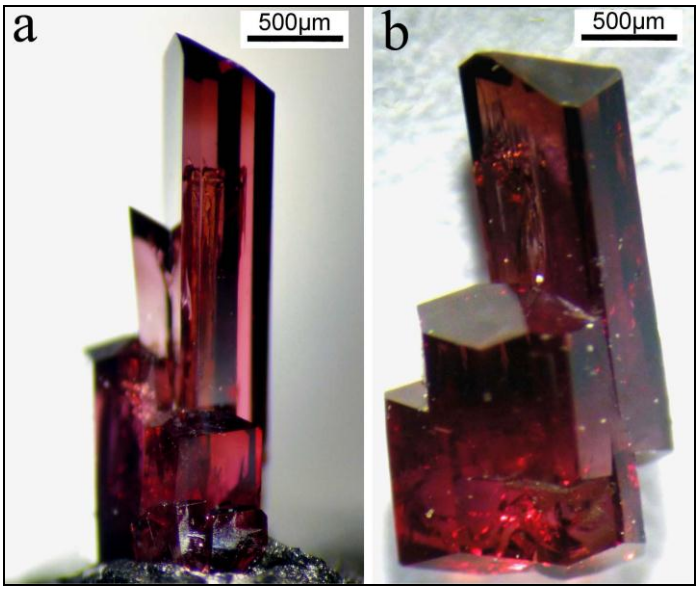

Fig. 4.14. Optical image of reddish crystals of Mn-doped enstatite a) run EN1; b) run EN7.

4.2.1 XRPD characterization

According to the XRPD patterns, the major diffraction peaks of Mn-doped enstatite consisted of orthoenstatite (JCPDS 22-0714) associated with few samples of clinoenstatite (JCPDS 35-0610) (Fig. 4.15).

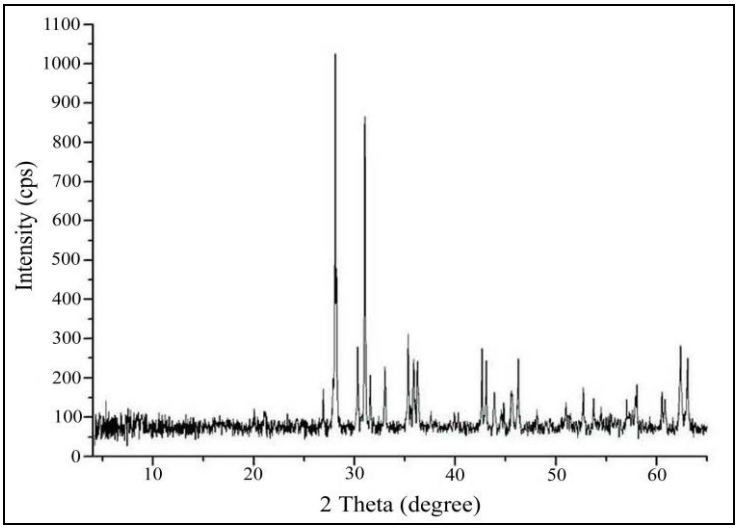

Fig. 4.15. Powder X-ray diffractogram of Mn-doped enstatite (EN1 run).Orthoenstatite (JCPDS Card No.22-0714) and clinoenstatite (JCPDS Card No.35-610) were identified.

As observed in previous experiments, also in this case, it has been difficult to avoid the formation of enstatite of clino-type, regardless of quenching of the products at temperature higher than or equal to 600 °C.

The coexistence of the two polymorphs has been already exstensively explained in paragraph 3.1.1.

Other phases have grown in different quantities; when the MnO (molar ratio) was ≥ 0.75 (run EN4, EN5, EN9), quartz, hausmannite (Mn_3O_4) and Mg-doped manganese oxide were obtained instead of Mn-doped enstatite (Table 4.2). This probably occurred because the bulk composition of the starting mixture is close to the stability field of manganese oxides. Moreover starting materials solubility decreased with increasing contents of basic oxide such as MnO, making the nutrients closer to the composition of other phases (i.e. quartz, hausmannite).

The formation of side-products from the solidified solvent during the cooling was totally avoided and the quench material contained, besides enstatite, significant amounts of amorphous material.

4.2.2 SEM/EDS characterization

As concern morphology, Mn-doped enstatite grew as single prismatic crystals of different size and with well-developed (100), (011), (010), (110), (0-11), (-1-10) and (1-10) faces (Fig. 4.16). Crystals grew often as single one, showing only in some case intergrowths of single crystals parallel to the c-axis (Fig. 4.17c). The largest crystals reached dimensions of more than 8 mm in length.

Normally, crystals grown under slow cooling rate are more than one order of magnitude (by volume) bigger than those crystallized during faster cooling.

In our case, the size of the Mn-doped enstatite seems not to be related to the cooling rate. Indeed, crystals length were of about 8 mm both when the cooling rate was slower (1.7 °C/h; run EN7) (Fig. 4.18b), and when it was faster (3.7 °C/h; run EN2) (Fig.4.16c).

Conversely, an inverse correlation between size and amount of MnO dopant (wt%) has been observed; crystals reduced their size when manganese in substitution for magnesium increased. In particular, when the content of manganese in the starting mixture is higher that 0.50 in molar proportion, the length of the crystals is about 3 mm (EN8 run, Fig. 4.21c) while enstatite reachs length of 8 mm if the amount of manganese is maintained below or equal to 0.40 in molar proportion (EN2, EN7 runs; Fig. s 4.16d, 4.18b).

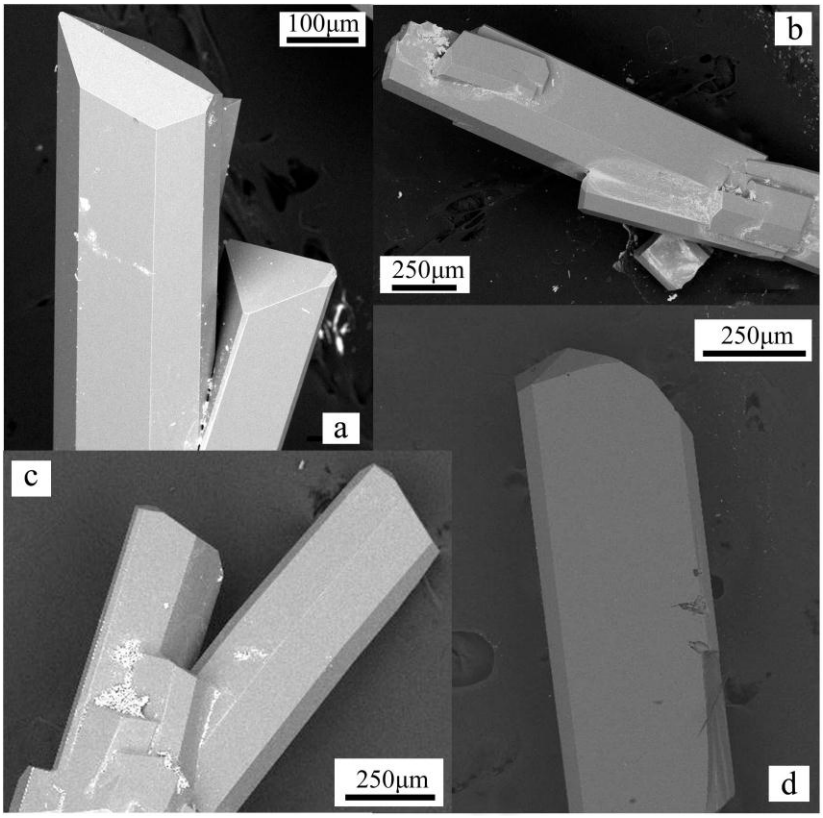

Fig. 4.16. SEM images of various Mn- doped enstatite crystals: a), b) Mn- doped enstatite intergrowth, EN1 run; c) Mn- doped enstatite aggregation, EN2 run; d) Mn- doped enstatite single crystal, EN2 run. EN1 and EN2 runs: cooling rate 3.7 °C/h.

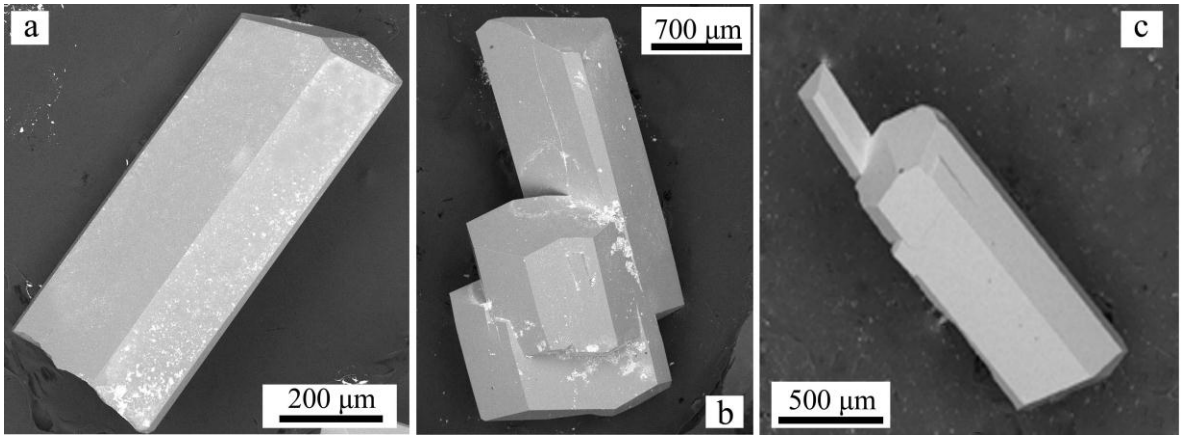

Fig. 4.17. SEM images of various Mn- doped enstatite crystals: a) Mn- doped enstatite single crystals, EN3 run; b) Mn- doped enstatite aggregation, EN3 run; c) intergrowths of single crystals parallel to the c-axis, EN3 run. EN3 run: cooling rate 2.1 °C/h.

Crystals didn't grow always as single crystals. Aggregates are also produced by the crystallization kinetics at large undercooling values. Indeed, fast cooling rate (3.7 °C/h) causes mainly the formation of aggregates of enstatite (Fig. 4.16 a,b,c) and of a few single crystals (Fig. 4.16d). Aggregates of crystals are still present when the cooling rate is

decreased from 3.7 to 2.1 °C/h (Fig. 4.17b) while they are completely absent when the cooling is maintained below 2.1 °C/h (Fig.4.18 a, b, c).

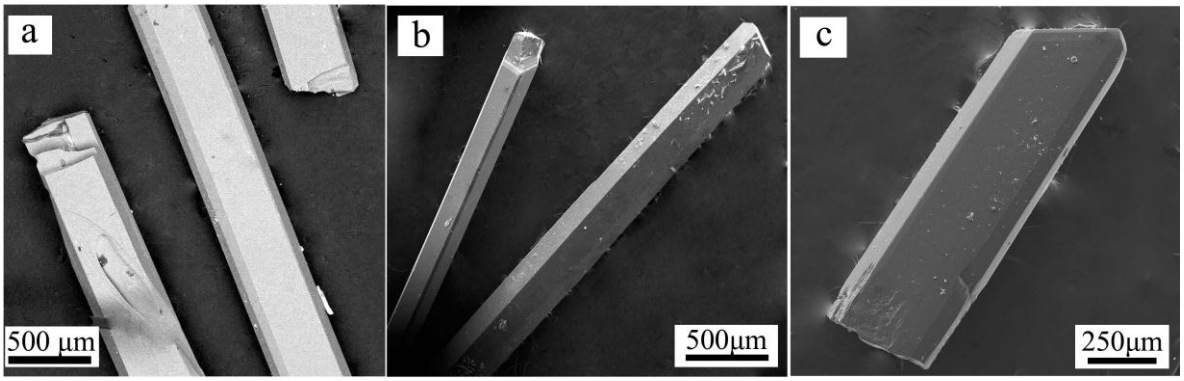

Fig. 4.18. SEM images of various Mn- doped enstatite crystals: a) Mn- doped enstatite single crystals, EN6 run; b) Mn- doped enstatite single crystals, EN7 run; c) single crystal of Mn-doped enstatite, EN8 run. EN6-EN7-EN8 runs: cooling rate 1.7 °C/h.

In regard to the chemical composition, quantitative analyses (EDS/SEM) carried out on 10 single crystals for each run, show that the amount of Mn^{2+} indicated as MnO wt% ranges from 6.28 wt% to 9.89 wt%. Therefore the representative chemical formulae are: $(Mg_{0.9}Mn_{0.1})SiO_3$ – $(Mg_{0.8}Mn_{0.2})SiO_3$. The chemical composition of Mn-doped enstatite was generally close to that of the starting materials, only for those with lower manganese content. However, a direct correlation was observed between MnO concentration in the starting mixture and Mn dopant in the grown enstatite crystals even if the increase was not proportional to the amount of MnO present in the starting mixture (Table 4.2).

Mn-doped enstatite was obtained only from runs in which the content of Mn in substitution for Mg was up to 0.60 in molar proportion. Indeed, when the amount of Mn in the starting mixture was 0.75 (EN4 run), or Mg was totally replaced by Mn as in EN5 run, enstatite growth was inhibited.

Enstatite crystals, within the same run, show a similar content of MnO dopant (slight shift from average value of MnO dopant) when MnO in the starting material was lower (EN2 run); conversely, higher amount of MnO in the starting mixture (run EN8) gave enstatite crystals with different content of MnO dopant, showing an evident shift from average value (Table 4.3). Moreover, EDS/SEM chemical data showed that slow cooling (1.7 °C/h, EN6, EN7) favored the formation of enstatite with similar Mn dopant amount in each crystal compared to those which were obtained from run with faster cooling rate (3.7 °C/h, EN1, EN3; Table 4.3).

Run	MnO (wt %)										Average
	1	2	3	4	5	6	7	8	9	10	
EN2	6.76	6.02	6.37	6.20	6.76	6.27	6.32	6.08	6.90	6.54	6.35
EN8	7.36	8.07	8.45	8.00	11.69	9.98	10.08	14.52	9.26	11.50	9.89
EN7	6.03	6.80	6.41	6.09	6.02	5.93	6.19	6.89	6.50	6.39	6.28
EN1	12.50	7.76	8.71	9.90	6.90	9.40	8.67	8.21	7.88	8.95	8.87

Table 4.3. Representative EDS-SEM analyses of MnO (wt %) in Mn-doped enstatite. EN2 run: lowest content of Mn in the starting mixture; EN8 run: highest content of Mn in the starting mixture; EN7 run: slowest cooling rate (1.7 °C/h); EN1 run: fastest cooling rate (3.7 °C/h).

Lastly, chemical analyses revealed that crystals have not impurities from the solvent in their lattice. Neither vanadium nor molybdenum is incorporated on to the lattice, only some rare specimens has veins in which is contained some quench material.

4.2.2.1 SEM/EDS characterization on enstatite thin section

Thin section of several enstatite single crystals were prepared in order to detect the probable presence of defects. Here is reported, as an example, the thin section of one crystal from EN1 run. The crystal appears well formed (Fig.4.19) only in the transversal section the presence of some voids confirms the probable lack of nutrient owing the viscosity of the melt (Bloise et al., 2008) or to the rapid cooling rate (3.7 °C/h) (Ushio et al., 1991).

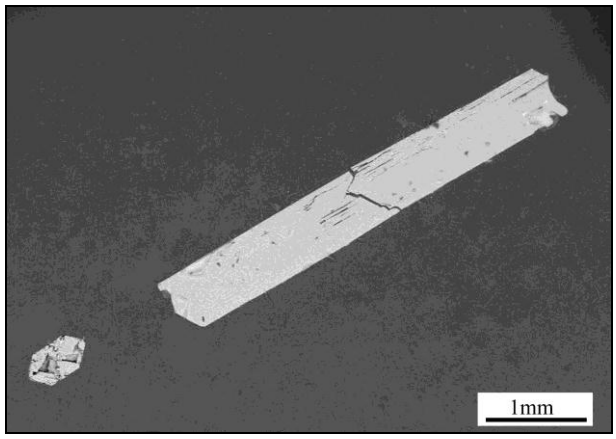

Fig.4.19. Transversal and longitudinal thin section of a single Mn-doped enstatite crystal (EN1 run).

Moreover, in order to study the distribution of the dopant through the crystals, SEM-EDS analyses were conducted on a thin section of the single enstatite crystal (Fig. 4.19).

Analyses conducted in several areas of the sections revealed that the concentration of MnO was not constant. Indeed, the concentration of MnO becomes the highest within the core of the crystal (12.20 wt% in average), while the lowest amount of MnO was recorded on the surface of it (7.55 wt% in average). Mn-doped enstatite crystal (run EN1) results to be zoned, suggesting crystallization in non-equilibrium conditions. Probably the mechanism for sector formation was controlled by growth rate and crystal does not re-equilibrate by volume diffusion (Schwandt &Mckay, 2006).

4.2.3 XRD characterization

Single crystals of Mn-doped enstatite with the maximum dopant content (EN8; see table 4.2) have been chosen in order to be characterized by X-ray diffraction. Refined cell parameters gave different results respect to the pure enstatite, for which the cell parameters reported in literature (Stephenson et al., 1966) are the following: a = 18.225(1) Å, b = 8.815(1) Å and c = 5.175(1) Å, V = 831.3(1) Å^3. Indeed, the analyses defined that the sample belongs to the orthorhombic crystal system with the cell axes a = 18.1278(3), b = 8.7841(3), c = 5.1809(2) Å, and volume V = 824.98(1) Å^3.

The relatively high content of manganese in the resulting enstatite (run EN8; Table 4.2) and greater ionic radius of manganese (0.80 Å) in substitution for magnesium (0.72 Å) in octahedral sites causes structural stress and, therefore, a distortion of the cell with the consequent decrease in volume. For this reason, only a partial substitution of Mg^{2+} by Mn^{2+} can be achieved without big changing in the structure.

4.2.4 μ-R characterization

Raman spectrum of pure enstatite ($MgSiO_3$) single crystal (run H1) was compared with Mn-doped enstatite spectra in order to study the effect of the increasing doping on the position and intensity of Raman bands.

Generally, the intensity of the Raman bands depends on the orientation of the sample with respect to the laser incident beam (polarized); if this orientation is uncontrolled, the relative intensity changes of the Raman bands due to the sample orientation cannot be discriminated from those induced by the different chemical components in the studied phase. At this regards, in order to compare different Raman band intensities spectra were collected after careful alignment of the crystals with respect to the incident laser beam. In

order to verify the crystallographic orientation of the crystals, polarized Raman spectra of pure enstatite were collected at room temperature under parallel XX and crossed XY polarization. The experimental data, obtained under the two different polarizations, are plotted in Fig. 4.20.

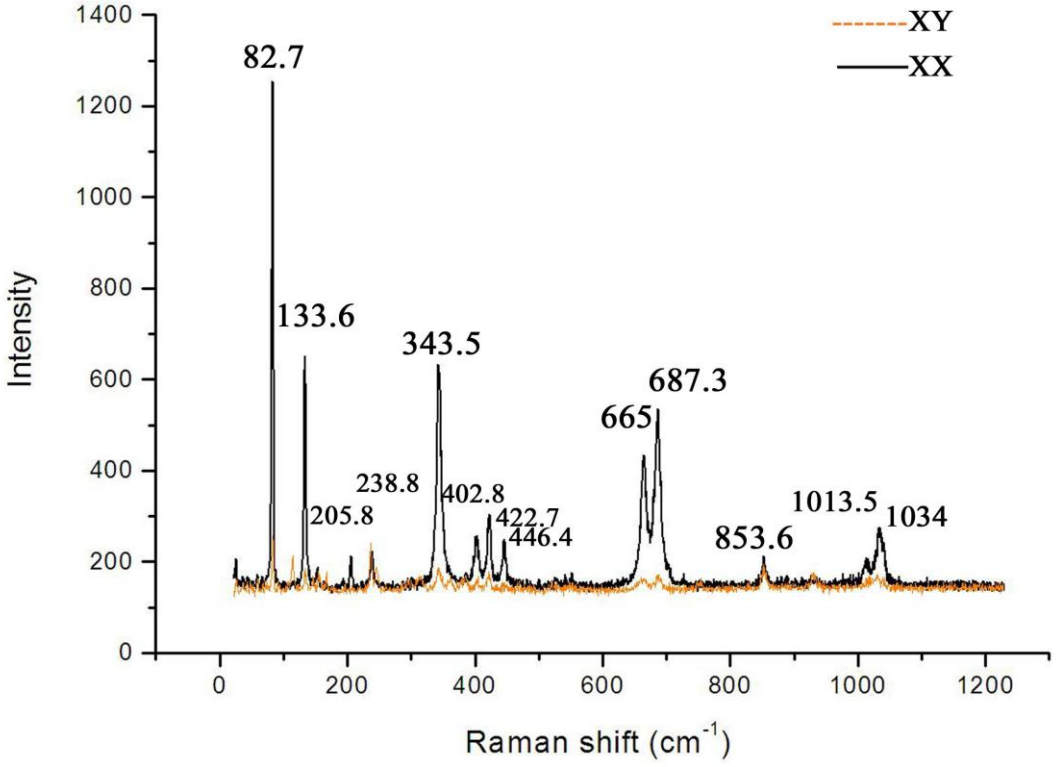

Fig.4.20 . Typical micro-Raman spectra recorded under different polarizations from pure enstatite crystals.

The strong differences in intensity between the two polarizations indicates an amount of spillover smaller the 10%, revealing a good aligment of the crystal with respect to the laboratory axes (directions of beam propagation and polarization) confirming that the Raman spectra used below for samples characterizations can be defined as polarized.

Therefore the intensity changes of the Raman bands in spectra observed from three different enstatite crystals may be considered really doping dependent they have been recorded with the same orientation.

In particular, in figure 4.21 are reported: a) Raman spectrum of pure enstatite; b) Raman spectrum of enstatite doped with 6.30 wt % of Mn; c) Raman spectrum of enstatite with a content of manganese of about 10 in wt %.

The mode at 345 cm^{-1} in pure enstatite strongly decreases in intensity for increasing doping (Fig. 4.21).

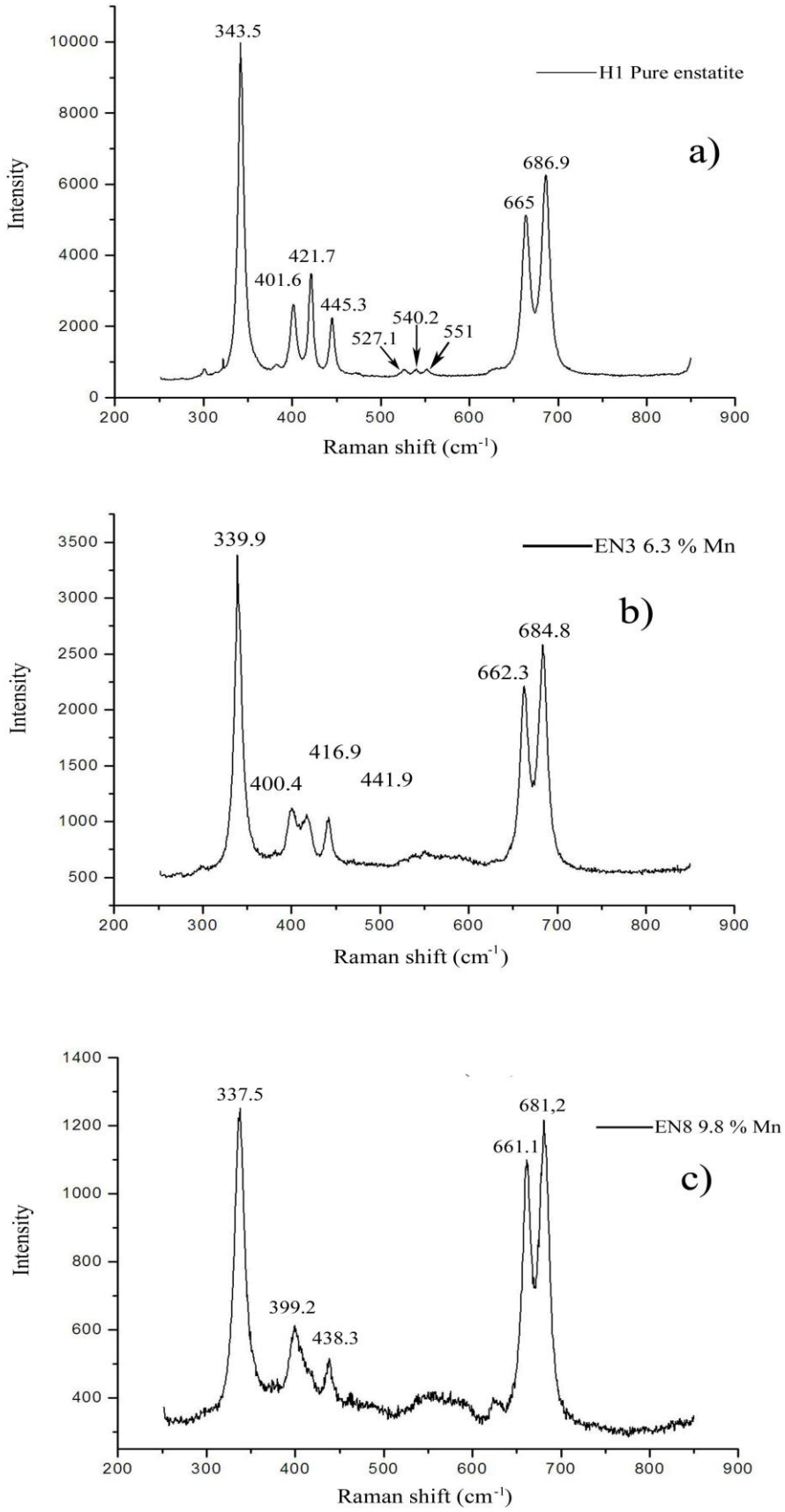

Fig. 4.21 . Raman spectra of: a) no-doped enstatite (run H1); b) Mn-doped enstatite with 6.3 % Zn-content (EN3 run); c) Zn-doped enstatite with 9.8 % Mn-content (EN8 run) in the 200 – 900 cm^{-1} region.

Indeed, when the content of manganese is about 10 wt %, the intensity turns out to be 85 % less respect to that one in the pure enstatite. However, a general decrease in intensity is detected for all main frequencies. This effect is attributed to an increase in surface reflection with the increasing of MnO dopant concentration.

In regard to the number of well observable modes, a significant example of its apparent reduction with increasing of manganese content, is the change in the low frequency (400–450 cm^{-1}) range: from the three modes at 401.6, 421.7 and 445.3 cm^{-1} (pure enstatite) to a doublet at 400-416 cm^{-1} plus a single peak at 441 cm^{-1} (for concentration of manganese of about 6 wt %) or into two single peaks (for Mn-concentration of 10 wt %) with the one at 416 cm^{-1} no more resolved.

Further differences among the three spectra (Fig.4.21) can be observed for the weaker Raman active modes (500–550 cm^{-1}) which broaden with increasing of the dopant concentration, so that they appear no more resolved.

Figure 4.22 reports the three Raman spectra in the 640-710 cm^{-1} range to better demonstrate how an increase in Mn dopant affects raman modes.

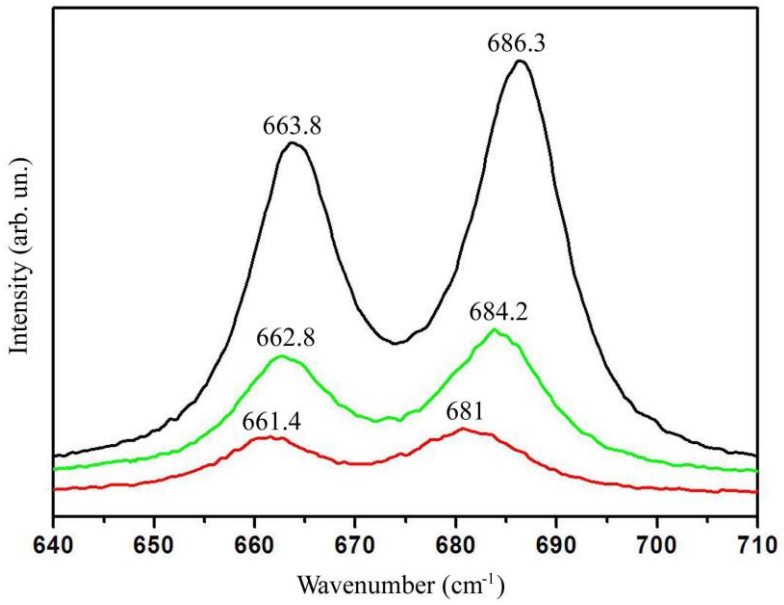

Fig. 4.22 Raman spectra of pure enstatite (run H1) dark line; Mn-doped enstatite (run EN3) green line; Mn-doped enstatite (run EN8) red line, in the 640 – 710 cm^{-1} region.

This range was chosen because in terms of a general application, it is reasonable to compare Raman modes which have 1) high intensity in all orientations, 2) show no overlap

with neighboring bands, (3) are present in the entire solid-solution series analyzed ($MgSiO_3$-$ZnSiO_3$), and 4) show Raman shifts that are dependent on chemical composition. For two different MnO dopant values, 6.30 wt% (run EN3) and 9.89 wt% (run EN8), the following trends in the Raman spectra were observed: i) a down shifting of the peak positions; ii) a widening of the peaks.

These effects indicate changes in vibrational modes because of the increasing presence of MnO. In particular the Raman band at about 686 cm^{-1} which has previously been assigned to the symmetric stretching vibration of the Si–O_b–Si bond (O_b is the bridging oxygen) in $[Si_2O_6]_n$ chains (White, 1975; McMillan & Hofmeister, 1988) in the pure enstatite spectrum, shifts down to 680 cm^{-1} for 9.89 wt% Mn doping (run EN8, Fig. 4.22), in good agreement with the data reported by Stalder et al., (2009) for Fe-doped enstatite.

4.2.5 CL characterization

The luminescence spectra of minerals contain complex information regarding crystal and defect intrinsic structure. There are two kinds of luminescence: 1) intrinsic luminescence which is characteristic of the host lattice. It can be due to non-stoichiometry (vacancies), structural imperfections (poor ordering in the crystal, radiation damage, shock damage, etc.) and impurities (non-activators that distort the lattice); 2) Extrinsic luminescence which results from impurities in the structure. The impurities generate luminescent centers and are most commonly transition elements, rare earth elements and actinide elements (due to the occurrence of valence electrons in either "d" or "f" orbitals). These impurities are generally the most common source of CL in minerals. There are several categories of interactions that influence the character of the CL such as activators ($Cr^{3+,}$ Fe^{3+}, Ti^{4+}, Mn^{2+} and rare earth elements- REEs).

Cathodoluminescence spectra of pure enstatite (H1 run) and Mn-doped one (EN1 run), (Fig. 4.23) were collected in order to have information regarding luminescence characteristics of enstatite when extrinsic defects (activators) are present in its structure.

At room temperature, the CL spectrum of Mn-doped enstatite (run EN1) contains a broad emission located at 677 nm (Fig. 4.23a).

As confirmed by Lin et al. (2006) this broad band is attributed to the transition $^4T_{1g}(G) \rightarrow {}^6A_{1g}$ (S) of Mn^{2+} substitutional to Mg^{2+} position in enstatite; in particular, the

(SiO_4) tetrahedrons form a one-dimensional chain in $MgSiO_3$ host, thus the doping Mn^{2+} ions can easily substitute the Mg^{2+} sites in the matrix material (Lin et al. 2006).

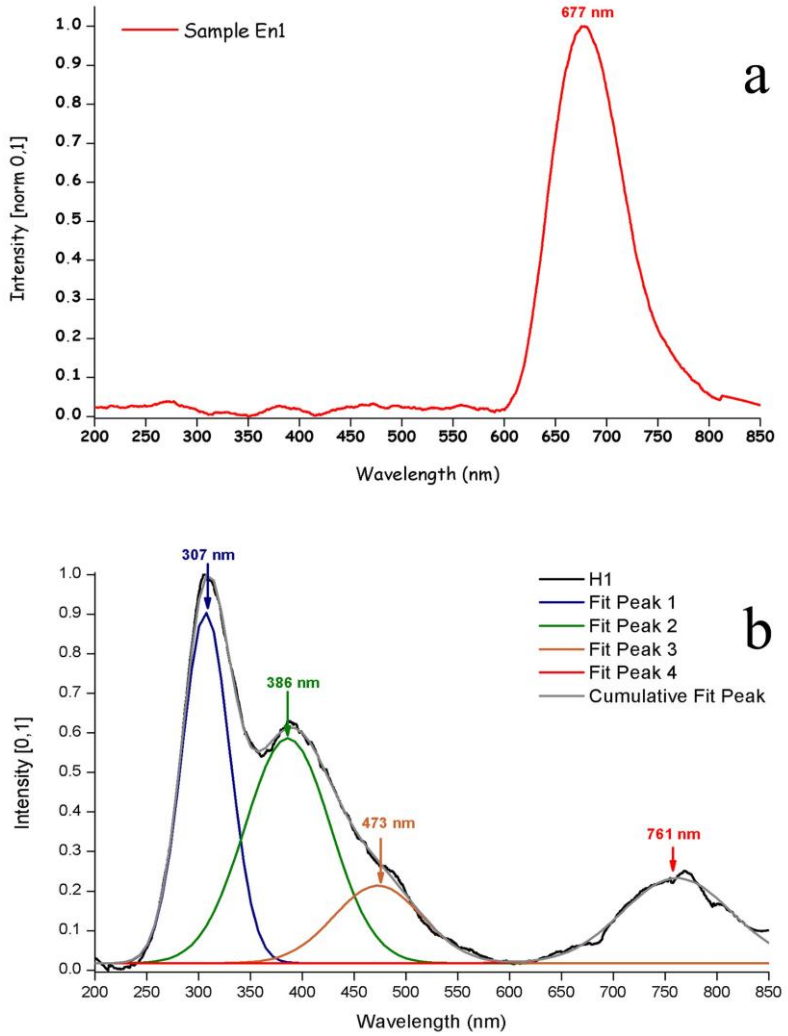

Fig. 4.23. Cathodoluminescence spectra of: (a) Mn-doped enstatite (run EN1); (b) cathodoluminescence spectra of: non-doped enstatite (run H1).

If we compare the CL spectrum of Mn-doped enstatite (Fig. 4.23a) with the analogous spectrum of pure enstatite (Fig. 4.23b), it is shown that the broad emission bands that appear in pure enstatite are completely absent in the CL spectrum of Mn-doped enstatite. This means that in this case the Mn^{2+} CL-signal is much more intense than the mentioned bands in pure enstatite (H1 run).

The electronic transition $^4T_{1g}(G) \rightarrow {}^6A_{1g}(S)$ (responsible for luminescence in Mn^{2+} centers) is spin-forbidden and also Laporte forbidden for electric dipole transitions which accounts for the center of symmetry (Walker et al., 1989). However, the spin-forbiddeness is broken down to some extent by a small degree of spin-orbit coupling, while the Laporte-forbidden

is broken by vibrational coupling of phonons with different parity (G. Walker 1985). For these reasons such transition is characterized by decay time of roughly 10 ms.

The energy of $^4T_{1g}(G) \rightarrow {}^6A_{1g}(S)$ Mn^{2+} transition strongly depends on symmetry and therefore on field strength (Keppler 1992). In fact, according to the Mn^{2+} Tanabe–Sugano diagram, for octahedral coordination (Tanabe & Sugano, 1954), the 677 nm emission is due to the $^4T_{1g}(G) \rightarrow {}^6A_{1g}(S)$ Mn^{2+} transition for a crystal field parameter Δ near 10000 cm^{-1}, and this value is stronger than the Δ value of Mn^{2+} at Mg^{2+} position in dolomite (Walker et al., 1989).

4.2.6 Side-products

XRPD and SEM/EDS analyses show that, together with enstatite, other phases were also product. Quartz (Fig. 4.24a) were detected in all runs while hausmannite ($Mn^{2+}Mn^{3+}{}_2O_4$; Fig 4.24b) grew only in the runs in which the content of manganese in the starting material was above or equal 0.75 in molar proportion (EN4, EN5, EN9 runs) probably because the starting composition was close to the phase boundary of this oxide.

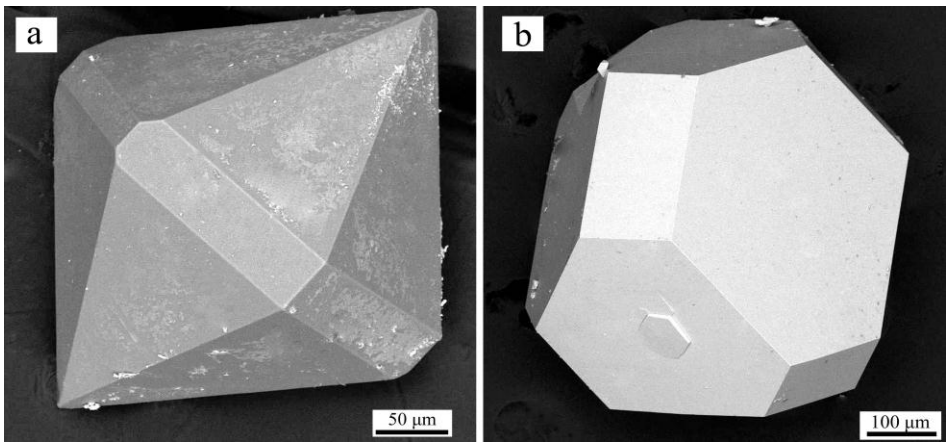

Fig. 4.24 . a) Quartz; b) Hausmannite.

4.3 Talc doped with Zinc

After a rapid quench, the sealed capsules were opened and the products were firstly analysed by optical microscope and X- ray powder diffraction.

In table 4.4 are reported the phases detected for each run in order of decreasing abundance and the content of zinc in talc.

Run	Molar ratio		T (°C)	Reactant	Detected phases	ZnO dopant average (wt.%)
	MgO	ZnO				
T1P	3	0	650	α	Tlc	0.00
T2e	2	1	650	α	Tlc, Qtz, W	7.56
T3f	1.5	1.5	650	α	Tlc, Qtz, W	7.72
T4	0	3	650	α	W, Qtz, Zc	0.00
T2Ca	2	1	650	β	Z, S, C, Tlc	9.06
T3Ca	1.5	1.5	650	β	Z, S, C, Tlc	7.53
T2HCl	2	1	650	γ	Tlc,W, Qtz	8.63
T4HCl	0	3	650	γ	W, Qtz	0.00
T2a	2	1	500	τ	Tlc, Qtz, W	10.68
T2b	2	1	500	α	Tlc, Qtz, W	6.92
T2c	2	1	300	τ	C, Tlc,W	15.16
T2d	2	1	300	α	Qtz, Tlc, W	16.40
TZn1	2	1	650	α	Tlc, Qtz	6.74
T2P	2	1	650	π	Tlc, Qtz	7.05

Table 4.4. Products from each synthesis in order of decreasing abundance, as detected by XRPD and SEM. α= H_2O 12%; β= H_2O + $CaCl_2$ 12%; γ= H_2O + HCl 12%; τ= H2O 4%; π= H2O 16%. Tlc = talc, W = willemite, Q = quartz, S = silicon dioxide, C = cristobalite, Z = zinc oxide, Zc = zincite.

Talc doped with zinc was produced in all runs except in T4 and T4HCl runs in which magnesium was totally substituted by zinc in the starting mixture and TP1 run which is zinc-free.

Under optical microscope, the products appear as a soft, compact, white powder. Only in some runs (T2d run) is possible to distinguish small colourless pieces of quartz. In TZn1 and T2P samples, the presence of fibrous phases is observed at higher magnification. For this reason these two runs (yellow lines in table 4.4) will be discussed separately. Further morphological descriptions will be reported below in SEM/EDS characterization.

4.3.1 XRPD characterization

Diffractograms obtained from each run are grouped according to the temperature in order to stress i) how talc changes in crystallinity with decreasing of growth temperature; ii) the effect of the temperature on the formation of other phases (Fig. 4.25).

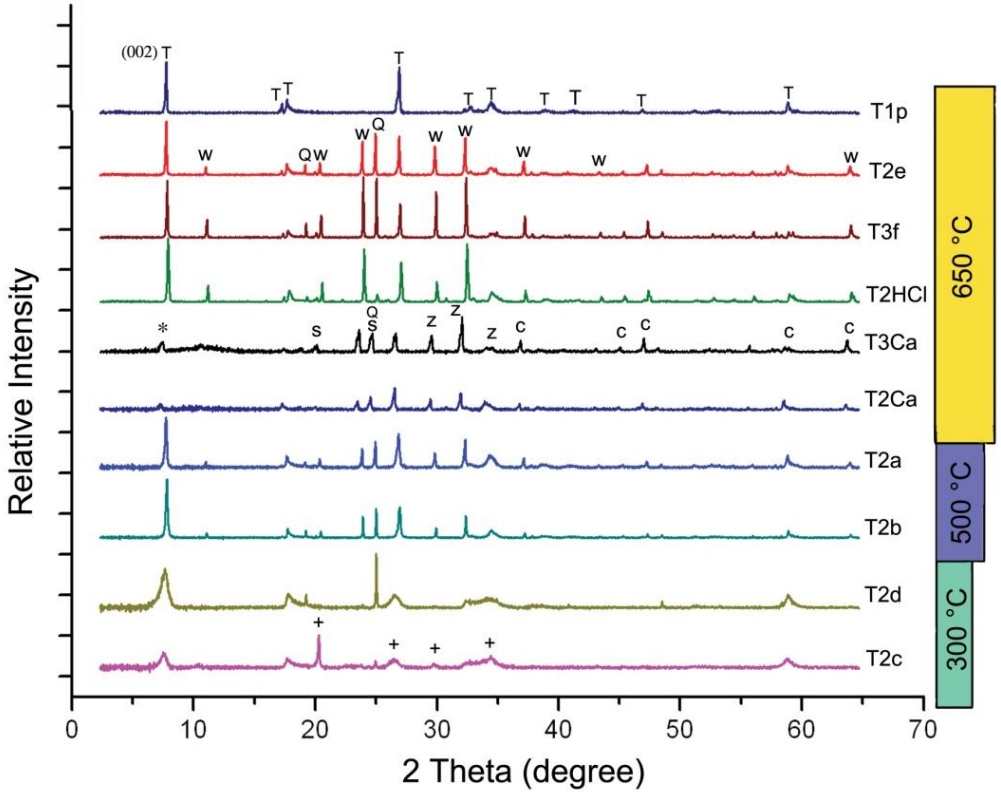

Fig. 4.25 . XRPD patterns of runs; identified phases are indicated with capital letters, asterisk and plus symbols. T = talc (JCPDS 13-0558); * = Talc (JCPDS 10-0403); W = willemite (JCPDS 46-1316); Q = quartz (JCPDS 46-1045); S = silicon dioxide (JCPDS 29-0085; 11-0252); C = cristobalite (JCPDS 3-0267); $^{+}$ = cristobalite (JCPDS 39-1425), Z = zinc oxide (JCPDS 21-1486).

Results show that non-doped talc (JCPDS 13-0558) as single phase was obtained after 160 h of reaction, at 650 °C and 2 kbar. Willemite (Zn_2SiO_4; JCPDS 46-1316) and quartz (JCPDS 46-1045) were also detected together with the talc when ZnO was added to the starting mixture. A decrease in temperature from 650 °C (T2e) to 500 °C (T2a) yielded the same phases: talc, willemite and quartz; a further decrease to 300 °C causes a reduction in talc crystallinity. Indeed, the temperature of hydrothermal synthesis influenced considerably the crystallinity of the materials since the biggest peaks intensity and the reduction of the full width at half height with the increase of the synthesis temperature

proved the best crystallinity. This fact was clearly illustrated by the intensity and the shape of (002) reflection at 9.471 (2θ); indeed the powder diffraction patterns presented a broad peak for low hydrothermal synthesis temperatures (T2d, T2c runs) whereas T1p, T2e and T3f samples exhibited a sharp peak.

Likely, a decrease in temperature in a neutral pH environment causes low SiO_2 solubility. The interaction between cristobalite and other starting materials is therefore inhibited. Moreover, when magnesium was totally substituted by zinc in the starting mixture (i. e., T4 run, not shown in Fig. 4.25), willemite, quartz and zincite (JCPDS 1-1136) were obtained instead of talc (Table 4.4). Generally, crystals of a particular phase are usually produced from a solution in a state of supersaturation relative to that phase. To form good quality crystals the degree of supersaturation must be minimised. In this case, the supersaturation minimization was too high, moving the system toward the equilibrium field of other minerals such as willemite.

Zn-doped talc (JCPDS 10-0403) reduced its abundance and crystallinity not only when the growth temperature was below 500 °C but also when H_2O + $CaCl_2$ was used as reactant (runs T2Ca, T3Ca). Likely, $CaCl_2$ does not favor the reaction between the starting oxide mixture that mainly form zinc oxide (JCPDS 21-1486) and silicon dioxide (JCPDS 29-0085) in addition to low crystalline talc. Conversely, the use of HCl as reactant (talc grows in acidic pH environment) increased the solubility of SiO_2, (as showed in figure 4.25, from the decrease of the main quartz reflection at 26.617 (2θ)), improving the reaction toward a more abundant formation of talc.

XRPD data show that on equal experimental terms (T2a and T2b, 500 °C; T2c and T2d, 300 °C), Zn-doped talc obtained from runs altered with 12 wt% distilled water (T2b, T2d runs) is more abundant than that one obtained from runs with 4 wt% distilled water (T2a, T2c runs).

4.3.2 SEM/EDS characterization

The SEM micrographs of talc, synthesized in hydrothermal conditions at different temperatures and with different types of reactant, are shown in figures 4.26 and 4.27.

The low crystalline talc obtained at 300 °C (T2c, T2d runs; Fig. 4.26a, 4.26b) shows different morphology from that obtained at 650 °C. When the temperature of hydrothermal processing is at or below 500 °C, talc produced has a cabbage-like morphology; if the

temperature is raised to 650 °C, talc formed, assumed its classical hexagonal tabular morphology (T3f and runs T2e; Fig.4.27a, 4.27b).

In particular, figure 4.26 shows how crystallinity of T2c, T2d, T2a, T2b samples depends mainly on the amount of reaction water in the starting mixture (from 4 % to 12 %); crystallinity seems to decrease with decreasing of water content.

In regard to the lamellar talc, the diameter ranged from a few μm (T2e run) to 30-40 μm (T3f run, Fig. 4.27a, 4.27b) while talc with a cabbage-like morphology is smaller in size (few microns).

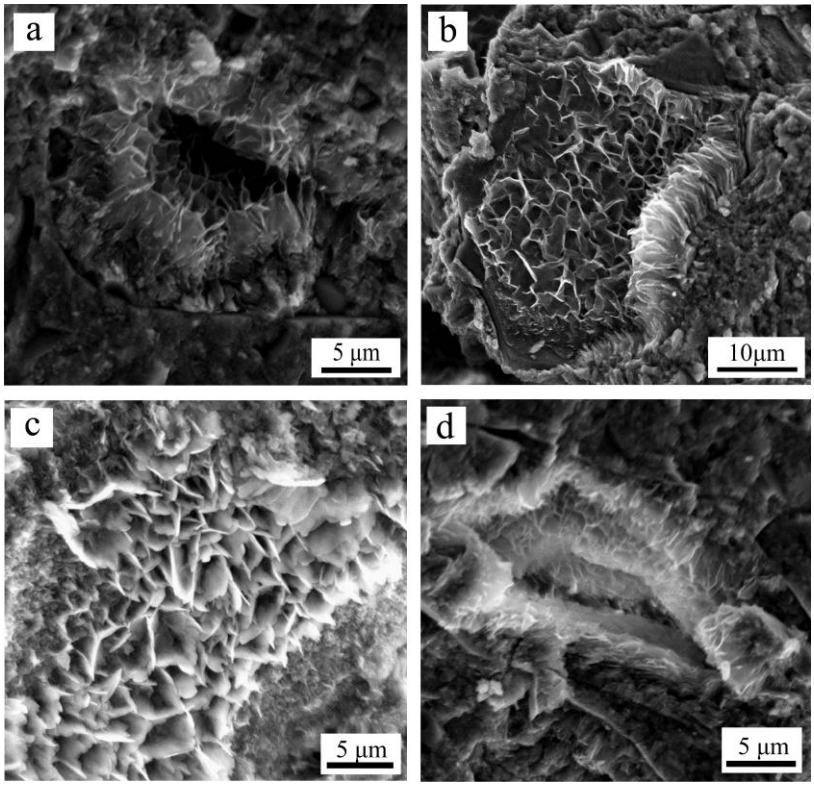

Fig. 4.26. SEM images of talc showing cabbage-like morphology; a) T2c run; b) T2d run; c) T2b run; d) T2a run. T2c and T2a = water content 4%; T2d and T2b= water content 12%.

Under unchanged experimental conditions (i.e. temperature and molar ratio), but in an acidic pH environment (using γ= H_2O + HCl 12% reactant), talc lamellae turn out to be better crystallized and increased in size from about 2 μm (T2e run) to 8 μm (T2HCl run; Fig. 4.27d).

On the contrary, when starting mixture were treated with β= H_2O + $CaCl_2$ 12% reactant, talc particles appear to grow poor crystallized and in less abundance (Fig.4.27c)

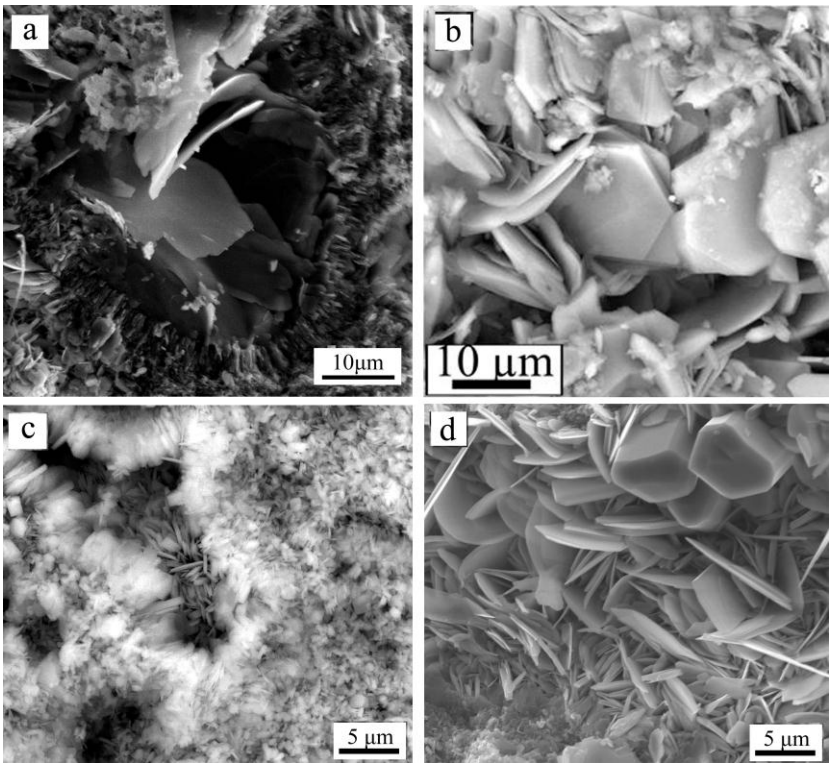

Fig. 4.27 . SEM images of various run products: a) lamellar talc, T3f run; b) talc showing classical exagonal plate morphology, T2e run; c) poor crystallized talc, T2Ca run; d) talc plate and willemite, T2HCl run.

As regards chemical composition, EDS-SEM semi-quantitative analyses of several talc crystals from all runs showed that the amount of Zn indicated as ZnO wt% ranges from 5.40 to 19.35 wt% (Table 4.5).

Run	ZnO (wt %)										Average
	1	2	3	4	5	6	7	8	9	10	
T2e	6.60	8.87	9.27	7.30	6.59	9.38	7.59	7.68	6.34	6.00	7.56
T3f	6.64	7.93	7.29	8.79	7.88	8.12	7.34	7.00	7.47	8.74	7.72
T2Ca	7.84	6.84	12.70	14.07	13.05	11.19	5.89	6.80	6.72	5.50	9.06
T3Ca	7.58	7.47	10.83	13.75	10.77	8.38	7.44	9.11	9.60	7.44	7.53
T2HCl	9.01	10.14	9.01	8.11	8.93	7.32	9.00	7.00	6.11	11.64	8.63
T2a	13.04	10.23	7.14	10.46	10.27	10.58	10.69	13.22	11.18	9.94	10.68
T2b	7.58	6.74	6.71	7.20	7.23	5.40	7.26	6.96	6.83	7.24	6.92
T2c	18.11	13.47	16.43	9.67	12.20	18.83	15.14	17.88	14.18	15.68	15.16
T2d	17.49	19.35	14.83	16.01	16.06	15.59	15.91	16.69	15.85	16.17	16.40

Table 4.5. Representative EDS-SEM analyses of ZnO (wt %) in Zn-doped talc synthesized from all run.

The concentration of ZnO in talc appears to be no-constant within the crystal suggesting crystallization in non-equilibrium condition. Moreover, Zn-doped talc crystals shifted from

their stoichiometric composition, in the ideal products of the starting mixtures, for the following reasons: i) growth of other phases (Table 4.4); ii) presence of small amounts of not reactive starting materials in all runs, suggesting that reactions were incomplete. Zn-doped talc did not form (run T4, T4HCl) when Mg was totally substituted by Zn in the starting mixture. $Zn_3Si_4O_{10}(OH)_2$ is not a stable phase at these synthesis conditions. An increase in temperature led to a decrease in the Zn content in the talc. Indeed, Zn-content in run T2d (300 °C) was double with respect to the amount present in run T2e (650 °C).
Likely, the content of Zn-dopant in talc crystals is limited because the synthesis conditions (i.e., higher temperature) favoured the growth of a big amount of anhydrous phases as willemite (Zn_2SiO_4) instead of talc and, thus zinc was subtracted from the mixture.

4.3.3 TG-DSC characterisation

Thermal decomposition by thermogravimetric analysis of natural talc has been extensively studied (Wesolowski, 1984). DSC curves of talc samples collected in different parts of the world have shown slight fluctuations which may be due to a combination of the dissimilarities in the particle size (Balek et al., 2008), differences in crystallinity, kinds of isomorphically substituted ions and presence of mineral impurities (Wesolowski, 1984).
In regard to the thermal stability of silicates in general, it is well known (Wesolowski, 1984) that it increase with increasing symmetry of the bonding and with ionic density in the octahedron. It attains a maximum when the central cation is surrounded by six oxygen anions. This is due to the fact that the value of the coordination number is a function of the radius of cation and of the deformation of the oxygen anions. As an example, when in silicates Mg cation is replaced by a cation with similar or equal ionic radius, thermal stability of minerals does not change. Conversely, the stability decreases when the cation that replaces magnesium has greater ionic radius.
Here, results of TG and DSC are presented in order to characterize the thermal behaviour of talc with increasing of zinc in its lattice.
Results of DSC for the pure and Zn-doped talc samples are investigated in the temperature range of 20 - 1000 °C and shown in figure 4.28 and table 4.6.

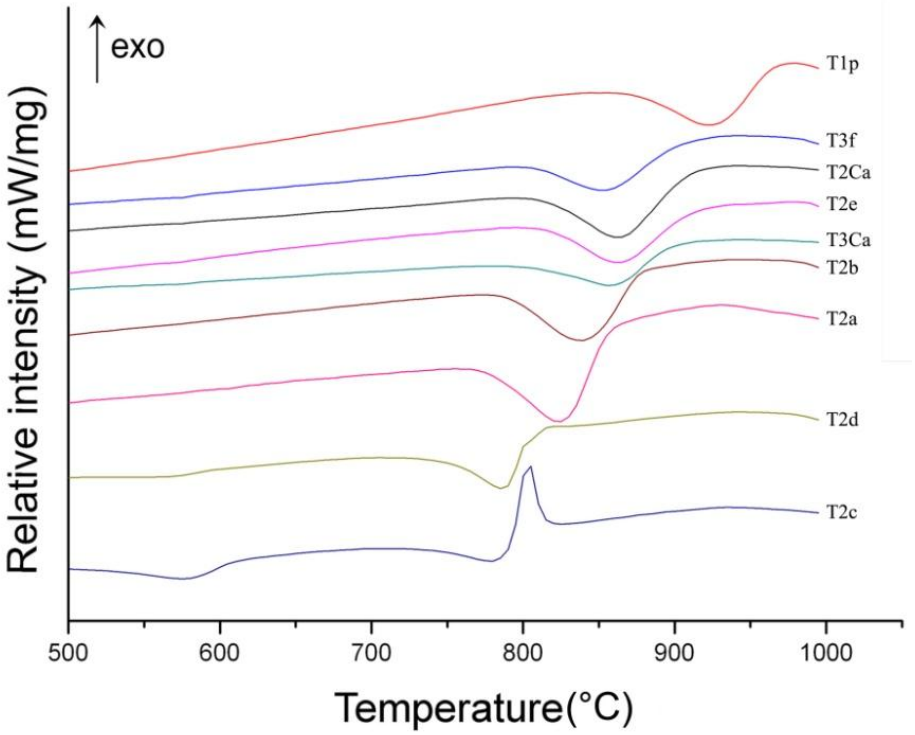

Fig. 4.28. DSC curves of synthetic non-doped talc (run T1p) and Zn-doped talc in the range of 500 – 1000 °C (run T3f, T2Ca, T2e, T3Ca, T2b, T2a, T2d, T2c).

During the heating of the talc, water is liberated in distinct steps due to differences in its bonding energy. In agreement with Avgustinik and Vigdergauz, (1948), it is observed the presence of three stages of talc dehydration: between 20–140 °C, 140–560 °C and the main one in the range of 599.85 – 950 °C.

Run	ZnO dopant (wt.%)	DSC endo (°C)	TG loss (%)
T1P	0.00	923.6	4.43
T2e	7.56	863.6	3.38
T3f	7.72	852.6	2.16
T4	0.00	-	-
T2Ca	9.06	862.6	3.42
T3Ca	7.53	856.9	2.25
T2HCl	8.63	-	-
T4HCl	0.00	-	-
T2a	10.68	825.1	3.62
T2b	6.92	838.1	3.65
T2c	15.16	778.9	3.18
T2d	16.40	786.1	3.84

Table. 4.6 . Results of DSC and TG of talc sample in the range 599-1000 °C).

The first two stages were due to the loss of physisorbed water. The values of the first and second mass losses decreased when the hydrothermal synthesis temperature increased.
During the third stage of dehydration, 3,32 wt% (on average) total nonhygroscopic water is liberated from the Zn-doped talc, while 4.43 wt% water content is liberated from the non-doped talc. Figure 4.29 reports the mass losses for each run in the range 599.85 – 950 °C, reassumed in table 4.6.

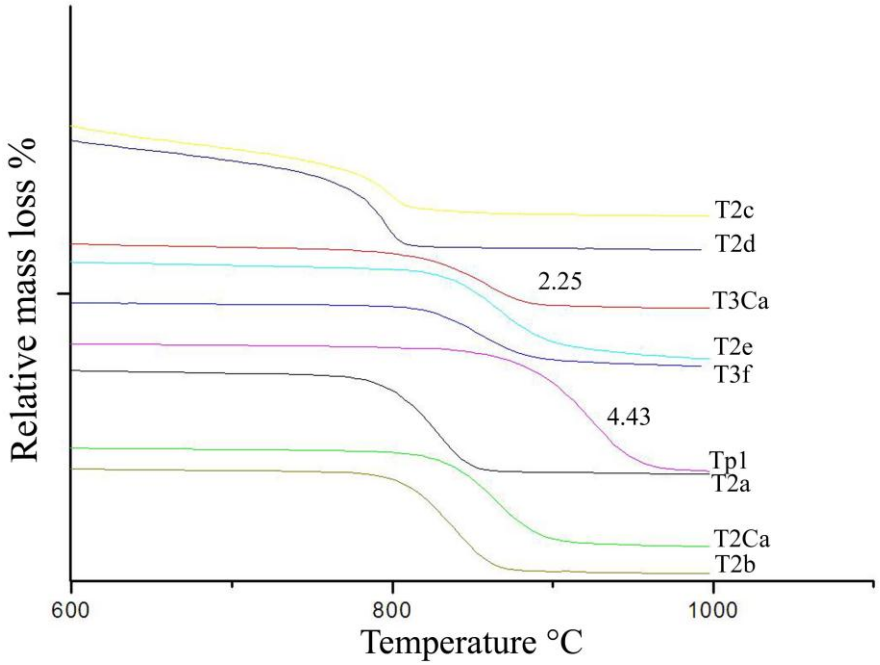

Fig. 4.29. Results of TG of talc samples in the range of 600-1200 °C.

The third loss, corresponding to the endothermic peak between 786 and 923 °C, was assigned to the dehydroxylation of the phyllosilicate sheets. This step is followed by the collapse of the sheet structure.
In particular, pure talc shows a breakdown at 923.6 °C, whereas Zn-doped talc collapse at temperature that decreases with increasing of Zn-dopant content.
The lower temperature value (down to 786.1 °C; T2d run; Table 4.4) observed for decomposition of Zn-doped sample indicates the lower thermal stability of the Zn-doped talc with respect to the pure talc.
It is clear that the presence of zinc in talc lattice which has the ionic radius (0.74 Å) slightly larger than ionic radius of Mg (0.72 Å) causes defects in the Zn-doped talc that decreases its thermal stability.

The dehydroxylation of non-doped and Zn-doped talc is accompanied by the decomposition of talc into free magnesium oxide, free zinc oxide and silica (XRPD verified). Only in T2c sample, the exothermal peak at 820 °C (Fig. 4.28) is relative to the formation of enstatite (XRPD identified). Indeed, the decomposition of talc in this sample is accompanied by the simultaneous formation of enstatite and amorphous silica. It is probable to suppose that the formation of enstatite only in T2c sample at this temperature was due to 1) the smaller size of talc crystals; 2) the lower crystallinity of the T2c sample with respect to the other samples.

4.3.4 FT-IR characterisation

The following investigation was undertaken mainly to study the detailed effects of substitutions in the octahedral layer on the hydroxyl stretching vibrations of talc.
At this purpose, non-doped talc (run T1p) was compared with Zn-doped talc (run T2d) by FT-IR in the 400-1300 and 3600-3720 cm^{-1} frequency ranges (Fig. 4.30). The spectrum of non-doped talc (run T1p) was very similar to that reported in previous work (Farmer, 1958), although the band around 1000 cm^{-1} moved to a lower frequency of 984 cm^{-1} (Fig. 4.30a). The possible vibrational band assignments are as follow; the bands in the region of 900-1100 cm^{-1} were identified as Si-O stretching motions with tetrahedral SiO_4 groups, and those in the 600-700 cm^{-1} region as OH librations, accompanied by weak Si-O bending vibrations (Russell et al., 1970; Martin et al., 1999). The bands at 506 and 540 cm^{-1} were interpreted as Mg-OH vibration (Martin, 1999) and the two bands at 459 cm^{-1} and 417 cm^{-1} were assigned to Si-O bending (Wilkins, 1967). In Zn-doped talc (run T2d), bands at 984 and 665 cm^{-1} shifted to the slightly lower frequency and a weak band at 796 cm^{-1} split into two peaks at 780 and 798 cm^{-1} (Fig. 4.30a). These bands are ascribed to the vibration of OH groups correlated with the octahedral cation. According to Martin et al., 1999, the location of this band (i. e., 796 cm^{-1}) is influenced by the nature of the octahedral cation (presence of zinc in this case). Finally, the bands at 506 cm^{-1}, 540 cm^{-1} and 459 cm^{-1} that were present in the non-doped talc (run T1p), are not more resolved in the Zn-doped talc (run T2d). In addition, the presence of the band at about 540 cm^{-1} only in talc obtained at 650 °C confirms that the temperature had a significant effect on the environment of the Mg–OH group.

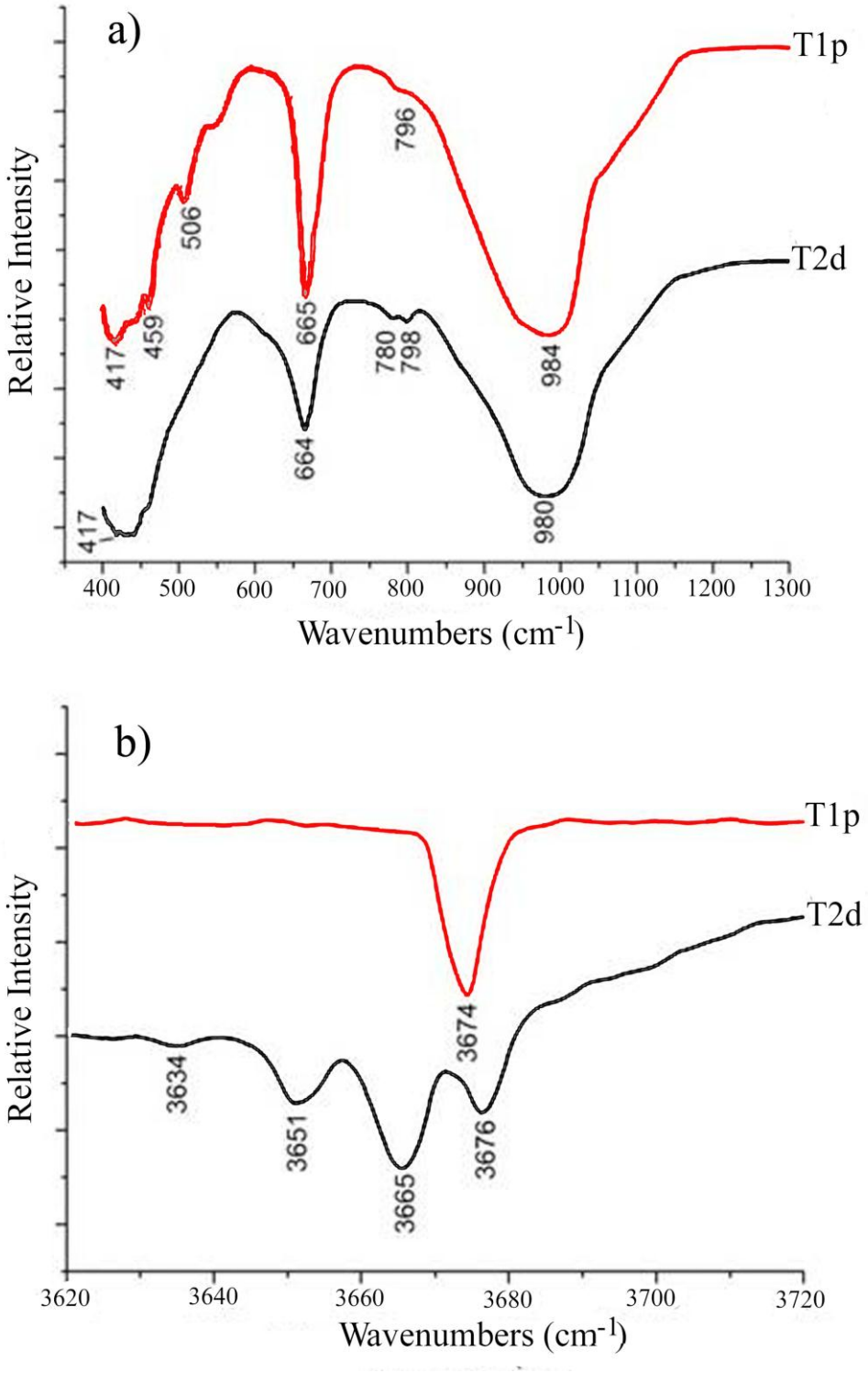

Fig. 4.30. a) Infrared spectra of non-doped talc (run T1p) and Zn-doped talc (run T2d) in the 350 -1300 cm^{-1} region; **b)** infrared spectra of non-doped talc (run T1p) and Zn-doped talc (run T2d) in the OH stretching region (3620 - 3720 cm^{-1}).

Summarising, all bands in the Zn-doped talc spectrum become slightly broader; the strongest ones develop low frequency tails; bands shift to lower frequencies.

Variations in peak frequency, like those in bandwidth, are related both to ionic radius and the extent of substitution of the zinc replacing magnesium in the octahedral layer.

The hydroxyl stretching vibrations of the Zn-doped talc in the region from 3620 to 3720 cm^{-1} furnished further valuable information on the grouping of cations around the hydroxyl group.

The hydroxyl stretching fundamental peak of non-doped talc (Fig. 4.30b) at 3674 cm^{-1} for ν(O–H) in Mg_3OH group (Chabrol et al., 2010), splits into four peaks in the case of the Zn-doped talc (run T2d; Fig. 4b) in good agreement with Wilkins and Ito, (1967). The splitting appears to be dependent on the degree of substitution of the magnesium in the octahedral layer and related to the electronegativity difference between Zn and Mg even if there is not a direct relation between the substitution and splitting parameters. The sharp band displayed in the non-doped talc (run T1p; Fig. 4.30b) indicates an extremely regular environment around the hydroxyl group.

4.3.5 Fibrous talc

Although talc is common, fibrous (asbestiform) talc is rare and its origin has been explained by the replacement of asbestiform amphiboles during retrograde metamorphism.

The production of fibrous talc in these experiments demonstrates that growth of talc after amphibole is not necessary for the production of a fibrous habit. Indeed, we obtained fibrous talc from TZn1 and T2P runs (see table 4.4), together with quartz. Preliminary SEM/EDS analyses show that fibres length ranging from 30 to 100 μm (Fig. 4.31), while the content in zinc dopant is between 5.33 and 8.13 wt% (6.74 wt% in average. All fibrous talc samples showed low amount of Ca^{2+} (likely deriving from $CaCl_2$ used in big percentage as reactant in the starting materials) and it could be involved in the fibrous growth. In order to characterize in detail fibrous talc and to clarify how and why fibrous morphology is obtained, TEM investigations are in progress.

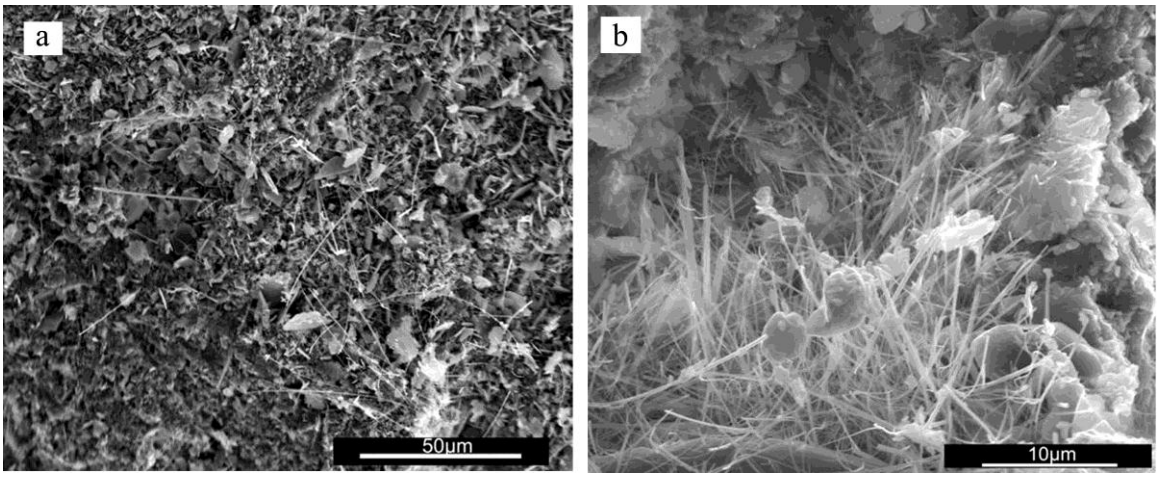

Fig. 4.31. SEM images: a) fibrous talc, TZn1 run; b) fibrous talc, T2P run.

4.4 Mn-doped talc

First attempt have been made to synthesize talc doped with manganese.

In table 4.7 are reported the phases detected for each runs in order of decreasing abundance and the average content of manganese in talc.

Run	Molar ratio		T (°C)	Detected phases	MnO dopant (wt.%)
	MgO	MnO			
T1P	3	0	650	Tlc	---
AC1	2.75	0.25	650	Tlc, Trd Qtz,	3.09
AC2	2	1	650	Trd, K, Tlc, Qtz	8.09
AC3	1.5	1.5	300	Qtz, Tlc, C	11.03
AC4	0	3	300	Agh, Qtz, Tpr	---

Table 4.7. Product list of synthesis for each synthesis in order of decreasing abundance, as detected by XRPD and SEM. α-reactant= H_2O 12%. Tlc = talc, Q = quartz, C = cristobalite, Trd = tirodite $(Mg,Mn)_7Si_8O_{22}(OH)_2$, Agh = alleghanite $Mn_5(SiO_4)_2(OH)_2$, Tpr = Tephroite Mn_2SiO_4

Talc doped with manganese was produced in all runs; only when magnesium was totally substituted by manganese (AC4 run) in the starting mixture no talc formed.

Under optical microscope, the products appear as a soft, compact, grey powder except for sample AC4 for which the use of an agate mortar was necessary to grind the sample.

4.4.1 XRPD characterization

XRPD results show that Mn-doped talc formed both at 300 °C and 650 °C (Fig. 4.32).

Crystallinity is affected by temperature: the characteristic (002) reflection of talc structure appeared clearly in the AC1 diffractogram. This indicated that a hydrothermal synthesis temperature of 650 °C led to a mineral with characteristics closer to those of talc.

Other phases were detected together with Mn-talc in AC2 run; tirodite $(Mg,Mn)_7Si_8O_{22}(OH)_2$ (JCPDS 13-0376) an amphibole phase which can coexist in equilibrium with talc (Chernoshy, 1985); kanoite (29-0865) an anhydrous mineral belonging to the orthopyroxene group, which forms at high temperature when the system losses the water as a consequence of the previous formation of hydrous phases. Sample AC2 is therefore, characterized by an assemblage of hydrous and anhydrous phases (Trd, K, T, in order of decreasing abundance) in good agreement with the experiments reported by Chernoshy, (1985).

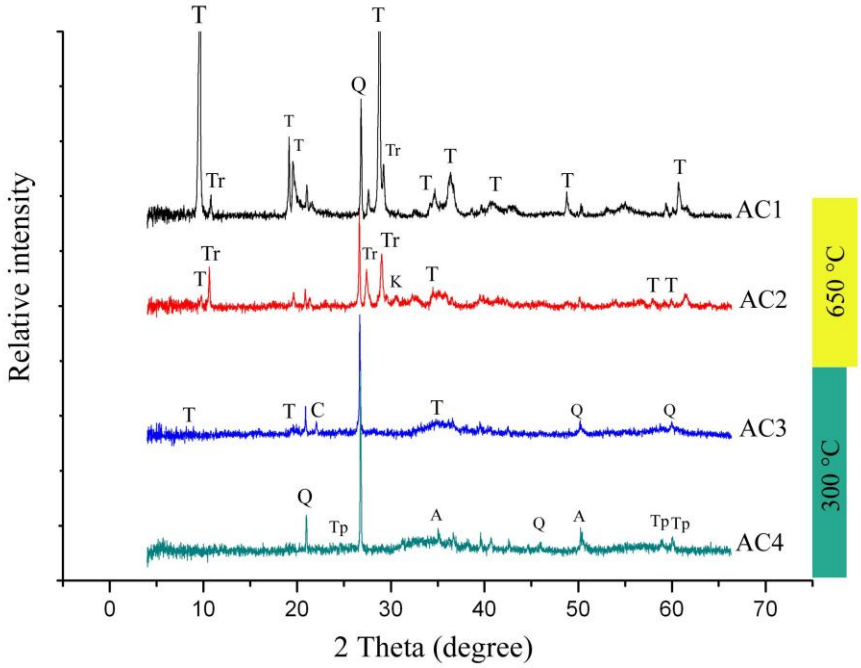

Fig. 4.32. XRPD patterns, identified phases are indicated with capital letters. T = talc (JCPDS 13-0558, 29-1493); Tr = tirodite (JCPDS 13-0376); Q = quartz (JCPDS 46-1045, 33-1161); C = cristobalite (JCPDS 39-1425); Tp = tephroite (JCPDS 35-0748); A = alleghanite (JCPDS 25-1184).

AC3 run presented relatively broad (002) reflection, indicating a low degree of crystallinity of talc due to a decrease of the reaction temperature (from 650 °C to 300 °C). However, on the other hand, lower temperature does not favour the formation of other phases (e. g., tirodite) containing manganese, with the possibility to obtain talc which does not shift from its stoichiometric composition in the ideal products and with a higher content of manganese (about 11 wt %).

Finally, XRPD diffractogram of AC4 run show that alleghanite (JCPDS 25-1184), ($(Mn_5(SiO_4)_2(OH)_2$; Humite group, Norris et al., 1969) and Tpr = Tephroite Mn_2SiO_4 (JCPDS 35-0748) are the stable phases when the starting mixture is supersaturated with manganese.

4.4.2 SEM/EDS characterization

Figure 4.33 show SEM images of products obtained from the four runs (see table 4.6).

Different talc morphologies are observed ranging from well-stacked up flakes (so-called 'macrocrystalline' type) to an heterogeneous stack of small plates ('microcrystalline' type) (Ferrage et al.,2003).

Indeed, talc morphology is temperature dependent: at higher temperature it assumed the classical hexagonal tabular morphology (Fig.s 4.33a and 4.33b) while talc obtained at 300 °C has not a specific morphology (Fig. 4.33c). With regard to lamellar talc, the diameter ranged from a few μm to 5 μm (Fig.s 4.33a and 4.33b) while talc with a cabbage-like morphology is smaller in size (below 2 μm). Figure 4.33d shows skeletal crystals of tephroite Mn_2SiO_4. A skeletal crystal is one that develops under conditions of rapid growth and high degree of supersaturation. Atoms are added more rapidly to the edges and corners of a growing crystal than to the centers of crystal faces, resulting in either branched, tree-like forms or, as in this case (see figure 4.33d) hollow, stepped depressions (hoppers).
EDS/SEM analyses revealed a direct correlation between the content of manganese in the starting mixtures and in the talc obtained. Manganese content ranges from 3.09 wt % (average value calculated on twenty lamellae for each run) in AC1 run to 11.03 wt % in AC3.

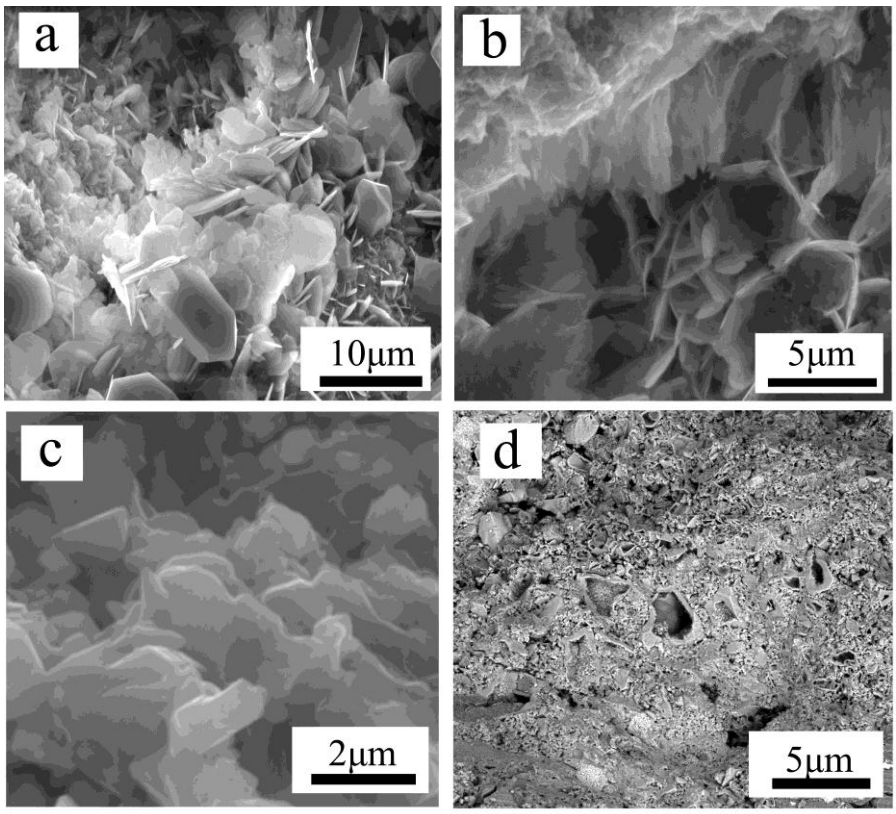

Fig. 4.33. SEM images of various run products: a) lamellar talc, AC1 run; b) talc with plate morphology, AC2 run; c) poor crystallized talc, AC3 run; d) Tephroite Mn_2SiO_4, AC4 run.

4.4.3 DSC/TG characterization

Results of TG and DSC presented in figure 4.34 characterize the thermal behaviour of talc doped with manganese (AC1 run).

From the TG results it followed that a total mass loss is 6.13 % due to contribution of talc and tirodite. A mass loss observed by TG in the range 850-950 °C characterizes the loss of the structural water due to dehydroxylation of the Mn-doped talc. This is confirmed by the DSC endothermal effect that took place at 896.8 °C.

The lower temperature observed for decomposition of Mn-doped talc sample with respect to the non-doped one (see Fig. 4.30 and table 4.6) indicates the lower thermal stability of the doped talc.

It is clear that the presence of manganese in talc lattice which has the ionic radius (0.80 Å) larger than ionic radius of Mg (0.72 Å) causes defects in the Mn-doped talc that decrease its thermal stability.

The dehydroxylation of Mn-doped talc is accompanied by the decomposition of talc into free magnesium oxide and silica (XRPD verified).

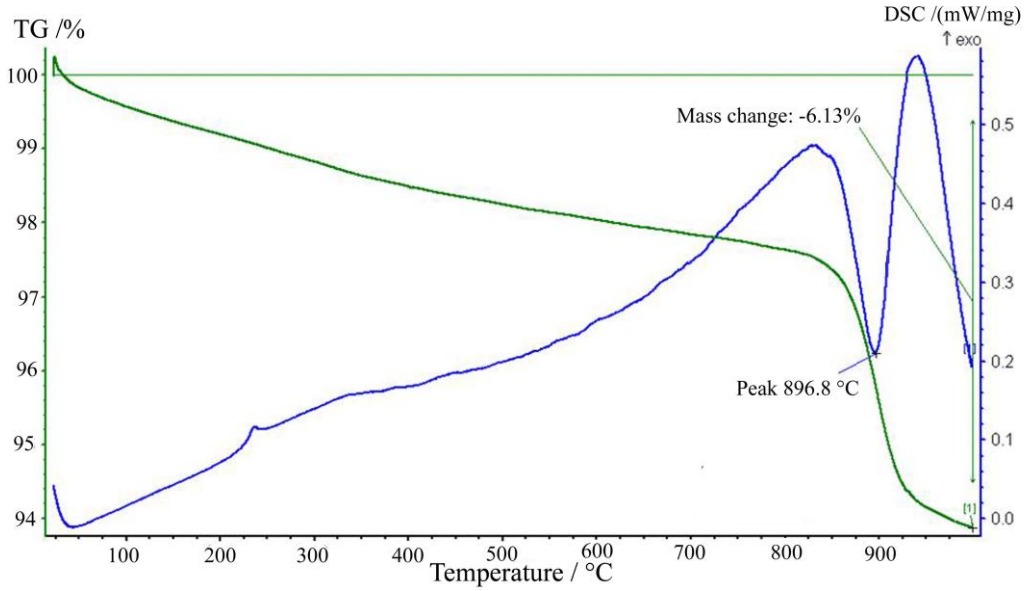

Fig. 4.34. Results of DSC and TG of Mn-doped talc (AC1 Run) in the range 0-1000 °C.

Chapter 5. Conclusion

Growth of single crystals of Zn: $MgSiO_3$ with different Zn concentration was attempted by using the slow-cooling flux method. Two types of flux were used: lithium-molybdate and lithiumvanadomolybdate systems, but only the latter was successful.

The best Zn-doped crystals were obtained at the following experimental conditions: 1) ZnO content in the starting mixture up to 0.60 in molar proportion, 2) very slow cooling rate (1.7 °C/h) and 3) starting temperature of 1050 °C. Crystals grown at these conditions were maximum 3.5 mm in lenght, colorless and all appear to be idiomorphic, commonly without defects, elongated along the c-axis and virtually free of fluid inclusions.

These experiments have clearly demonstrated the following points:

1) It is rather difficult to avoid the formation of enstatite of clino-type even if the enstatite was grown in the stability field of orthoenstatite (above 600 °C) and the cooling rate was slower than a few degrees per hour. Although thorough investigation of the structures of the polymorphs of MgSiO3 is currently underway, their relative stability is not well understood, yet (Huang et al., 1994; Beall, 1993).
   There are many factors which can affect the proto to clino and the ortho to clino transformations (Huang et al., 1994; Beall, 1993; Goel et al., 2007). Even a simple crushing of the samples can induce such a phenomenon.
   However, in this work, orthoenstatite was the predominant crystalline phase;

2) was not possible to avoid the formation of other phases together with enstatite, even if it was grown in the range of temperature in which it is stable and from a starting mixture afforded with the stoichiometry of enstatite;

3) Flux growth method allows crystals up to several mm^3 without big incorporation of the flux-component into the synthesized crystals. This is an important result because the content of element from the solvent, even if in low amount (EDS/SEM detectable), can create additional defect in the lattice which can decrease the quality of the crystals. Only in some rare specimens, veins occurred, which were open towards both ends and contained some quench material;

4) The amount of zinc in Zn-doped enstatite is related to the temperature of melting stage because at this stage Zn element enters the growing enstatite according to its melt/crystal partition coefficient. The maximum content of zinc in enstatite was of about 10 wt%. However, Zn-doped enstatite only grew when Mg^{2+} was only partially substituted by Zn^{2+} in the starting mixture. Pure $ZnSiO_3$ is not stable phase at these synthesis conditions. Therefore it disproportionates to Li_2ZnSiO_4-Zn_2SiO_4 and quartz.

Among the overall goals of this work, one was to characterize the grown enstatite in order to understand how the presence of foreign ions within the structure may change the physical, chemical and optical characteristics of it.

XRD investigations on single crystals show a decrease in cell volume when the content of zinc in enstatite was about 10 wt%. The larger ionic radius of Zn (i. r. 0.74 Å) substituted for Mg^{2+} (i. r. 0.72 Å) on M1 and M2 sites, induces a slight distortion and contraction of the whole crystal lattice which could imply the instability of this crystal phase although the orthorhombic structure keeps almost unchanged.

Single crystals of Zn-doped enstatite were analyzed by μ-Raman spectroscopy. They belong to the orthorhombic crystal system having both the symmetric Si-O-Si bending doublet at 665–687 cm^{-1} and the strongest mode at 83 cm^{-1} (Reynard et al. 2008).

Moreover, the presence of relatively high amount on zinc replacing magnesium shows a very remarkable peak broadening by the mode at 133 cm^{-1} (whose bandwidth turns out to double) and by the one at 343 cm^{-1} (with more than 50% of increase), for which a strong component of metal ion displacement must be postulated.

Mn-doped enstatite was grown by the same method using only lithiumvanadomolybdate system as a flux. Several starting mixtures and different cooling rates were used for Mn-enstatite synthesis, but the best conditions were as follow: 1) MnO content up to 0.60 in molar proportion in the starting mixture; 2) very slow cooling rate (1.7 °C/h); 3) starting temperature of 1050 °C.

Mn-enstatite crystals reach 8 mm in length, they are reddish in color and all appear to be idiomorphic, commonly without defects and elongated along the c-axis.

As for Zn-doped enstatite synthesis, also these experiments have clearly demonstrated that:

1) Orthoenstatite grows in association with clinoentatite, which is present also quenching the products at temperature higher than 600 °C;

2) No phases other than enstatite were detected among the crystallized portion of the starting mixture. The quench material contained significant amount of amorphous material and few crystals of quartz.

3) The incorporation of flux-component in the lattice is avoided: thus, the major problem to remove the possible impurities from the solvent is overcome.

4) The composition of products does not exactly correspond to the composition of the starting materials. However, a direct correlation can be observed between MnO concentration in the starting mixture and Mn-dopant in the grown enstatite, even if the increase was not proportional to the amount of MnO present in the starting mixture.

5) The average amount of MnO wt% in enstatite, ranged between 6.28 wt% and 9.89 wt%. Therefore the representative chemical formulae were: $(Mg_{0.9}Mn_{0.1})SiO_3$ – $(Mg_{0.8}Mn_{0.2})SiO_3$. When magnesium was totally replaced by manganese, no Mn-doped enstatite was obtained. The pressure-temperature of equilibrium conditions of end-member $MnSiO_3$ differ from those used for the synthesis of enstatite (W. V. Maresch and A. Mottana, 1976).

As in Zn-doped enstatite, also in this case some characterizations were performed in order to study how the presence of manganese in the enstatite lattice can influence the properties of this phase.

The cell dimensions of some crystals of enstatite with content in manganese of about 10 wt% were calculated. Results show a volume contraction as a consequence of a slight decrease of *a* and *b* cell axes.

The majority of Raman modes expected for the orthorhombic enstatite phase was satisfactorily displayed.

Raman spectra are strongly affected by the presence of the dopant as confirmed by: 1) a down shifting of the peak positions and a widening of the peaks due to the change in vibrational modes because of the presence of structural defects; 2) a descrease in Raman intensity with increasing of manganese concentration due to the consequent increase in surface reflection.

The cathodoluminescence spectra of enstatite $MgSiO_3$ single crystals intentionally doped with manganese is strongly influenced by the presence of this dopant.

At room temperature, the CL spectrum of $MgSiO_3$: 10 wt % MnO shows a strong broad red emission at 677 nm (Lin Lin et al., 2008), attributed to the transition $^4T_{1g}(G) \rightarrow {}^6A_{1g}$ (S) of Mn^{2+} substitutional to Mg^{2+} position in enstatite. By comparing CL of a pure enstatite with the doped one, it is clearly shown that Mn^{2+} emission was dominant in this material.

Synthesis of talc mineral doped with zinc and manganese were conducted using hydrothermal method under constant pressure of 2 kbar and reaction time of 160 hours with various starting materials. Although it is well known that talc are stable over a wide range of pressure and temperature, the results of the present study show that talc can be synthesized as single phase only under specific experimental conditions and with appropriate source material. In particular, pure talc was synthesised as a unique phase at 650 °C in agreement with Chernosky et al., (1895) and Bose et al., (1994).

With regard to Zn-doped talc, temperature of 650 °C also represents the best one to obtain the highest abundance of Zn-doped talc and biggest lamellae.

The results indicate that the chemical composition and morphology of Zn-doped talc can be controlled effectively by adjusting the reaction conditions. Indeed, it is demonstrated a strong relation between both talc morphology, content of dopant and crystallization temperature. When the temperature of hydrothermal processing is at or below 500 °C, talc produced has a cabbage-like morphology (few microns), while if the temperature is raised to 650 °C, talc assumed its classical hexagonal tabular morphology (from a few μm to 30-40 μm). The content of zinc in talc was higher when the temperature decreased from 650 °C to 300 °C. To assess the different hydrothermal condition under which talc forms of macrocrystalline type or of microcrystalline one, is an important achievement. Nevertheless, the morphology of the talc particles is the main physical parameter that

determines whether specific talc is suitable for a specific application or not E. Ferrage et al., 2003). Indeed, as an example, the effect of talc addition on polymers depends heavily on the particle shape and on the crystallinity of the sample; macrocrystalline talc usually leading to better mechanical properties than microcrystalline talc.

Further studies reveal that:

1) A decrease in temperature from 650 to 300 °C and a treatment of the starting mixture with $CaCl_2$ + distilled water worsened the reactions and talc grew poorly crystallized;

2) It is possible to increase the yield of talc by treating the starting mixture with: a) HCl+ H_2O; b) water in excess; c) higher temperature;

3) Zn-doped talc grew only when Mg was not totally substituted by Zn in the starting mixture.

TG and DSC analysis are reported to characterize the thermal behaviour of talc with increasing of zinc in its lattice. From results it is followed that dopant caused a decrease of the temperature of the release of structure bound OH groups with a consequent formation of free magnesium oxide and silica.

The exothermal effect at 820 °C is relative to the formation of enstatite. Indeed, the decomposition of talc is accompanied by the simultaneous formation of enstatite and silica in some samples.

The IR spectra of Zn-doped talc were very similar to those already reported in the literature for talc in which Mg is partly replaced by another divalent ion.

Variations in peak frequency, like those in bandwidth, are related both to ionic radius and the extent of substitution of the zinc replacing magnesium in the octahedral layer. Zn substitution for Mg in talc mainly affected the hydroxyl stretching fundamental peak in the region from 3620 to 3720 cm^{-1}, splitting itself into as many as four peaks with respect to non-doped talc which displayed only a sharp band.

The hydroxyl stretching vibrations of the Zn-doped talc furnished further valuable information on the grouping of cations around the hydroxyl group.

First attempt have been made to synthesize talc doped with manganese. Preliminary analyses show that large amount of big lamellar Mn-doped talc can be obtained at the

temperature of 650 °C under hydrothermal conditions. Maximum content of Mn-dopant in talc is 12.40 wt%. Talc crystallinity shows strong dependence on crystallization temperature: it increases with increasing of temperature. The composition of products does not exactly correspond to the composition of the starting materials. However, further syntheses are necessary to understand the relation between MnO concentration in the starting oxide mixture and Mn-dopant in the grown talc. TG and DSC results demonstrate that the presence of varying amounts of metal elements replacing Mg in talc cause a decrease in the temperature at which decomposition starts to occur.

This work has laid a foundation for the creation of new potentially technological materials and it opens up several avenues for future work on these materials to have a better knowledge of other physical properties for use in some specific application.

A consistent theme throughout the thesis work was to discuss on the possibility to control the nucleation and crystallization of specific materials using different experimental conditions in order to obtain materials that could be used in different technological fields (e. g., enstatite glass-ceramics; Holand & George, 2012). However, further studies are necessary to clarify the unsolved questions that this work has raised. Finally, as well as talc and enstatite, also the side-products obtained from the synthesis are worth considering, being in some case materials of high technology too.

References

Adnan, S.B.R.S., Mohamed N.S. (2012) Conductivity and Dielectric Studies of Li_2ZnSiO_4 Ceramic Electrolyte Synthesized via Citrate Sol Gel Method. *Int. J. Electrochem*. Sci., **7**, 9844 – 9858.

Aglietti, A. F. (1994) The effect of dry grinding on the structure of talc. *Appl. Clay Sci*. **9**, 139-147.

Ahmeda, M. M., Ibrahim, G. A., Hassan, M. M.A. (2007). Improvement of Egyptian talc quality for industrial uses by flotation process and leaching. Int. *J. Miner. Process*. **83**, 132-145.

Atlas, L. M. (1952) The polymorphism of $MgSiO_3$ and solid state equilibria in the system $MgSiO_3$-$CaMgSi_2O_6$. *J. Geol.* Chicago, **60**, 125-147

Avgustinik, A. J., Vigdergauz, V. S. (1948) Properties of talc during heating. *Ogneupory*, **13**, 218-227.

Avgustinik, A. J., Tandura, P. Z., Sverchkova, L. I. (1949) *Zh. Pnikl. Khim.* (Leningrad), **22**, 1150-1159.

Bailey, S. W. (1991) in Hydrous phyllosilicate, Review in Mineralogy, Mineralogical society of America. **19,**169-188.

Balek, V., Subrt, J., Perez-Maqueda, L.A., Benes, M., Bountseva, I.M., Beckman, I.N., Perez-Rodriguez, J.L. (2008) Thermal behavior of ground talc mineral. *J. Min. Metall.* **44B**, 7-17.

Barrer, R. M. (1948) Syntheses and Reactions of Mordenite. *J. Chem. Soc*., 2158-2163.

Beall GH (1993) Glass - ceramics: Recent development and application . In: Nucleation and Crystallization in Glasses and Liquids. Ceram. Trans. 30 , Weinberg MC (ed.), The Am. Ceram. Soc. Westerville, OH , 241 – 266 .

Bloise, A., Barrese, E., Apollaro, C., Miriello, D. (2009) Flux growth and characterization of Ti- and Ni-doped forsterite single crystals *Cryst. Res. Technol.* **44,** 463-468.

Bloise, A., Barrese, E., Ferraris, G. (2008) Flux growth of straw-like rutile monocrystals. *Cryst. Res. Technol.*, **43**, 121-126.

Bloise, A., Belluso, E., Fornero, E., Rinaudo, C., Barrese, E., Capella, S. (2010) Influence of synthesis conditions on growth of Ni-doped chrysotile. *Micro. Mes. Mat.* **132**, 239-245.

Bloise, A., Pingitore, V., Miriello, D., Apollaro, C., Armentano, D., Barrese, E., Oliva, A. (2011) Flux growth and characterization of Ti-and Ni-doped enstatite single crystals. J. Cryst. Growth 329, 86-91.

Bose, K., Canguly, J. (1994) Thermo gravimetric study of the dehydration kinetics of talc. *Am. Mineral*. **79**, 692-699.

Bowen, N. L., Tuttle, O. F. (1949) The system MgO-SiO2-H2O.*Geol. Soc. Amer. Bull*. **80**, 1947-1960.

Brady, J. E., Humiston, G. E., Heikkinen, H. (1983). General Chemistry: Principles and Structure (3rd ed.). John Wiley & Sons. 671.

Brown, W. L., Morimoto, N., Smith, J. V. (1961) A structural explanation of the polymorphism and trasition of MgSiO3. *J. Geol.* 609, -616.

Cabella, R., Gaggero, L., Lucchetti, G. (1991) Isothermal-isobaric mineral equilibria in braunite-, rhodonite-, johannsenite-, calcite-bearing assemblages from Northern Apennine metacherts (Italy). *Lithos* **27**, 149–154.

Cavalli, E., Bettinelli, M. (1993) Optical spectroscopy of Cr^{3+} ions in orthoenstatite $MgSiO_3$. *Opt. Mater.* **2**, 151-156.

Chabrol, K., Gressier, M., N., Pebere, Menu M. J., Martin, F., Bonino, J. P., Marichal, C., Brendle, J. (2010) Functionalization of synthetic talc-like phyllosilicates by alkoxyorganosilane grafting. *J. Mat. Chem.* **20**, 9695-9706.

Chernosky JR., J. V., Day, H. W., Caruso, L. J. (1985) Equilibria in the system MgO-SiO_2-H_2O: experimental determination of the stability of Mg-anthophyllite *Am. Mineral*. **70**, 223-236.

Choudhury, N., Ghose, S., Chowdhury, C. P., Loong, C. K., Chaplot, S.L. (1998) Lattice dynamics, raman-spectroscopy, and inelastic neutron-scattering of orthoenstatite $Mg_2Si_2O_6$, *Phys. Rev, B,* Condensed matter., **58**, 756-765.

Christianson, D. W. (1997) Structural chemistry and biology of manganese metal-loenzymes. *Prog. Biophys. Mol. Biol.*, **67**, 217-252.

Cotton, F. A., Wilkinson, G. (1980) .Advanced Inorganic Chemistry. A Comprehensive Text, 4th ed., John Wiley and Sons: New York.

Deer, W. A., Howie, R. A, Zussman, J. Rock-Forming Minerals. 2th Edition, 3B, The Geological Society 2009.

Dellisanti, F., Valdrè, G., Mondonico, M. (2009) Changes of the main physical and techonological properties of talc due to mechanical strain. *Appl. Clay Sci*. **42**, 398-404.

Denac, M. Musil, V., Šmit, I. (2004). Structure and mechanical properties of talc-filled blends of polypropylene and styrenic block copolymers. *J. Polym. Sci*., Part B: Polym. Phys. **42**, 1255-1264.

Edgar, A. D. Experimental petrology, basic principles and techniques. Oxford University Press (1973).

Evans, B. W., Guggenheim, S. (1988) Talc, Pyrophyllite, and related minerals. In S. W. Bailey (ed.) hydrous silicates (Exclusive of Micas). Rev. Min. 19, 225-280

Farmer V.C. (1958) The infrared spectra of talc, saponite and hectorite. *Mineral. Mag.* **31**, 829-845.

Ferrage E., Martin F., Boudet A., Petit S., Fourty G., Jouffret F., Micoud P., de Parseval P., Salvi S., Bourgerette C., Ferret J., Saint-Gérard Y., Buratto S. & Fortune´ J.P. (2002) Talc as nucleating agent of polypropylene: morphology induced by lamellar particles addition and interface mineral-matrix modelization. *J. Mater. Sci.* **37**, 1561 –1573.

Ferrage, E., Martin F., Petit, S., Pejo-Soucaille, S., Micoud, P., Fourty, G., Ferret, S., Salvi, S., De Parseval, P., Fortune, P. (2003) Evaluation of talc morphology using FTIR and H/D substitution. *Clay Miner.* **38**, 141–150.

Fyfe, W. S. (1960) Hydrothermal synthesis and determination of equilibrium between minerals in the subliquidus region. *J. Geol.* **68**, 553-566.

Fraùsto da Silva, J. R., Williams, R. J. P. (1991) The Biological Chemistry of the Elements. The Inorganic Chemistry of Life; Clarendon Press: Oxford, England.

Gaft, M., Reisfeld, R., Panczer, G. Modern luminescence spectroscopy of minerals and materials. Springer (Ed.), Berlin, Heidelberg, New York, 2005.

Goel A; Tulyaganov DU; Agathopoulos S; Ribeiro MJ; Ferreira J.M.F. (2007) Synthesis and characterization of $MgSiO_3$-containing glass-ceramics, *Cer. Int.* **33,** 1481-1487.

Grandin de L'éprevier, A., Ito, J. (1983) Flux grown orthoenstatite by a multiple slow-cooling technique. *J. Cryst. Growth* **64**, 411-412.

Grandin de L'Eprevier, A (1972) Synthèse de monocristaux de forstérite Mg_2SiO_4 par la methode des sels fondus. Thèse, La Faculté des Sciences d'Orlèans. Orleans. France.

Grover, J E. (1972) The solubility of low-clinoenstatite in the system $Mg_2Si_2O_6$-$CaMgSi_2O_6$ (abstr.) *Trans. Am.* Geophys. Union, 539-549.

Gruner, J. W. (1934) Crystal Structures of Talc and Pyrophyllite. *Z. Krist*. **88**, 412-419.

Hambidge, K. M., Krebs, N. F. (2007). Zinc deficiency: a special challenge. *J. Nutr.* **137,** 1101.

Heiserman, David L. (1992) Element 30: Zinc. Exploring Chemical Elements and their Compounds. New York: TAB Books.

Hendricks, S. B. (1938) On the crystal structure of talc and pyrophyllite. *Z. Krist*. **99**, 264 274.

Hernandez, B. A, Gonzalez, R.,Viesca, J., Fernandez, J., Diaz, F. J., MacHado, A., Chou, R., Riba, J. (2008) CuO, ZrO_2 and ZnO nanoparticles as antiwear additive in oil lubricants. *Wear* **265**, 422-428.

Höland, W., Beall, G.N. (2002) Glass-Ceramic Technology. The American Ceramic Society, Westerville, Ohio.

Holand W., Beall, G. H (2012) Glass-ceramic technology 2nd ed. Wiley-The American ceramic society, USA.

Huang, E. Chen, C.H., Huang, T., E.H., Xu, J.A. (2000) Raman spectroscopic characteristics of Mg-Fe-Ca pyroxenes. *Am. Mineral.* **85**, 473-479.

Huang, C.M., Kuo, D.H. Kim,Y.J., Kriven, W. (1994) Phase stability of chemically derived enstatite (MgSiO3) powders, *J. Am. Ceram. Soc.* **77**, 2625– 2631.

Ishida, K. (1990) Identification of infrared OH librational bands of talc- willemseite solid solution and Al (IV)-free amphiboles through deuteration. *Min. J.* **15**, 93-104.

Ito, J (1975) High temperature solvent growth of orthoenstatite, $MgSiO_3$, in air. *Geophys Res. Letters* **2**, 533-536.

J. Giese, R. F. (1974) Interlayer bonding in talc and pyrophyllite. *Clay Clay Miner.* **23,** 165-166.

J. Giese, R. F. (1978) The electrostatic interlayer forces of layer structure minerals. *Clay. Clay Miner.* 26, 51-57.

Johnson, R. L, Virta, R. L. (2000). Am. Ceram. Soc. Bull. 79, 79-81

Karrad, S., Lopez Cuesta, J.-M, Crespy A. J. (1998) Influence of a fine talc on the properties of composites with high density polyethylene and polyethylene/polystyrene blends. *Mater. Sci*. **33**, 453-461.

Kaupp M., Dolg M., Stoll H., Von Schnering, H. G. (1994). Oxidation state +IV in group 12 chemistry. Ab initio study of zinc(IV), cadmium(IV), and mercury(IV) fluorides. *Inorg. Chem*. **33**, 10, 2122-2131.

Keppler, H. (1992) Crystal field spectra and geochemistry of transition metal ions in silicate melts and glasses. *Am. Mineral.* **77,** 62 - 75.

Kirak, A., Yilmaz, H., Guler, S., Guler, C. (1999) Dielectric properties and electric conductivity of talc and doped talc. *J. Phys. D:* Appl. Phys. **32,** 1919-1927.

Koshimizu, H., Higuchi, S., Otsuka, R. (1981) Hydrothermal synthetis and some properties of the talc-willemseite solid solutions. (Abstract), J. Clay Sci. Soc. Japan. 21, 61-71

Lehto, R. S. (1968) Zinc. In Clifford A. Hampel. The Encyclopedia of the Chemical Elements. New York: Reinhold Book Corporation. 822–830.

Lin, L., Min, Y., Chaoshu, S., Weiping, Z., Baogui Y. (2006) Synthesis and Luminescence Properties of Red Phosphors: Mn^{2+} Doped $MgSiO_3$ and Mg_2SiO_4 Prepared by Sol-Gel Method. *J. Rare Earths* **24**, 104-107.

Lin, L., Chaoshu, S., Wang, Z., Zhang, W., Yin, M. (2008) A kinetics model of red long-lasting phosphorescence in $MgSiO_3$: Eu^{3+} , Dy^{3+} , Mn^{2+}. *J. Alloys Compd.* **466,** 546-550.

Maresch, W. V., Mottana, A. (1976) The Pyroxmangite-Rhodonite Transformation for the $MnSiO_3$ Composition. Contributions to Mineralogy and Petrology, **55,** 69-79.

Martin, F., Petit, S., O. Grauby, Lavie, M. P. (1999) Infrared band identification in Ge talcs. *Clay Min.* **34**, 365-374.

Marzbani, P., Resalati, H., Ghasemian, A., Shakeri, A. (2013) Talc, a multi-purpose filler: a review of talc's features and improvement methods of its efficiency. Annals of Biological research **4**, 159-162.

McKinnie, I. T., Choie, R. Y. (1997) Efficient laser operation of heavily-doped Cr^{4+} forsterite. *Opt. Quant Electron.* **29**, 605-610.

McMillan, P.F., Hofmeister, A.M. (1988): Infrared and Raman spectroscopy. in Spectroscopic methods in mineralogy and geology, Hawthorne, F.C., ed., *Rev. Mineral.*, **18,** 99–159.

Menczel, J., Varga, J. (1983) Influence of nucleating agents on crystallization of polypropylene. I. Talc as nucleating agent. *J. Therm. Anal.* **28**, 161 –174.

Moezzi, A., McDonagh, A. M., Cortie, M. B. (2012) Review: Zinc oxide particles: Synthesis, properties and applications. *Chem. Eng. J.* 185–186, 1–22.

Moncorgè, R., Bettinelli, M., Guyot, Y., Cavalli, E., Capobianco, J. A., Girard, S. (1999) Luminescence of Ni^{2+} and Cr^{3+} centres in $MgSiO_3$ enstatite crystals. *J. Phys. Condens. Matter* **11,** 6831-6841.

Mottana, A. Fondamenti di mineralogia geologica, Zanichelli ed. Italia, (1988).

Nacken, R. (1946) Artificial Quartz Crystals, etc. U.S. Office of Technical Services Report, PB-18–748 and 28–897.

Norris, W., Jones, P., Ribbe H., Gibbs, G. V. (1969) Crystal chemistry of the humite minerals. *Am. Mineral.* **54,** 309-313.

Ozima, M. (1982) Growth of orthoenstatite crystals by the flux method. J. *Jpn. Assoc. Mineral. Petrol. Econ. Geol.* **3** (Suppl.), 97-103.

Ozima, M., Akimoto, S. (1983) Flux growth of single crystals of $MgGeO_3$ polymorphs (orthopyroxene, clinopyroxene, and ilmenite) and their phase relations and crystal structures. *Am Mineral* **68**, 1199–1205.

Perdikatsis, B. & Burzlaff, H. (1981): Strukturverfeinerung am Talk $Mg_3Si_4O_{10}(OH)_2$. *Z. Krist* **156**, 177-186.

Pidluzhna, A. Y., Grigorchak, I. I., Nikipanchuk, M. V., Ostafiychuk, B. K., Budzulyak, I. M., Mitsov, M. M., Yablon, L. S. (2012) Intercalation current in oxygen- and sulfur-doped talc. *Russ. J. Electrochem*. **48**, 545- 602.

Rayner, J. H., Brown, G. (1973) The structure of talc. *Clay. Clay Miner.* **21**, 103-114.

Reynard, B. Bass, J. D., Jackson, J. M. (2008) Rapid identification of steatite–enstatite polymorphs at various temperatures. *J. Eur. Ceram. Soc.* **8**, 2459-2462.

Russell, J. D., Farmer, V. C., Velde, B. (1970). Replacement of OH by OD in layer silicates, and identification of the vibrations of these groups in infra-red spectra. *Mineral. Mag*. **37**, 869-879.

Schwandt, S. C., Mckay, G. A. (2006) Minor- and trace-element sector zoning in synthetic enstatite. *Am Mineral.* **91**, 1607-1615

Smyth, J. (1974) Experimental study on the Polymorphism of Enstatite. *Am. Mineral*. *59*, 345-352.

Smyth, J. R., Ito, J. (1977) The synthesis and crystal structure of magnesium-lithium-scandium-protopyroxene. *Am. Mineral.* **62**, 1252-1257.

Smyth, J. R. (1973) Experimental study on the polymorphism of enstatite. *Am. Minera.*, **59**, 345-352.

Stalder, R. (2002) Synthesis of enstatite single crystals at high pressure. *Eur. J. Mineral.* **14,** 637-640

Stalder, R., Kronz, A., Schmidt, B.C. (2009) Raman spectroscopy of synthetic (Mg,Fe)SiO_3 single crystals. An analytical tool for natural orthopyroxenes. *Eur. J. Mineral.,* **21** 27-32.

Takahashi, N, Tanaka, M., Satoh, T., Endo, T. (1994) Study of Synthetic Clay Minerals. III. Synthesis and Characterization of Two Dimensional Talc. *Bull. Chem. Soc. Jpn.* **67**, 2463-2467.

Takesue M., Hayashi H., Smith JR R. L. (2009) Thermal and chemical methods for producing zinc silicate (willemite): a review. Progress in Crystal Growth and Characterization of Materials **55**, 98-124.

Tanabe, Y., Sugano, S. (1954) On the absorptionspectra of complex ions. I and II. *J. Phys. Soc.* Jpn. **9,** 753-766.

Tanabe, Y., Sugano, S. (1954) On the absorptionspectra of complex ions. I and II. J. *Phys. Soc. Jpn.* **9**, 766-779.

Tanaka, T. and Takey, H. (1997) Growth of $MgSiO_3$ orthoenstatite single crystals by the top-seeded solution growth (TSSG) method. *J. Cryst. Growth* **180,** 206-211.

Turner, F. J., Heard, H., Griggs, D. T. (1960) Experimental deformation of enstatite and accompanying inversion to clinoenstatite. XXI *Int. Geol Cong Copenhagen*, **18**, 399-408.

Ushio, M., Kobayashi, N., Suzuki, M., Sumiyoshi, Y. (1991) Crystal growth of Mg_2SiO_4 and $MgSiO_3$ single crystals by the flux method. *J. Am. Ceram. Soc*. **74,** 1654-1657.

Walker, G. In Chemical Bonding and Spectroscopy in Mineral Chemistry. F. J. Berry and D. J. Vaughan (Ed.), Springer (1985) 103.

Walker, G., Abumere, O. E., Kamaluddin, B. (1989) Luminescence spectroscopy of Mn^{2+} rock-forming carbonates. *Mineral. Mag*. **53**, 201-211

Ward, W., Phillips, J. M. (1971) Calculated lamellar binding I. van Der Waals bonding in talc and pyrophyllite Surface. *Amer. J. Sci.*. **25,** 379-384.

Wesolowski, M (1984). Thermal decomposition of talc: A review. *Thermochim. Acta* **78**, 395-421.

West, A. R. (1980) The crystal structures and the phase transformation of Zn-Li silicates: discussion, *Am. Mineral.* **65**, 1059-1060.

White, W.B. (1975) Structural interpretation of lunar and terrestrial minerals by Raman spectroscopy. in ‘‘Infrared and Raman spectroscopy of lunar and terrestrial minerals’’, C. Karr Jr., ed., Academic Press, New York, 325–358.

Wilkins, R. W. T., Ito, (1967) Infrared spectra of some synthetic talcs. *J. Am. Mineral.* **52**, 1649-1661.

Yoder, H. S. (1952) The MgO-Al_2O_3-SiO_2-H_2O system and the related metamorphic facies. *Amer. J. Sci.* 250A, 569-627.

Zazenski, R., Ashton, W. H., Briggs, D., Chudkowski, M., Kelse, J. W., Maceachern, L., Mccarthy, E. F., Nordhauser, M. A., Roddy, M. T., Teetsel, N. M., Wells, A. B., Gettings S. D. (1995). *Regul. Toxicol. Pharm*. **21**, 218-229.